DOCTOR OF PHILOSOPHY

Drivers of thermocline shear in seasonally stratified shelf seas

Li, Jingnan

Award date:
2017

Awarding institution:
Bangor University

Drivers of thermocline shear in seasonally stratified shelf seas

Li Jingnan

School of Ocean Sciences

Bangor University

September 2017

To Zhou Yanru, Li Zhenguo

To Wu Junrong

To Malin, Zuaner

Declaration and Consent

Details of the Work

I hereby agree to deposit the following item in the digital repository maintained by Bangor University and/or in any other repository authorized for use by Bangor University.

Author Name: ……………………………………………………………………Li Jingnan

Title: ………………………… Drivers of thermocline shear in seasonally stratified shelf seas

Supervisor/Department: .... Prof. T P Rippeth, School of Ocean Sciences

Funding body (if any): ....Chinese Scholarship Council

Qualification/Degree obtained: ……………………………………………………………………………….PhD

This item is a product of my own research endeavours and is covered by the agreement below in which the item is referred to as "the Work". It is identical in content to that deposited in the Library, subject to point 4 below.

Non-exclusive Rights

Rights granted to the digital repository through this agreement are entirely non-exclusive. I am free to publish the Work in its present version or future versions elsewhere.

I agree that Bangor University may electronically store, copy or translate the Work to any approved medium or format for the purpose of future preservation and accessibility. Bangor University is not under any obligation to reproduce or display the Work in the same formats or resolutions in which it was originally deposited.

Bangor University Digital Repository

I understand that work deposited in the digital repository will be accessible to a wide variety of people and institutions, including automated agents and search engines via the World Wide Web.

I understand that once the Work is deposited, the item and its metadata may be incorporated into public access catalogues or services, national databases of electronic theses and dissertations such as the British Library's EThOS or any service provided by the National Library of Wales.

I understand that the Work may be made available via the National Library of Wales Online Electronic Theses Service under the declared terms and conditions of use (http://www.llgc.org.uk/index.php?id=4676). I agree that as part of this service the National Library of Wales may electronically store, copy or convert the Work to any approved medium or format for the purpose of future preservation and accessibility. The National Library of Wales is not under any obligation to reproduce or display the Work in the same formats or resolutions in which it was originally deposited.

Statement 1:

This work has not previously been accepted in substance for any degree and is not being concurrently submitted in candidature for any degree unless as agreed by the University for approved dual awards.

Signed ………………………………………….. (candidate)

Date ……………5^{th} December 2017…………………..

Statement 2:

This thesis is the result of my own investigations, except where otherwise stated. Where correction services have been used, the extent and nature of the correction is clearly marked in a footnote(s).

All other sources are acknowledged by footnotes and/or a bibliography.

Signed …………………………………………. (candidate)

Date ……………5^{th} December 2017…………………..

Statement 3:

I hereby give consent for my thesis, if accepted, to be available for photocopying, for inter-library loan and for electronic repositories, and for the title and summary to be made available to outside organisations.

Signed …………………………………………. (candidate)

Date ……………5^{th} December 2017…………………..

<u>Statement 4</u>:

Choose **<u>one</u>** of the following options

a)	I agree to deposit an electronic copy of my thesis (the Work) in the Bangor University (BU) Institutional Digital Repository, the British Library ETHOS system, and/or in any other repository authorized for use by Bangor University and where necessary have gained the required permissions for the use of third party material.	
b)	I agree to deposit an electronic copy of my thesis (the Work) in the Bangor University (BU) Institutional Digital Repository, the British Library ETHOS system, and/or in any other repository authorized for use by Bangor University when the approved **bar on access** has been lifted.	
c)	I agree to submit my thesis (the Work) electronically via Bangor University's e-submission system, however I **opt-out** of the electronic deposit to the Bangor University (BU) Institutional Digital Repository, the British Library ETHOS system, and/or in any other repository authorized for use by Bangor University, due to lack of permissions for use of third party material.	

Options B should only be used if a bar on access has been approved by the University.

In addition to the above I also agree to the following:

1. That I am the author or have the authority of the author(s) to make this agreement and do hereby give Bangor University the right to make available the Work in the way described above.

2. That the electronic copy of the Work deposited in the digital repository and covered by this agreement, is identical in content to the paper copy of the Work deposited in the Bangor University Library, subject to point 4 below.

3. That I have exercised reasonable care to ensure that the Work is original and, to the best of my knowledge, does not breach any laws - including those relating to defamation, libel and copyright.

4. That I have, in instances where the intellectual property of other authors or copyright holders is included in the Work, and where appropriate, gained explicit permission for the inclusion of that material in the Work, and in the electronic form of the Work as accessed through the open access digital repository, *or* that I have identified and removed that material for which adequate and appropriate permission has not been obtained and which will be inaccessible via the digital repository.

5. That Bangor University does not hold any obligation to take legal action on behalf of the Depositor, or other rights holders, in the event of a breach of intellectual property rights, or any other right, in the material deposited.

6. That I will indemnify and keep indemnified Bangor University and the National Library of Wales from and against any loss, liability, claim or damage, including without limitation any related legal fees and court costs (on a full indemnity bases), related to any breach by myself of any term of this agreement.

Signature: ………………………………………………………

Date : ……………<u>5th December 2017</u>…………………..

Acknowledgements

I would like to thank Professor T. P. Rippeth for being a great and helpful supervisor. His sensitive senses of physics inspired me many times during my research. He is not only helping with the research and thesis writing, but also always kind and patient, and giving me a lot encouragement during my great days and bad days.

I would like to thank Dr. B. J. Lincoln, who helped me to get into this area at the beginning. The very first idea about my research was inspired by some of his previous work. And I would like to thank Dr. Y. D. Lenn who helped me with some serious math issue during the study.

I would like to thank Mr. B Scannell, from whom I learnt a lot, some about research and some about life - how to be a better person and how to be brave.

I would like to thank Mrs. J. Madge and Miss I. Rottwinkel, who helped me with my English writing and gramma, thank you for your time, your kind words and snacks.

I would like to thank all my colleagues, Dr. D. Mameha, Dr. J. Griffiths, Dr. E. M. A. Merfyn, Ms. J. M. Silvester, Dr. S. B. Wilmes, Miss M. Baker, Mr. B. Barton and Mr. E. Lockhart, for helping me when I just arrived years ago, and during my Ph.D study. I feel so lucky to meet all of you, and I feel such a great honour to join in this great team.

I would like to thank the support from my family and all my friends, particularly Zhou Yanru, Wu Junrong, Li Wenfei, Zuo Wenyi, Lin moqing and Jia Zhaohan, who are the source of power to help me go through all the tough days.

Doing Ph.D. is a great adventure in my life, I cannot achieve this happy ending without you.

Abstract

Shelf seas occupy only 7% in area and less than 0.5% in volume of the entire ocean, but they play an important role in the carbon cycle by taking about 20% - 50% of all the CO_2 absorbed by the ocean. Diapycnal mixing is a key process in transporting nutrients, carbon, water mass etc. between the surface and the lower mixed layers in a seasonally stratified shelf sea. The identification and quantification of the processes responsible for driving diapycnal mixing in seasonally stratified seas are the subjects worth study.

Early researchers have examined the correlation between enhanced bulk shear and the wind. The bulk shear is defined as the average of the shear in two defined layers which are either side of the thermocline. However the contribution from the barotropic tide has generally been neglected.

This study examines two stages of the evolution of water column stratification: the spring development stage and the autumn break down stage. Rotary spectral analysis shows that the shear across thermocline corresponds to different drivers when the water stratification is different. At the spring development stage, the shear across the thermocline corresponds to near-inertial oscillations, which are related to wind. Whilst at the autumn break down stage, the shear across thermocline relates to both the near-inertial oscillations and the barotropic tide. Thus, in contraction to earlier research, our research suggests that the barotropic tide is another dominant driver in the generation of shear.

However not all observations can be explained by the wind or barotropic tide. The additional consideration of the baroclinic tide helps explain the signal of an odd shear spike observed in the northern North Sea, which occurred during a period of weak shear production by the wind and barotropic tide.

A 1D two-layer vertical dynamic numerical model and a 1D turbulence closure numerical model were applied to investigate the impact of wind and barotropic tide on shear, respectively. In addition, the impacts of hydrographic conditions on the driver of shear were considered. Coherence analysis was applied to examine the similarity of constituents (in frequency domain) between the modelled shear production and the observations. The model sensitivity analysis demonstrates that the switch of driver of shear is highly related to the depth ratio, which is the ratio of thermocline depth over water depth.

Contents

List of figures

7.4 = Bulk shear components of E-W and N-S directions and baroclinic tide in period A.

7.5 = The evolution of shear estimated from observed current velocity, compared with that from baroclinic tide, from two-layer model, the wind speed and barotropic tidal current during the same period.

7.6 = Time serials of wind speed, directions of baroclinic tide and bulk shear, bulk shear squared, evolution of bulk shear squared and the modelled production of bulk shear squared.

List of tables

List of abbreviated terms

WIS = western Irish Sea

NNS = northern North Sea

TC model = 1D Turbulence Closure Numerical Model

Two-layer model = 1D Two-Layer Vertical Dynamic Numerical model

List of symbols

α = direction of shear

β = direction of boundary stresses

β_s, β_b = direction of surface and bottom boundary stresses

$\frac{\partial \eta}{\partial x}$, $\frac{\partial \eta}{\partial y}$ = northern and eastern surface elevation slopes

κ = von Karman's constant

ρ = water density

ρ_{air} = air density

ρ_m = depth averaged water density

$\rho(z)$ = water density at depth z

τ_s, τ_b = sea surface and bed stress

τ^x, τ^y = northern and eastern components of shear stress normalized by density

Φ = stratification parameter

φ = latitude

Ω = rotation rate of the Earth

B_1 = Mellor Yamada constant

C_{D10} = surface drag coefficient

C_{Db} = bed drag coefficient

C_i = interfacial drag coefficient

C_{xy} = coherence of x and y signals

dt = sampling time interval

$D_i(S^2)$ = dissipation by interfacial friction

DR = depth ratio

E_k = turbulent kinetic energy

f = Coriolis coefficient

f_1, f_2 = frequencies of two example signals

f_s = sampling frequency

f_{max} = maximum frequency can be separated in rotary spectral analysis for a certain time series data

g = gravitational acceleration

h = water depth

h_{diff} = height difference between the centers of surface mixed layers

h_s = surface mixed layer thickness

h_b = lower mixed layer thickness

IF = inertial frequency

K_Z = eddy diffusivity

L = length scale

M = Manning Roughness

N^2 = buoyancy frequency

N_Z = eddy viscosity

pCO_2^{air}, pCO_2^{sea} = partial pressures of carbon dioxide in the atmosphere and in the sea surface

ΔpCO_2 = difference of partial pressure of carbon dioxide between atmosphere and sea surface

$P(S^2)$ = production of bulk shear squared

q = intensity of turbulence velocity

R_i = Richardson number

S^2 = shear squared in the water column

S_{bk} = bulk shear

S_M, S_H = stability function

S_u, S_v = northern and eastern components of shear

T = time series length for observed data

U = current speed

U_{10} = wind speed at 10 m height

U_{bt} = magnitude of barotropic current

UC = baroclinic current

UCC = time averaged baroclinic current

UCT = baroclinic tide

U_{diff} = magnitude of current velocity difference above and below thermocline

$\overline{U}_s$, $\overline{U}_b$ = mean velocity of surface and lower mixed layers

UT = barotropic current

u(z,t) = barotropic tide velocity (in fig 1.1)

u, v = current velocity components

u_{10}, v_{10} = northern and eastern components of wind speed at 10 m height

u_b, v_b = northern and eastern components of lower mixed layer current velocity

u_{diff} = northern components of magnitude of current velocity difference above and below thermocline

u_m, v_m = northern and eastern components of depth mean current velocity

u_{bt}, v_{bt} = northern and eastern components of barotropic current

u_{bc}, v_{bc} = northern and eastern components of baroclinic current

u_s, v_s = northern and eastern components of surface mixed layer current velocity

ushear, vshear = northern and eastern components of shear

u_{tc}, v_{tc} = northern and eastern components of tidal current speed

z = distance below the sea surface

z_i = internal depth

Chapter 1

Introduction

1.1 Background and motivation for the study

The warming of the global climate system since the 1950s [IPCC, 2013] has attracted public attention to global climate change. Global climate change is the variation of the climate system among the atmosphere, hydrosphere and cryosphere. Climate change can be observed through sea surface temperature increase, atmospheric temperature increase, sea level rise, glacier diminish, and the increase of greenhouse gases etc. [IPCC, 2013].

Radiative forcing is a key factor that has an impact on climate change [IPCC, 2013]. Radiative forcing is the net energy input to the global system, and which is estimated by the difference between the solar energy absorbed by the global system and the energy that is radiated back into the space [IPCC, 2013]. The impact of the radiative forcing balance on global average temperature is significant because, the positive net energy entering the global system will lead to an increase in global average temperature [IPCC, 2013]. The biggest contribution to changing the radiative forcing balance is from greenhouse gases in the atmosphere, as these prevent solar energy being radiated back into space [IPCC, 2013]. Of all the greenhouse gases the impact of CO_2 on the radiative forcing is the most significant (fig 1.1).

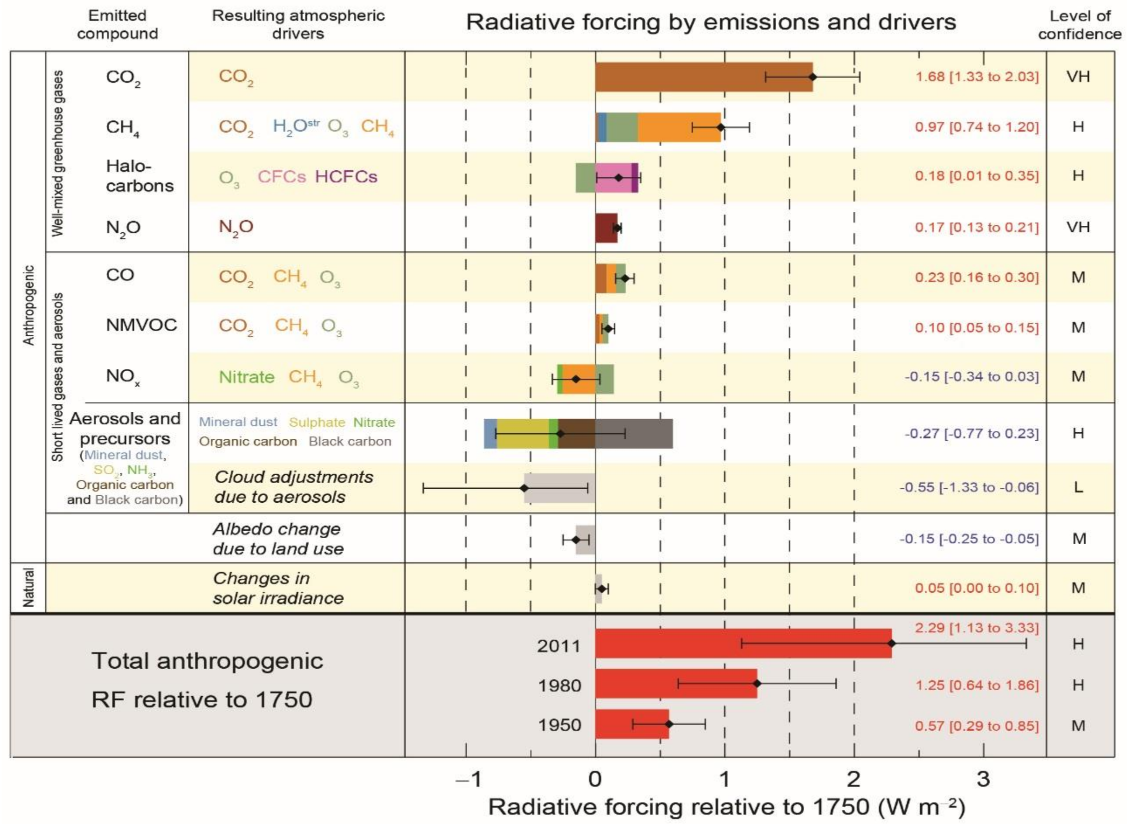

Fig 1.1 The contribution from different emissions and drivers to the radiative forcing in 2011. Among all the emissions the impact of $\mathbf{CO_2}$ on the radiative forcing is the most significant (IPCC, 2013).

The IPCC [2013] claimed that the ocean is estimated to uptake 30% of all the cumulative emitted anthropogenic CO_2. Among all the sea areas, the temperate seasonally stratified shelf seas, which act as the net sink of atmospheric CO_2 [Chen and Borges, 2009; Rippeth et al., 2014], show a great importance in the global carbon cycle.

The shelf sea is defined as the sea area which extends from the coastline to 200 m water depth. It plays a remarkable role in transporting and translating process of carbon among the atmosphere, ocean and continent due to its unique feature of linking these areas [Walsh, 1991; Bauer et al., 2013; Rippeth et al., 2014].

Although the shelf seas only occupy 7% of the area and less than 0.5% of the volume of the entire global ocean, they disproportionately contribute to 20% - 50% of the carbon sink in the ocean [Rippeth et al., 2014]. Additionally, the shelf seas contain a large amount of the inorganic carbon (30% - 50%), the organic carbon burial (around 80%) and the global primary oceanic production (15% - 30%) [Simpson and Sharples, 2012; Bauer et al., 2013; Rippeth et al., 2014].

A significant carbon uptake from the atmosphere, which is known as the continental shelf carbon pump, is sustained by seasonal stratification [Rippeth et al., 2014].

The direction of net carbon dioxide fluxes is determined by the difference of partial pressure of carbon dioxide between atmosphere and sea surface, the ΔpCO_2 [Rippeth et al., 2014]. The partial pressures of carbon dioxide in the atmosphere and in the sea surface are defined as pCO_2^{air} and pCO_2^{sea} respectively, which:

$$\Delta pCO_2 = pCO_2^{air} - pCO_2^{sea} \tag{1.1}$$

A positive ΔpCO_2 implies a net CO_2 flux from atmosphere to the ocean, the regions with a positive ΔpCO_2 are normally regarded as a carbon sink. The negative ΔpCO_2 implies a carbon source, and release CO_2 from sea surface to the atmosphere. Where ΔpCO_2 is 0 represents a perfect balance of CO_2 between the atmosphere and sea surface and thus there will be no exchange of CO_2 between the air-sea interface. The positive ΔpCO_2, the carbon sink, appears in high latitude in the shelf sea [Rippeth et al., 2014]. The negative ΔpCO_2, the carbon source, appears in the warm, low latitude oceans [Rippeth et al., 2014].

The water stratification prevents water exchange between surface mixed layer and lower mixed layer. Thus consume of nutrients or CO_2 in each layer cannot be fulfilled from the other layer through water vertical mixing.

Assuming that the partial pressure of carbon dioxide below and above the sea surface is balanced at the beginning, *i.e.* $pCO_2^{air} = pCO_2^{sea}$ and $\Delta pCO_2 = 0$. When the primary production process starts in the surface mixed layer (in the euphotic zone), the photosynthesis by phytoplankton consumes the CO_2 at surface mixed layer. As described, due to the water stratification, the loss of CO_2 in the surface mixed layer cannot be supplied from the lower mixed layer through the vertical mixing. Thus, the pCO_2^{sea} at the sea surface decreases and ΔpCO_2 becomes positive. The carbon uptake process at the sea surface is triggered through this mechanism [Rippeth et al., 2014].

However, the carbon pump would stop at some point when the nutrients required for photosynthesis run out. Diapycnal mixing is required to sustain the photosynthesis process by supplying the nutrients from the lower mixed layer to the surface mixed layer where there is sufficient light to support photosynthesis [Rippeth et al., 2014].

1.2 Vertical structure in shelf seas

The area of water column stratified in the shelf sea is determined by the position of tidal mixing fronts [Simpson, 1971]. Fig 1.2 shows a section of the water column structure across a shelf sea front. On the near shore side of the tidal mixing front, the water column stays well mixing around the whole year, while at the same time, at the off-shore side of the mixing front, the water column experiences a seasonal stratification. The stratification starts to form in spring, develops during the summer, breaks down in autumn and disappears in winter [Simpson and Sharples, 2012]. Fig 1.3 shows a bird's-eye view of surface water temperature distribution from the near shore towards the off-shore, the sea surface temperature in the shelf sea shows a patchwork of warm water (the stratified area) and cold water (the well mixed area), which is separated by the tidal front [Rippeth, 2005; Simpson and Hunter, 1974]. The well mixed water appears at the shallower water (near shore area) where the tidal current is strong, and hence mixing is strong, and so the impact of tidal stirring is sufficient to overcome the impact of the buoyancy force. Whilst in the stratified area away from shore, the water column structure is determined (at least in the first order) by the balance of vertical exchange processes and the buoyancy effect [Simpson and Sharples, 2012]. The tidal front is defined as a thin horizontal layer of well stratified water column and well mixed water column [Simpson, 1971]. The tidal front location is defined by the parameter $\frac{h}{u^3}$, where h is the water depth and u is the tidal current speed [Simpson, 1971].

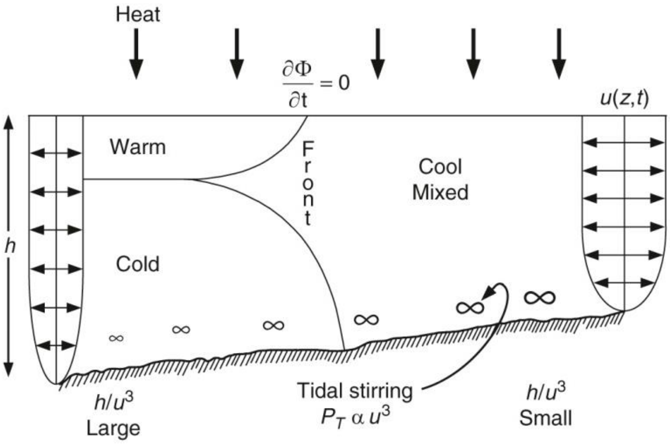

Fig 1.2 The example of sections of water stratification at the shelf seas. Right side of the tidal mixing front is the well mixed area, the near shore region, and the left side of the front is the stratified area where away from the shore. The barotropic tide *u(z,t)* flows recliner and provide the stirring at the sea bottom. The heat income from atmosphere to the sea surface generates a warm layer overlying cold layer. On the near shore side, water is well mixed, whilst at the off shore side, the water column experience seasonal stratification. [Simpson and Sharples, 2012]

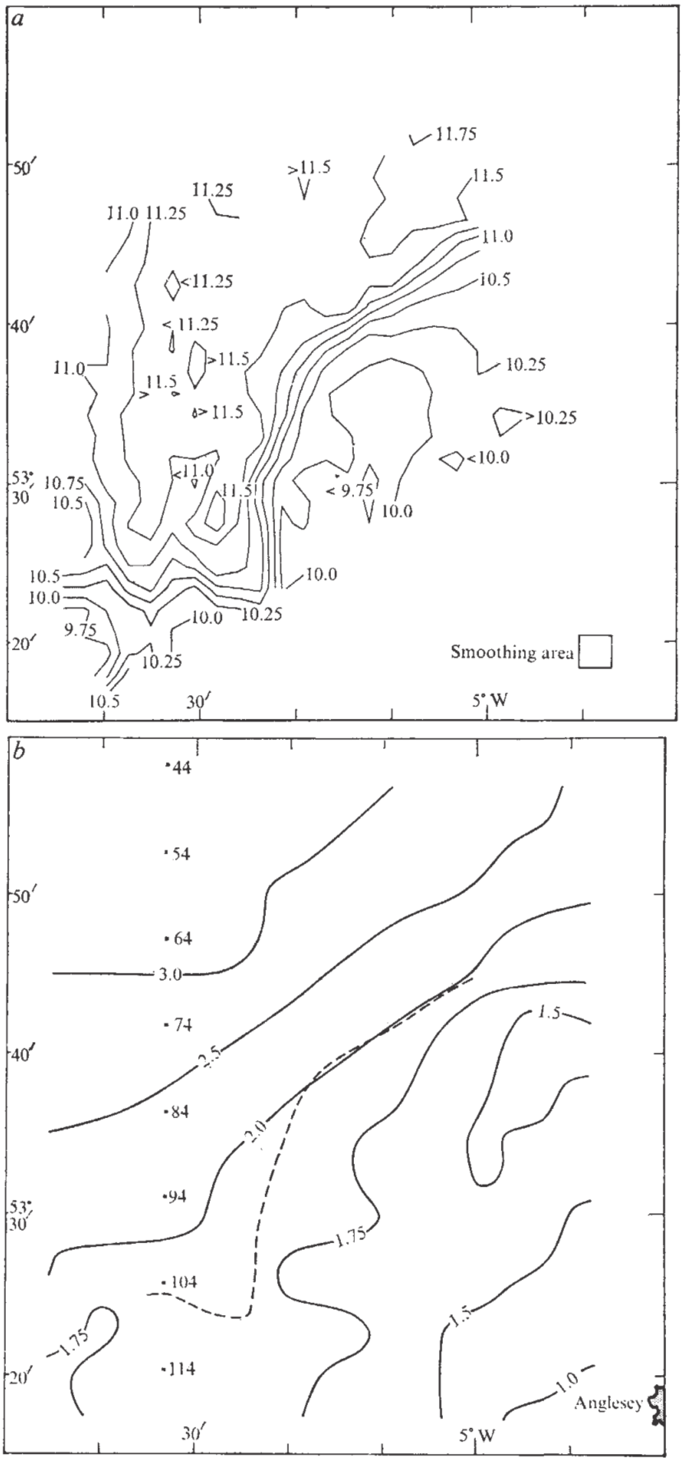

Fig 1.3 The bird’s-eye view of Irish Sea surface: a) contours of sea surface temperature on 5th June, 1973. b) contours of $\log_{10}(h/u^3)$, the dashed line indicates the position of tidal front. [Simpson and Hunter, 1974]

In the stratified area, the density structure of the water column is separated into two or more layers, with significant density variation over short vertical distances, and is defined as water stratification. Away from estuaries and coastal areas, the salinity in the shelf sea does not vary much with depth. Thus based on the equation of state for sea water (Chapter 5, equation 5.1), the vertical variation of density is highly dependent on the vertical variation of temperature.

The evolution of stratification and the water structure can be quantified through the stratification parameter *Φ* [Simpson and Sharples, 2012]. *Φ* is defined as the change in potential energy (PE) per meter of the observed water column compared to that of the same water column when it is completely mixed, which is:

$$\Phi = \frac{1}{h}\int_{-h}^{0}\left(\rho_m - \rho(z)\right)gzdz \tag{1.2}$$

Where ρ is the water density, ρ_m is the water density after well mixed, h is the water depth, z is the depth.

According to this definition, a larger *Φ* suggests a stronger stratification, and *Φ=0* when the water is well mixed. Additionally, this parameter provides an indication of the amount of energy input required to mix the water column.

The annual evolution of water column stratification in the seasonally stratified shelf seas is a result of the forcing balance between the buoyancy force and the mixing mechanism [Simpson and Sharples, 2012]. The key determining factor of buoyancy force is the solar heating. The origin of mixing has several sources, which includes the stirring effect from surface wind stress and bottom tidal stress. In the Northern Hemisphere in spring, due to the solar heating increase, the water starts to stratify and warm water begins to form at the surface, over the top of cold water (fig 1.2).

As the solar heating continues to increase in the summer, the temperature difference between the sea surface and the lower layer enlarges, and thus the thermocline develops. The developed warm surface layer introduces the increase of buoyancy force, which is eventually able to overcome the tidal and wind mixing, leading to the development of strong stratification which persists for the whole summer. This suggests that the stratified area in shelf seas is more likely to appear in an area with weak tides [Rippeth, 2005; Simpson, 1971].

The greatest stratification appears in summer with the stratification starting to break down in the autumn. At this time, a decrease in solar heating results in the heat flux at the air-sea interface to become negative, with the sea releasing heat to the atmosphere.

The temperature decrease at the sea surface causes the density of surface water to increase, which further contributes to the break down process through convective overturning. Another source of reduction in the stratification is thought to be related to the mixing in the thermocline which is caused by turbulence driven by the tide and the wind [Rippeth, 2005].

The increased wind in autumn and winter enhances wind drive mixing, which combined with the heat loss from sea surface reverses the buoyance force, and accelerates the water stratification break down [Rippeth et al., 2014]. This leads to the water column becoming well mixed in winter [Simpson and Sharples, 2012]. Thus, the models, even those which only include vertical exchange processes (i.e. 1-Dimensional models), can successful represent the evolution of stratification when they contain the key mechanisms of heating and cooling, and the mixing processes. Hence these processes are the first order controls of water column stratification.

An example of the annual cycle of stratification is shown in fig 1.4 [Simpson and Sharples, 2012], which displays the vertical temperature structure variation in a seasonally stratified shelf sea, the Nymphe Bank, Celtic Sea. Water temperature data was collected several times a week for the whole year, and adapted by Simpson and Bowers [1984]. The evolution of sea temperature is represented by the temperature difference between the sea surface temperature and the near bottom temperature. According to fig 1.4, stratification starts to form in April to May, is well developed from July to September, and eventually breaks down during December to March.

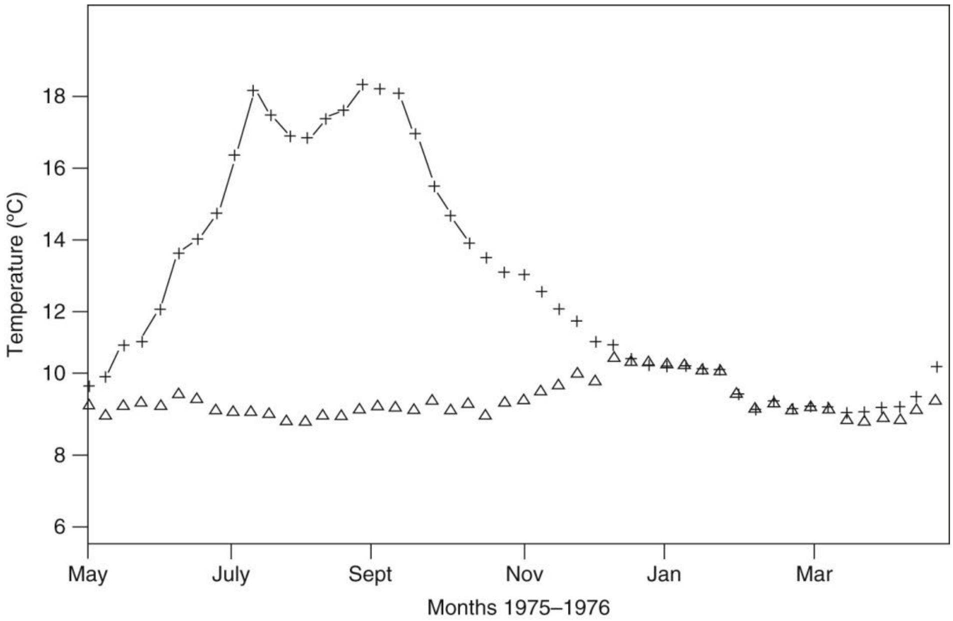

Fig 1.4 The temperature evolution at the sea surface (crosses) and near the sea bottom (triangles). The data is collected from a site at Nymphe Bank, Celtic Sea. The latitude is 50°40' N and the longitude is 7°30' W. The figure shows a whole year of the variation in the surface temperature and near bottom temperature, which shows the periods when the water column is fully mixed and well stratified [Simpson and Sharples, 2012].

1.3 The state of marginally stable

It is not only the convective mixing that occurs near the boundary of thermocline that could break down the stratification, the vertical mixing across the thermocline, which is defined as the diapycnal mixing, could help with the stratification break down as well [Rippeth et al., 2014]. The diapycnal mixing is driven by turbulence, which is a result of shear instability.

The appearance of shear instability is highly related to the local Richardson number Ri, which is the ratio of the shear and buoyancy frequency, and can be estimated by the following equation:

$$\mathrm{Ri} = \frac{N^2}{S^2} \tag{1.3}$$

$$N^2 = -\frac{g}{\rho}\frac{\partial \bar{\rho}}{\partial z} \tag{1.4}$$

$$S^2 = (\frac{\partial U}{\partial z})^2 \tag{1.5}$$

Where ρ is the water density, g is the acceleration due to gravity, U is the horizontal current speed and z is the depth. N^2 represents the effect of buoyancy, which is known as Brunt-Väisälä frequency squared, and S^2 is shear squared in the water column.

The term “marginally stable” [Rippeth et al., 2009] in some papers gives the name of near critical stability [Johnston and Rudnick, 2009; Brannigan et al., 2013], which is defined as the state where the local Richardson number Ri $\approx$ 1. Thus, in the stratified water column, when the Richardson number in the thermocline is close to 1, the thermocline is in a marginally stable state [Rippeth et al., 2005]. Fig 1.5 shows an example of a thermocline in a marginally stable state at a mooring site in the stratified western Irish Sea. The values of N^2 and S^2 are similar at the same depth across thermocline, thus Ri $\approx$ 1 across thermocline and flow at the mooring site is marginally stable.

In a marginally stable state an increase of local current shear will easily decrease the Ri [Thorpe and Liu, 2009]. Vertical current shear enhancement within the thermocline, can reduce Ri to < 0.25, triggering local shear instability and leading to the development of turbulence [Rippeth et al., 2009]. The turbulence will mix the water column, which will further reduce the vertical density gradients, thus decrease N^2 .However through viscosity, the turbulence will reduce velocity shear and increase Ri back to > 0.25 [Thorpe and Liu, 2009]. Thus the marginally stable state is maintained.

High resolution measurements of shear and stratification indicate that in the stratified shelf seas, the flow is marginally stable [Van Haren et al., 1999; Mackinnon and Gregg, 2005; Rippeth et al., 2005; Rippeth et al., 2009]. As described, in the marginally stable area (fig 1.5), an episode of enhanced shear will easily reduce Ri and lead to local shear instability, turbulence, and eventually diapycnal mixing in thermocline.

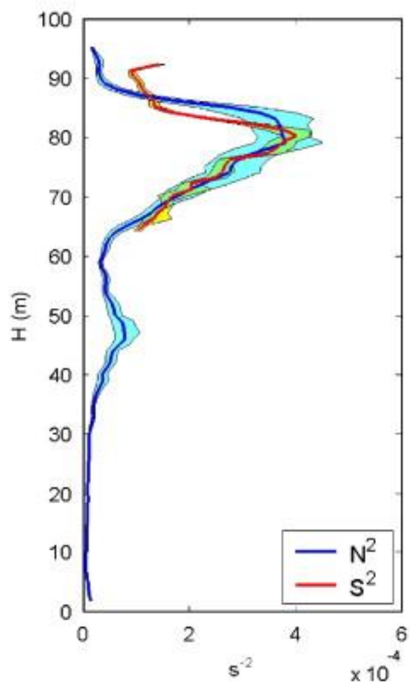

Fig 1.5 Example of a "marginally stable" state in the western Irish Shelf Sea, June 2002. The blue line represents the profile of buoyancy frequency squared (N^2) and the red line represents the profile of shear squared (S^2). The blue and green envelops are the 90% confidence limits for the buoyancy frequency and shear profiles, respectively. At the height of 65 m - 85 m, which is the height of thermocline, the gradient Richardson number $\mathbf{Ri} \approx \mathbf{1}$ suggesting that the thermocline is in a marginally stable state [Rippeth, 2005; Rippeth et al., 2009].

1.4 Drivers of the thermocline shear

As an important source of momentum in the ocean, wind stress has a great impact on the ocean surface mixed layer through inertial oscillation, which are energetic motions rotating in or close to the local inertial period. When the wind stress on the sea surface suddenly ceases or changes direction, the surface mixed layer oscillates at an inertial frequency over the lower mixed layer generating shear at the base of the surface mixed layer.

As described, periods of enhanced shear are potentially an important trigger for diapycnal mixing in the marginally stable shelf sea seasonal thermocline. Measurements reveal that the significant enhanced shears, called shear spikes, are 2-3 times larger than the normal shear before and after. As with normal shear, the shear spike vector rotates clockwise with a near local inertial frequency. The natural mechanism of a shear spike is considered as a result that comes from wind-shear direction alignment and destroyed by their opposition [Brannigan et al., 2013].

Rippeth et al. [2009] report a coincidence between shear enhancement and episodes of enhanced wind in the western Irish Sea, however this coincidence between wind and shear spikes is not always observed [Burchard and Rippeth, 2009]. D'Asaro [1985] noted that the wind and surface current alignment will create an increase in shear, Rippeth et al. [2009] observed that shear enhancement was accompanied by a 3 - 4 times increase in the turbulent dissipation rate, which coincided with wind-shear vector alignment in a shelf sea seasonal thermocline [Brannigan et al., 2013]. A similar increase of dissipation rate and shear enhancement were observed in the northern North Sea [Burchard and Rippeth, 2009] and in the ice-covered Laptev Sea [Lenn et al. 2011]. The increase in dissipation shows that the wind-shear alignment plays an important role in enhancing mixing across the seasonal thermocline [Rippeth et al., 2009].

The coincidence between shear spikes and the wind-shear vector alignment was examined by Burchard and Rippeth [2009] through a two-layer model. A model sensitivity analysis shows that in a marginally stable area, the effect of the shear vector, wind stress and bed stress alignment combines to form a shear spike. A study in an open ocean by Brannigan et al. [2013] reported a similar conclusion.

Lincoln et al. [2016] linked the shear spikes to the surface mixed layer deepening. During the period of enhanced shear, the Richardson number near the base of surface mixed layer is estimated to be below 0.25, which implies a correlation with shear instability and the surface mixed layer deepening. The model results, using a 1D vertical exchange model, also reveal a coincidence between shear spikes and the surface mixed layer deepening.

Shear generation in the thermocline in previous studies [Brannigan et al., 2013; Burchard and Rippeth, 2009] is related to boundary stresses. The bottom boundary stress is driven by the barotropic tide [Burchard and Rippeth, 2009] and the surface boundary stress is by the stress exerted on the ocean surface by the wind [Burchard and Rippeth, 2009; Brannigan et al., 2013]. In the shelf sea regime the relative importance of surface stress and bottom stress was quantified by Burchard and Rippeth [2009], and it is indicated that the wind stress, i.e. the surface stress, is the main driver of enhanced shear, and that the bottom stress can be neglected.

The generation of shear spikes is related to wind-shear alignment. When the direction of the wind and the shear does not align, shear will continue to grow, but at a decreasing rate. The growth will stop when the wind-shear direction reaches 90°. This is the point at which the rate of shear growth switches from positive to negative [Burchard and Rippeth, 2009; Lincoln, 2012; Brannigan et al., 2013].

Burchard and Rippeth [2009] used a model to investigate the sensitivity of shear development to different wind durations. The study shows that shear developed in short and intense wind events will generate a stronger shear spike than longer period events. In intense wind events, the most significant change is the intensity of the shear (which generates one large shear spike), whilst in longer wind events, a number of subsequent shear peaks are generated.

When the tidal current flows over the continental shelf break and continental shelf bank, it may trigger the phenomena of internal tide [Bell, 1974; Baines, 1982; Garrett, 2003]. Vertical mixing is often thought to be powered by internal tides rather than barotropic tide. The internal tide is thought to dominate the tidal contribution to mixing of thermocline, since it provides additional shear across the thermocline [Rippeth, 2005].

Not only will the baroclinic tide affect shear directly, but it will also interact with the effects of the wind on the generation of shear. Also, in the condition of clockwise rotating tides, the angle between the wind direction and the shear direction plays a more important role than the wind stress itself in enhancing shear. If the bulk shear is following the inertial oscillation motion in the Northern Hemisphere and rotating clockwise, the clockwise tides will strongly enhance the shear in contrast to the counter-clockwise tides which will suppress shear [Burchard and Rippeth, 2009].

Besides the effect of wind and tide, there is a 180° phase shift of current motion observed between the surface mixed layer and the lower mixed layer, which could also contribute to the enhanced shear [Rippeth et al., 2002; Rippeth et al., 2009]. Rippeth et al. [2002] reported a close to 180° phase difference at surface and lower mixed layers, the switch of phase observed occurs at the pycnocline (the same as thermocline). Similar observations are reported in earlier studies on the continental shelf of the Gulf of Lyons [Millott and Crépon, 1981] and in the North Sea [Maas and van Haren, 1987]. Results from a 1D two-layer model shows the same conclusion as the 180° phase difference between the surface and the lower mixed layers is reproduced by the model, where the phase lag is gradually varying with depth. This 180 ° phase shift is proved to be related to the boundary coastal condition. The barotropic surface slope resulting from the applied wind stress, together with the existence of the coastal boundary are the determining factors for the 180 ° phase shift [Krauss, 1979; Craig, 1989; Rippeth et al., 2002; Simpson et al., 2002; Shearman, 2005].

1.5 Structure of the thesis

This study aims to investigate the relative roles of the wind and the tide in generating shear across thermocline within seasonally stratified shelf seas. The bulk shear over the thermocline, which is defined as the average of the shear in two defined layers which are either side of the thermocline, is important in the seasonally stratified shelf sea. The bulk shear is particularly important for these locations as the water stratification is in a marginally stable state, thus the increase of shear, which is the shear spike, could significantly decrease the Richardson number. Once the Richardson number decreases below 0.25, turbulence occurs at the thermocline resulting in diapycnal mixing. Thermocline shear has been shown to result from wind stress at the sea surface [Burchard and Rippeth, 2009]. In our study we will use rotary spectral analysis, 1D modelling, and a sensitivity analysis to examine the relative roles of the wind and the tide in generating shear.

The structure of the thesis is as follows:

- Chapter 2 - The methods applied to investigate the processes responsible for diapycnal mixing in the thesis are introduced. The three key analysis methods are rotary spectral analysis, correlation analysis and coherence analysis.

- Chapter 3 - The two models used in the study are introduced. They are a 1D two-layer vertical dynamic numerical model and a 1D turbulence closure numerical model. The key differences between the models and the philosophy applied to the modelling are introduced in this chapter.

- Chapter 4 - The analysis of the observational data collected in the western Irish Sea during the onset of stratification are presented. The data collection, the stratification background and the key driver of bulk shear under this scenario is described. The two-layer model is employed to replicate the shear production in the thermocline and the separate impacts on shear production from the surface stress and the bottom stress are investigated. A coherence analysis is applied to investigate at which frequencies the modelled results and observations have the greatest similarity, in order to help assess the model skill when applied in different sea areas.

- Chapter 5 - A contrasting dataset collected from the seasonally stratified northern North Sea, during the breakdown of stratification, is analysed in this chapter. Similar analyses and model application are applied here as in Chapter 4. The water stratification in this chapter goes from full development towards the process of breaking down. The key driver of bulk shear is found to have a great difference compared with those in Chapter 4.

- Chapter 6 - A model sensitivity analysis is employed in this chapter to aid elucidation of the key results obtained in chapters 4 and 5. Four parameters are tested in the sensitivity analysis: the water depth, the thermocline depth, the depth ratio and the thermocline thickness.

- Chapter 7 - Here an interesting period of observations are examined where neither the wind nor the barotropic tide can explain the observed shear spikes.

- Chapter 8 - This chapter brings together and synthesizes the main results from the previous chapters and provides a discussion of the directions for future work.

Chapter 2

Analysis methods

In this chapter, we will provide an outline of the analysis methods which are applied in the following subsequent chapters, to understand the processes responsible for the diapcynal mixing in the seasonal thermocline of temperate shelf seas.

2.1 Calculation of bulk parameters

This section provides a brief introduction to the data used to investigate the bulk shear across the thermocline. The data used in the study are the sea water temperature, the sea water salinity, the water current velocity and the wind speed and direction at a height of 10 m above the sea surface.

The water temperature includes two types of data, one is the time series of the evolution of water temperature, and the second is vertical profiles of temperature at the beginning and the end of the observational period. CTDs were applied to collect the salinity profiles at the beginning and the end of the observational period. The salinity data collection in WIS and NNS will be introduced in Chapters 4 and 5 respectively. The temperature time series profile data provides information on water stratification and the position of the thermocline. The two temperature profiles, together with coincident profiles of salinity are used to estimate the density profile based on the state equation (Chapter 5, equation 5.1). Furthermore, this analysis can be used to reveal which parameter (temperature or salinity) dominates the variation in the density.

The current velocity data was collected using acoustic Doppler current profilers (ADCPs), which provide data from the bulk shear, the barotropic current, and barotropic tide; from this data the baroclinic current and tides can be estimated. The current velocity in the surface and lower mixed layers are compared with the wind and barotropic tide velocities to investigate the relationship between the boundary forcing and the current as well as the relationship of the boundary forcing and the bulk shear. The barotropic tide is used to estimate the bottom stress.

Two sources of wind data are used in this study from two sources. One is from direct observation, whilst the second is from the Met Office 3 hourly reanalysis data. The wind data from the observations was measured on the Frigg oil rig using an anemometer fixed at 10 m height above the sea surface. The wind data is used to estimate the surface stress, for comparison with the bulk shear and the surface current. The wind data is also used in the coherence analysis and correlation analysis together with model predictions to investigate the relationship between the wind and the bulk shear, and also the relationship between the wind and the current.

Detailed information of data collection, for example where and when the measurements were made, and which instruments were involved in the measurement, will be provided in the following chapters (Chapters 4 and 5).

The surface stress, bed stress and bulk shear are being calculated before doing the analysis. Detailed information for those calculations is as follows:

2.1.1 Surface stress

Surface stress is the transfer of momentum from the wind to the ocean surface. In our calculation, the surface stress (from the water side not the air side) is considered to be identical to the wind stress, thus the calculation of surface stress could follow the equation of wind stress as:

$$\tau_s = \rho_{air} C_{D10} U_{10}^2 \tag{2.1}$$

Where τ_s is the wind stress, $\rho_{air} = 1.3\ kgm^{-3}$ is the air density， C_{D10} is the surface drag coefficient and U_{10} is the wind speed at 10 m height. The calculation of C_{D10} is as follows [Yelland and Taylor, 1996]:

$$1000C_{D10} = 0.29 + \frac{3.1}{U_{10}} + \frac{7.7}{U_{10}^2} \quad (3 \leq U_{10} \leq 6\ ms^{-1}) \tag{2.2}$$

$$1000C_{D10} = 0.60 + 0.070 \times U_{10} \quad (6 \leq U_{10} \leq 26\ ms^{-1}) \tag{2.3}$$

What can be seen from equations 2.2 and 2.3 is that different functional dependence on wind speed.

2.1.2 Bed stress

The bed stress is a result of the interaction of the bottom flow with the sea bed. The bottom flow is dominated by the barotropic tide, and leads to the generation of a bottom boundary layer. If we assume the current close to sea bed is due only to the barotropic tide, the bed stress τ_b is estimated by [Burchard and Rippeth, 2009]:

$$\tau_b^x = C_{Db} U_{bt} u_{bt} \tag{2.4}$$

$$\tau_b^y = C_{Db} U_{bt} v_{bt} \tag{2.5}$$

$$U_{bt} = \sqrt{{u_{bt}}^2 + {v_{bt}}^2} \tag{2.6}$$

Where u_{bt} and v_{bt} are the northern and eastern components of barotropic current, U_{bt} is the magnitude of barotropic current, C_{Db} is the bed drag coefficient.

The value of C_{Db} varies with different bathymetry conditions, and can be estimated by [Easton et al., 2012]:

$$C_{Db} = \frac{g}{(Mh^{1/6})^2} \tag{2.7}$$

Where M is the Manning Roughness, g is the gravitational acceleration and the h is the local water depth. In shelf seas, C_{Db} is normally set at a value between 0.0015 - 0.0025 [Pugh, 1987]. In order to compare my results with the results from early researchers, the values of C_{Db} are set with different values in western Irish Sea and northern North Sea. The value of C_{Db} in western Irish Sea is set as 0.0025 [Lincoln, 2012] and in the northern North Sea 0.0015 [Simpson and Sharples, 2012].

2.1.3 Bulk shear

Shear is the vertical gradient of the horizontal velocity difference across adjacent layers in the ocean. The focus of our study is the shear at the thermocline. However, it is often difficult to accurately observe shear at the thermocline since the thermocline can be a thin layer relative to the resolution of the measurements of velocity. Also, the depth of the thermocline will vary over a range of timescales from tidal to seasonal and so the depth of moored current meters will vary relative to the thermocline. To gain consistency in representing the shear, a bulk shear is defined as representative of the shear across the thermocline. The bulk shear is the average of shear in two defined layers which are either side of the thermocline. We are therefore assuming that the water current velocities are identical in any place in each mixed layer and equal to the mean current velocity of that layer. Based on these assumptions, the bulk shear can be used to represent the shear across thermocline.

The bulk shear is calculated as the velocity difference between defined upper and lower layers, separated by a certain distance which is from the central upper layer to the centre of the lower layer, the equation and the diagram are as follows:

$$S_{bk} = \frac{\overline{U}_s - \overline{U}_b}{h_{diff}} \tag{2.8}$$

Here, S_{bk} is the bulk shear, $\overline{U}_s$ is the mean velocity of surface mixed layer, $\overline{U}_b$ is the mean velocity of lower mixed layer and h_{diff} is the height difference between the centers of two layers.

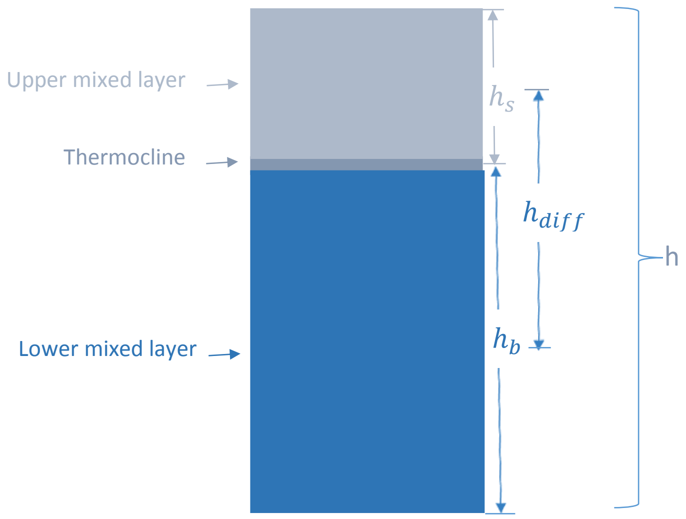

Fig 2.1 An example of how we define the upper mixed layer, lower mixed layer and h_{diff} in the water column. The water depth is defined as h. The upper and lower mixed layers are separated by a thin thermocline. The water column thickness of upper and lower mixed layers are defined as h_s and h_b, respectively. To simplify the definition of h_s and h_b the thermocline is defined as a thin layer at certain constant depth with a constant thickness, however in reality, the thermocline depth and thickness varies with time. The height difference between the centers of the upper and lower layer is defined as h_{diff}.

The height difference of two layer centers h_{diff} varies as stratification evolves, the upper and lower extent over which the bulk shear is estimated is based on the height and thickness of the thermocline and the coverage of the ADCP. In the following subsequent result chapters (Chapters 4 and 5), h_{diff} varies according to the study area, in each study area the values of h_{diff} will be introduced.

2.2 Analysis methods

Two main analysis methods are applied in this study, the rotary spectral analysis and the coherence analysis.

2.2.1 Fourier transform

Fourier transform is a widely used statistical analysis method for time series analysis to identify the component frequencies of variability [Emery and Thomson, 1998]. It transforms the data from the time domain to the frequency domain (fig 2.2). Assuming that time series variability is the complex mixing of several sine waves with different amplitudes and phases. After Fourier transform, the time series variability is displayed as frequency series variability and the x-axis is switched from time to frequency. The Fourier transform reveals which wave components dominant in the time series variability and at which frequency there will be greatest energy concentration.

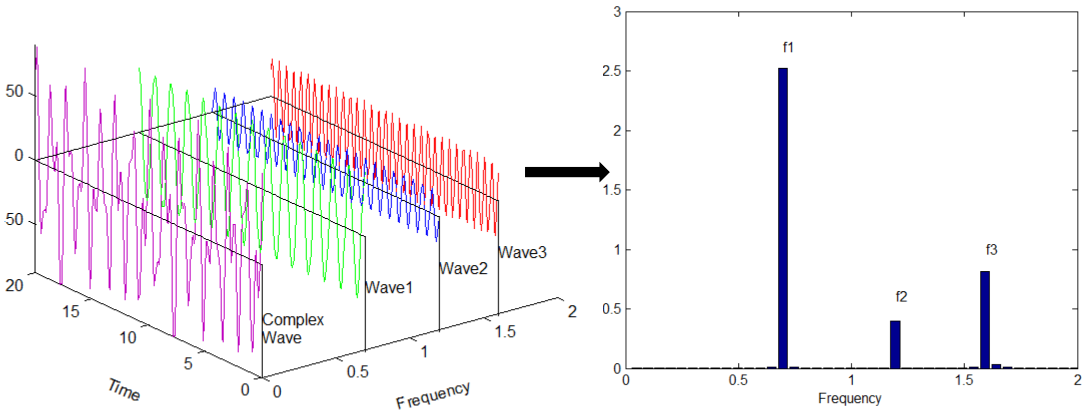

Fig 2.2 An example of Fourier transform. Assuming a complex wave is built by three simple sine waves: wave1, wave 2 and wave 3. The frequencies for the three waves are f1, f2 and f3 respectively. The Fourier transform is transforming the time series complex wave from the time domain (left panel) to the frequency domain (right panel) and splitting the simple sine waves (f1, f2 and f3) from the complex wave. The height of the bars in the right panel shows the relative amplitude of the three simple sine waves.

The basic idea of Fourier transform is to assume every complex signal can be divided into several sine or cosine form signals [Emery and Thomson, 1998], by the form:

$$y(t) = \overline{y(t)} + \sum_p [A_p \cos(\omega_p t) + B_p \sin(\omega_p t)] \quad (2.9)$$

which $\overline{y(t)}$ is the time averaged value, A_p and B_p are the Fourier coefficients, ω_p is the frequency. P represents there are p frequency components for the signal $y(t)$.

The component frequencies ω_p, is defined by the time length T of the time series data, which is:

$$\omega_p = 2\pi f_p = 2\pi p f_1 = 2\pi p \frac{1}{T} \qquad (p = 1,2,3 \ldots) \quad (2.10)$$

Where $f_1 = \frac{1}{T}$

While

$$A_p = \frac{2}{T}\int_0^T y(t)cos(\omega_p t)dt \qquad (p = 0,1,2 \ldots) \quad (2.11)$$

$$B_p = \frac{2}{T}\int_0^T y(t)sin(\omega_p t)dt \qquad (p = 1,2,3 \ldots) \quad (2.12)$$

Thus, the Fourier series is expressed by the following form:

$$y(t) = \overline{y(t)} + \sum_{p=1}^{\infty} C_p cos(\omega_p t - \theta_p) \quad (2.13)$$

$$C_p = (A_p^2 + B_p^2)^{1/2} \qquad (p = 0,1,2 \ \ldots) \quad (2.14)$$

$$\theta_p = tan^{-1}[B_p/A_p] \qquad (p = 1,2,3 \ldots) \quad (2.15)$$

It is worth noting that before applying Fourier transform the Shannon-Nyquist sampling theory should be satisfied [Emery and Thomson, 1998]. The Shannon-Nyquist sampling theory states that the sampling frequency should be greater than twice the maximum frequency in the time series variability (equations 2.8), otherwise the result of the Fourier transform will not be able to reflect the full range of information in the original time series variability.

$$f_s \geq 2f_{max} \quad (2.16)$$

The sampling frequency f_s is calculated as:

$$f_s = \frac{1}{dt} \quad (2.17)$$

Here dt is the sampling time interval.

The main frequencies interested in our study are that of the principle semidiurnal tide, the M2 tidal frequency (0.0805 cycles per hour), local inertial frequencies for western Irish Sea (WIS) site (0.0674 cycles per hour) and northern North Sea (NNS) site (0.0719 cycles per hour). Thus the threshold for identifying M2 tide, local inertial frequencies of western Irish Sea and northern North Sea are 0.161 cycles per hour, 0.1248 cycles per hour and 0.1438 cycles per hour respectively. The ADCP sampling frequency for each site is 5 minutes (12 measurements per hour, in WIS) and 10 minutes (6 measurements per hour, in NNS), which are much larger than the threshold value for the identification of the M2 tidal frequency and the two local inertial frequencies. Thus, the frequency resolution issue is not a concern in this study.

For determining the minimum length of the time series to separate two frequencies, another threshold is required to be followed [Emery and Thomson, 1998]:

$$|f_1 - f_2| > \frac{1}{T} \tag{2.18}$$

Where f_1 and f_2 are the frequencies of the two signals, and T is the time series length for the observed data.

In the western Irish Sea, to identify the M2 frequency and the local inertial frequency, the time length threshold is 76.3 hours (3.18 days), and in the northern North Sea the time length threshold 116.3 hours (4.84 days). The time length of the observed current velocity data in the western Irish Sea is 51 days and in the northern North Sea it is 55 days, both of which are much larger than the threshold. In both cases the time series are of sufficient length to allow the separation of the tidal and inertial signals.

Here we will apply Fourier transform with a built-in Matlab fast Fourier transform (FFT) function (fft.m) to transfer the imaginary bulk shear time series data ($ushear + i * vshear$) into the frequency domain.

2.2.2 Rotary spectral analysis

The rotary spectral analysis shows the relative power spectral density distribution with frequency. The Fourier transform provides the amplitude and phase of the signal components of the different frequencies which dominate. The distribution of amplitude squared with frequency represents the distribution of power with frequency, which is the power spectrum.

We consider the rotation to be formed by several circular motions with different diameters and frequencies. Take the inertial current as an example (fig 2.3), theoretically it should be one simple clockwise rotation in the Northern hemisphere.

However, in reality the inertial current (left panel) is combined with many other clockwise and counter-clockwise motions (right panel) rather than just being one pure inertial current. By using rotary spectral analysis, we can separate out the circular motions which are overlaid to form the complex circular motion, and also identify their sense of rotation, clockwise or counter clockwise. This technique provides a useful method for describing how currents rotate with time. The spectral analysis technique selected will therefore depend on the type of motion being analysed.

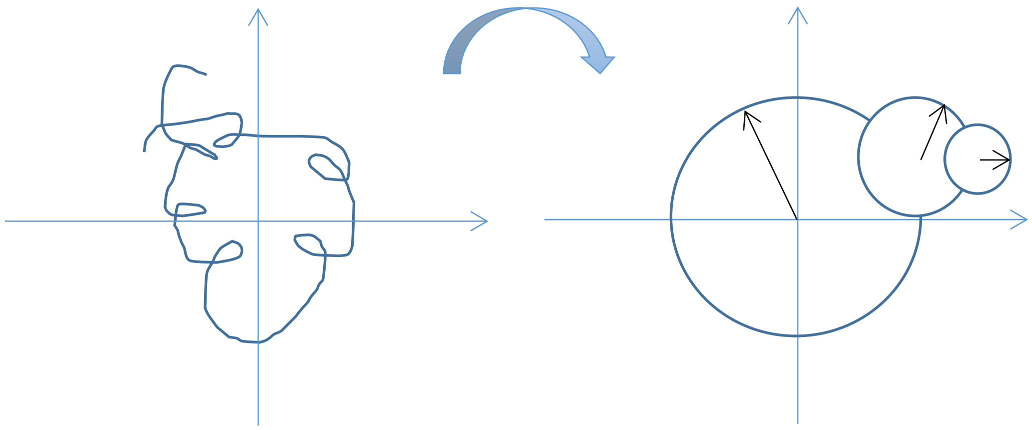

Fig 2.3 An example of rotary spectral analysis. Rotary spectral analysis transforms the time series variabilities from the time domain to the frequency domain based on Fourier transform. It decomposes a complex circular motion (left panel) into several simple uniform circular motions (right panel) with different frequencies.

Fig 2.4 reveals the distribution of relative power spectral density (PSD) with frequency. X-axis of rotary spectral analysis is the frequency, y-axis is relative PSD. The PSD shows the frequencies at which the energy is concentrated, and thus the dominant frequencies can be used to provide quantitative links to the forcing frequencies, i.e. the tide, the local inertial oscillations etc. Furthermore, the driver of this dominant component will be the dominant driver of our study, the shear. Thus this mechanism of the dominant shear frequency is the mechanism of dominant driver.

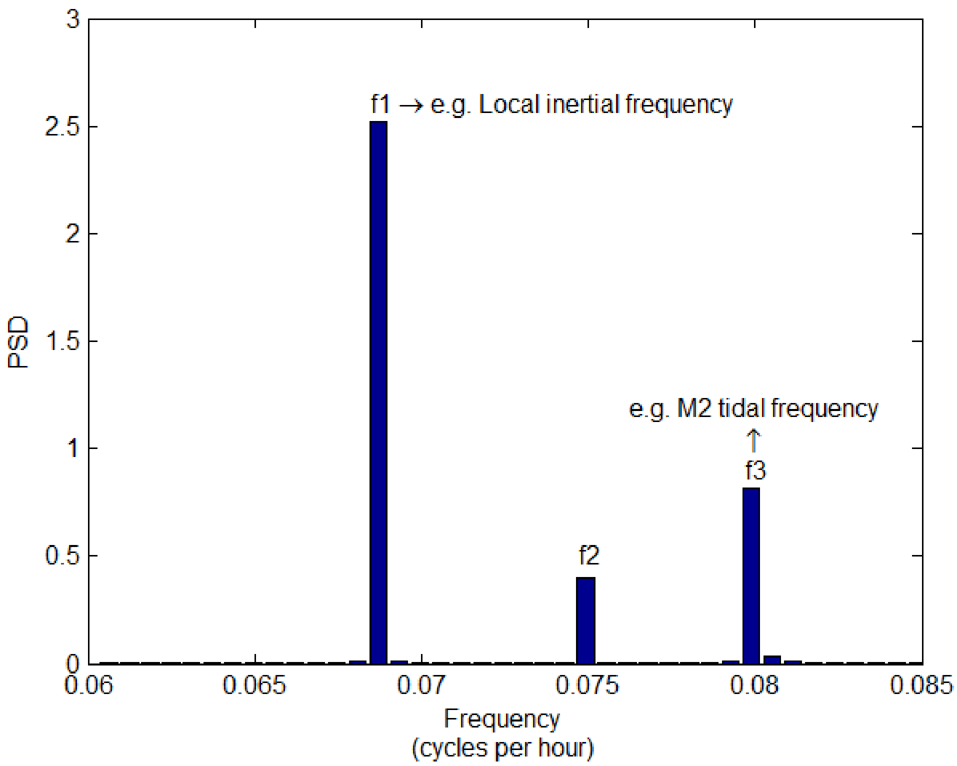

Fig 2.4 An example of the distribution of relative power spectral density (PSD) with frequency. f1, f2 and f3 are three identified frequencies from rotary spectral analysis. Assuming that f1 is the local inertial frequency and f3 is the M2 tidal frequency, the rotary spectral peak at these frequencies could suggest a driving relationship to the data analysed from the wind and M2 tide.

However, the 'driver' may not share the dominant frequency with the resultant motion. A simple example to explain the difference in frequencies between two related phenomena is that there are several different ways for the wind to drive ocean currents. For example, one way is for the wind force ocean current directly through surface wind stress [Simpson and Sharples, 2012]. A long period constant (constant in direction) wind blowing over an area of the ocean will drag the movement of water. The other way for wind to affect the ocean is indirectly, for instance through inertial current [Simpson and Sharples, 2012]. Wind offers an initial speed to an ocean current in a very short time, after the short forcing, the wind stops or turns to other directions, and the Coriolis force helps the current to maintain the rotating movement, which is the inertial oscillation. In the second scenario, even though the frequency of water movement is different from the frequency of wind, we still consider that the movement is related to the wind and that is where the frequency difference comes from.

2.2.3 Coherence analysis

The coherence analysis reveals the linear correlation of two time series variabilities, which is the similarity of two time series in frequency domain. Coherence is calculated by the following equations [Emery and Thomson, 1998]:

$$Cov_{xy} = E\{[X - E(X)][Y - E(Y)]\} = E[XY] - E[X]E[Y] \tag{2.19}$$

$$C_{xy} = \frac{Cov_{xy}}{\sqrt{Cov_{xx}Cov_{yy}}} \tag{2.20}$$

The peak in the coherence shows the frequency of the strongest correlation. While the trough, which is usually ignored, suggests the frequency of the smallest correlations.

For example, if there are three time series variabilities: data1, data2 and data3 (fig 2.5), the variability of each is formed by three simple sine form constituents. Data1 with the frequency of constituents 1 Hz, 2 Hz and 3 Hz, data2 with the frequency of constituents 1 Hz, 4 Hz and 5 Hz, and data3 with the frequency of constituents 4 Hz, 2 Hz and 8 Hz. Thus, the data1 and data2 shares the common frequency of 1 Hz, and data 1 and data 3 shares the common frequency of 2 Hz. The coherence analysis is applied between data1 and data2, data1 and data 3 (fig 2.5). The results are named as coh12 and coh13 respectively.

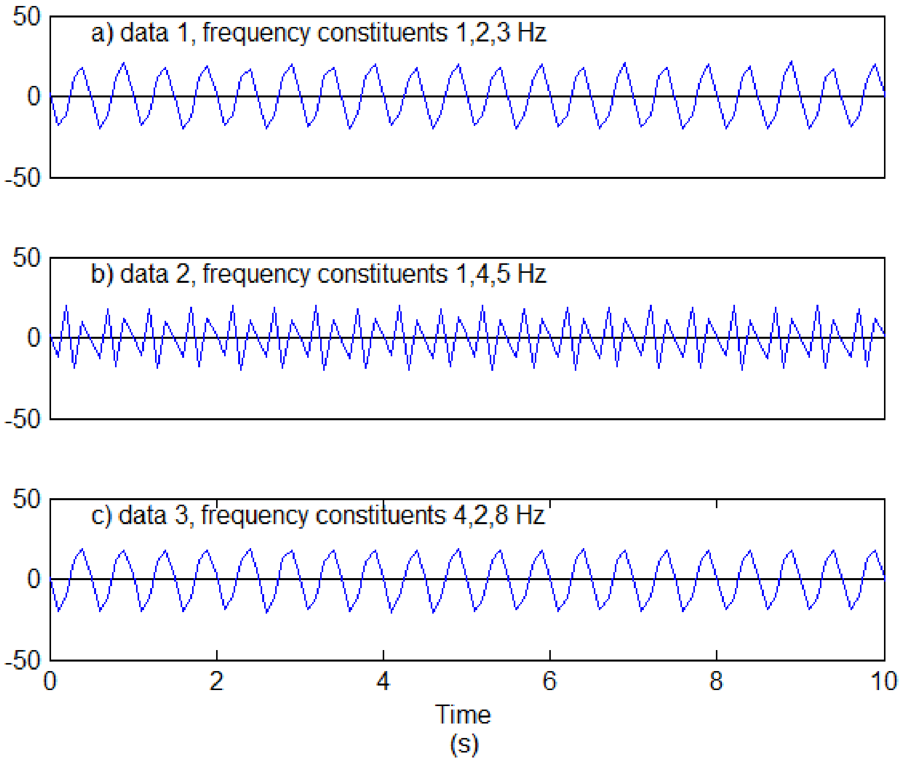

Fig 2.5 Three time series variabilities represented by data1, data2 and data3. Each of the time series variabilities are formed by three simple sine form time series variabilities with different frequencies. Data1 is formed by the constituents with frequencies of 1, 2, 3 Hz, data2 is formed by the constituents with frequencies of 1, 4, 5 Hz, and data3 is formed by the constituents with frequencies of 4, 2, 8 Hz.

Fig 2.6 shows the result of coherence analysis between data1 and data2, coh12 in panel a, and between data1 and data 3, coh 13 in panel b. Data1 and data2 share a common frequency of 1 Hz and in panel a, the most significant peak of coh 12 is located at 1 Hz and the coherence is 1. The data1 and data3 share a common frequency of 2 Hz and as shown in panel b, the most significant peak of coh 13 is at 2 Hz and the coherence is 1.

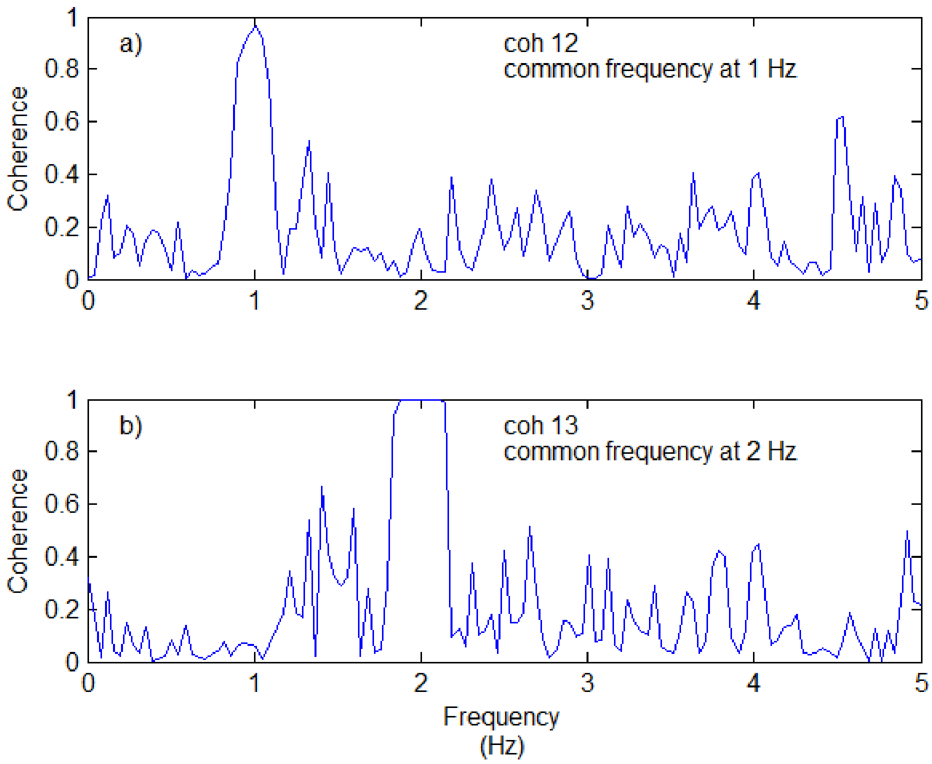

Fig 2.6 Example of the coherence analysis of time series variabilities from fig 2.5. Panel a is the coherence analysis between data1 and data 2, which is defined as coh12. Panel b is the coherence analysis between data1 and data 3, which is defined as coh13. The greatest peak of coh12 is at frequency of 1 Hz, which is the common frequency shared by data1 and data2. The greatest peak of coh13 is at frequency of 2 Hz, which is the common frequency shared by data1 and data3.

In physics, the similarity between two time series could suggest that one data set represents the forcing whilst the other represents the response, from which we would say that this high similarity represents a driving relationship. The low similarity frequencies suggest that these two components are not linearly related at that frequency. In the coherence analysis, as the similarity is based on the frequency domain, the driving relationship between the two parameters could be regarded as limited by frequency. In a certain frequency range, one parameter is driven by the other, but in the other frequency range, these two parameters are not related. For example, if the shelf sea water current velocity is related to the wind and tide, the coherence analysis between the current velocity and tide stress will show a peak value at tidal frequency, but not at other frequencies.

Even though all the coherence analyses shows are the similarity of the two data in the frequency domain, the result of coherence analysis could have a different physical meaning. The significant coherence between two observed time series data implies either that one data is responsible for driving the other, or that they are both driven by the same forcing. If significant coherence is found between an observed signal and a modelled signal, this similarity implies the model's ability to reproduce the key mechanisms that cause the variability. For example, if the coherence analysis of a modelled shear production and an observed shear production shows a peak at inertial frequency, the model can be claimed to contain the key mechanism that contributes to the shear production at inertial frequency.

It is worth noting that the coherence analysis should be used with caution. It is easy to regard the method as standard for determining the dominant driver, however this may not be that case. Take a coherence analysis in a later chapter as an example (in Chapter 5). Fig 2.7 shows the coherence analysis of shear squared production from the wind-only driven model and the evolution of bulk shear squared from observation. A significant peak before inertial frequency (IF) is shown in fig 2.7, however this peak has no physical meaning. More detailed information of this coherence analysis result can be found in Chapter 5.

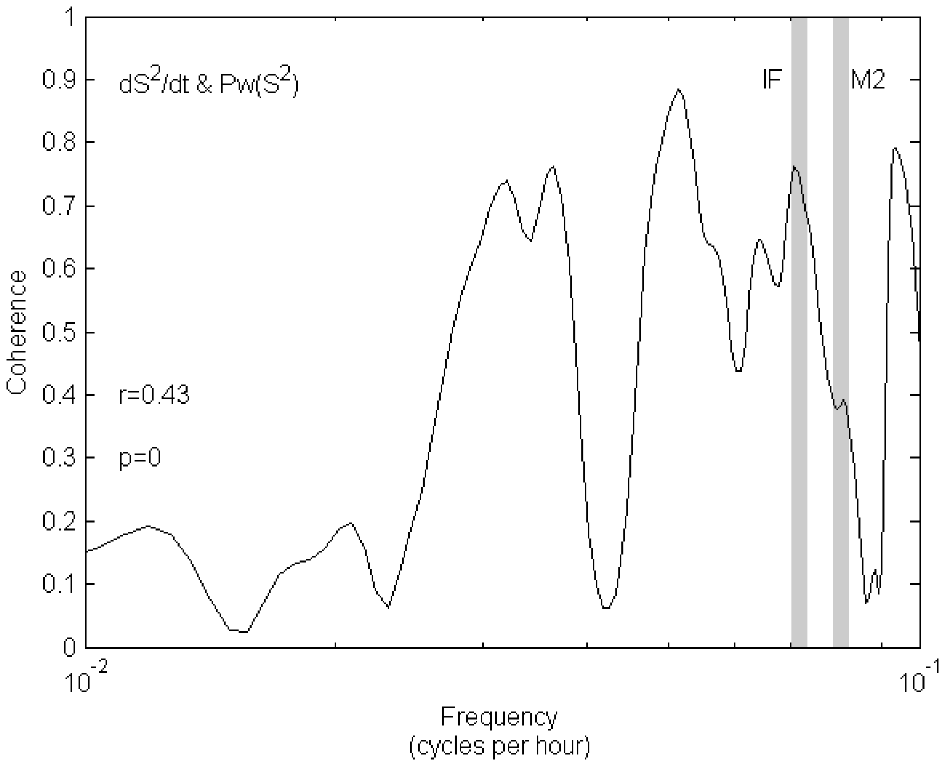

Fig 2.7 An example of when the greatest peak of coherence analysis does not represent the driving frequency of the analysed data. This is the coherence analysis between modelled production of shear squared and the evolution of observed bulk shear squared from Chapter 5. The two grey bars show the position of local inertial frequency and the M2 tidal frequency. The greatest coherence appears before local inertial frequency but this peak does not represent a driver with the certain frequency. The reason for the appearance of the greatest peak is explained in Chapter 5.

P value (Probability value) from correlation analysis is a useful parameter in the quantification of the results of the coherence analysis. A '*p* value' smaller or equal to 0.05 suggests the results of coherence analysis is reliable, otherwise the results are invalid.

2.3 Different strategies of defining thermocline

Theoretically, the bulk shear does not 100% represent the shear. The difference between the bulk shear and the shear could be enlarged by an improper selection of thermocline. However, using bulk shear is acceptable in our study of driver of shear across thermocline. The following three strategies of estimating bulk shear helps to explain: how the use of bulk shear helps simplify the calculation without introduce errors.

Three different strategies to estimate bulk shear are shown in the following figure. The figure is the time series of temperature profile, whilst the white lines represent thermoclines. The strategy a is to set thermocline at a constant depth, with a narrow thermocline thickness (area between white dotted lines). As the thermocline deepening during the study period, time averaged depth was selected. The strategy b is the thermocline depth evolves with time (white solid bars represents the position of thermocline), thus the thickness of surface mixed layer and lower mixed layer are variable too. The strategy c is the thermocline at a constant depth with a larger thickness (area between white dashed lines), which covers most of the real thermocline variation area during the period of interest.

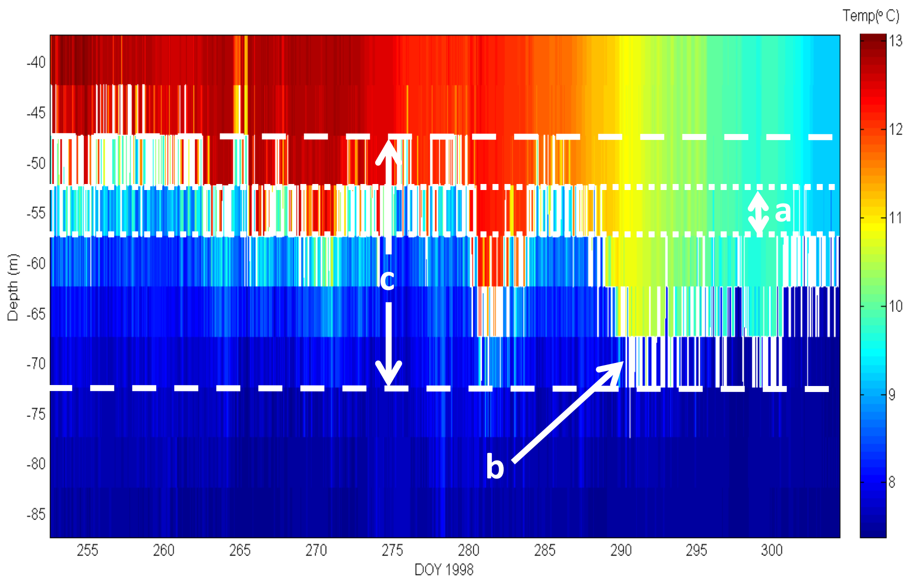

Fig 2.8 The time series of water temperature profile, which is used defining thermocline through three different strategies. The strategy a is to set thermocline at a constant depth, with a narrow thermocline thickness (area between white dotted lines). As the thermocline deepening during the study period, time averaged depth was selected. The strategy b is the thermocline depth evolves with time (white solid bars represents the position of thermocline), thus the thickness of surface mixed layer and lower mixed layer are variable too. The strategy c is the thermocline at a constant depth with a larger thickness (area between white dashed lines), which covers most of the real thermocline variation area during the period of interest.

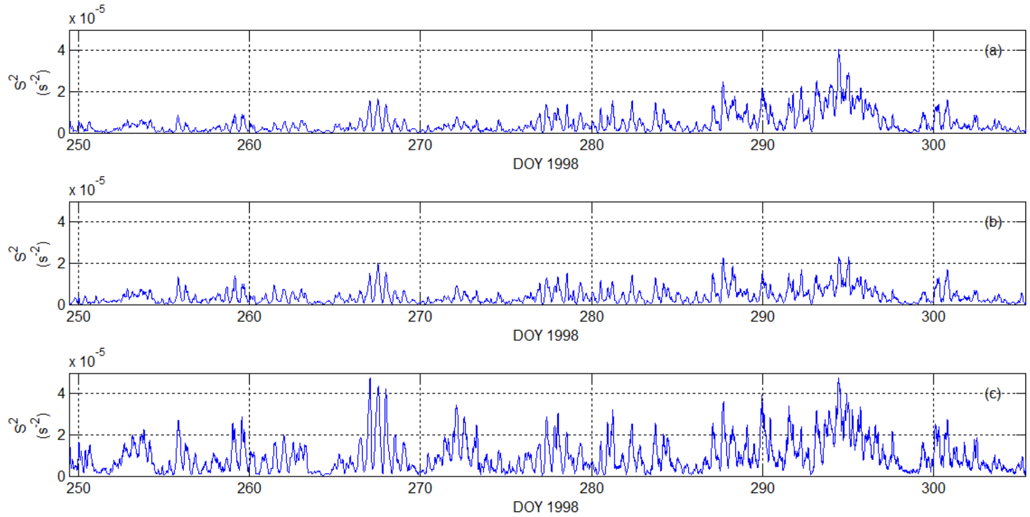

Fig 2.9 The bulk shear squared estimated from strategies a, b and c. The bulk shear is greater through the period of interest by strategy c than by strategies a and b. Comparing panel a and b, the intensity of bulk shear does not vary much expect for days 290 - 300. In panel c, the intensity of bulk shear in greater in general, especially during days 265 - 270 and 290 - 300.

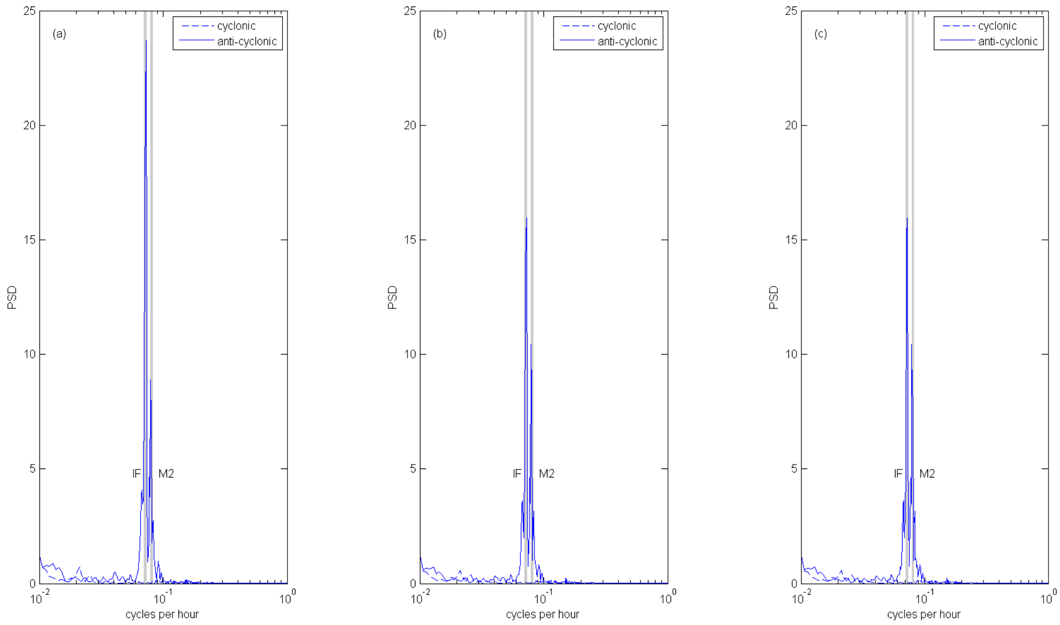

Fig 2.10 The rotary spectrum analysis of bulk shears from strategies a, b and c. All three strategies show the same dominant frequency of inertial frequency. The relative power densities of inertial frequency and M2 tidal frequency are similar in strategies b and c.

As can be seen from figs 2.9 and 2.10, the three strategies of selecting thermoclines result to different intensity of estimated bulk shear spikes, however, the dominant drivers of the bulk shears are the same which are all the inertial frequency dominated even though with different relative power density of local inertial frequency and M2 tidal frequency.

The rotary spectrum analysis by strategy c, with a thick thermocline that covers all the variation of thermocline depth, is closer to the strategy b, with a varied thermocline depth and closer to the shear in the real ocean. Thus, a thicker thermocline (c) is more preferable than a thinner thermocline (a). However in particular, when the collected data are limited at surface layer or bottom layer, or when the thermocline of thickness does affect the study object, or the estimated results need to compare with the model result which has a thin thermocline, under these conditions, in the study of driver of shear, a thinner thermocline, even though it does not cover all the thermocline depth variations, is still acceptable.

Chapter 3

Methodology: 1D Numerical Models - Two-Layer Vertical Dynamic Model and Turbulence Closure Model

Two numerical models are introduced in this chapter: the 1D Two-Layer Vertical Dynamic Model and the 1D Turbulence Closure Model. The difference of physics for the two models are: in the 1D Two-Layer Vertical Dynamic Model, the ocean responds to the two slabs of the sea surface and the sea bed, interaction inside the water column is not included in the model. In the 1D Turbulence Closure Model, the variation in vertical structure, especially inside the water column, was resolved through a turbulence closure scheme. The key idea of 1D Two-Layer Vertical Dynamic Model is to provide impact on shear production from the wind and tide. The 1D Turbulence Closure Numerical Model is used for the following aims: 1. to investigate the vertical mixing mechanisms in the ocean; 2. to estimate the effects of the wind and tide on shear production in the thermocline.

3.1 The philosophy of modelling

Before the employed models are introduced, it is necessary to describe the philosophy of modelling. Modelling is a powerful tool for assessing the importance of individual physical processes in the ocean, and also to study the interactions of the physical processes. The final goal of modelling is to develop a model which could represent all the hydrodynamic physics in the ocean. However this has not been achieved yet.

Consider that every single complex phenomenon in the ocean, for example shear, is built up by several simple components with different frequencies. In the real ocean it is too complicated for a single model to reflect the components of all frequencies for even one phenomenon. Based on that, the simplification must be adopted in the construction of the model. An over simplified model will fail to reflect the targeted subject, however an overly complex model is a waste of calculation resources. The Occam's razor principle, states that the simpler theories or models are preferable compare with the more complex ones, as long as the simplification does not cause a significant difference of the modelled outcome. This is a guide for model simplification, which suggests the model should keep the main dynamic mechanisms whilst ignore the less important ones [Rippeth, 1993]. The criterions of importance of the dynamic mechanism based on Occam's razor principle in modelling could be represented by:

1. the model skill to reproduce the phenomenon in the real ocean. The failure of model in reproducing the reality (the general pattern, not every single detail) must indicate there are some key physical mechanisms missing in the model.

2. The power density of spectrum analysis at each frequencies of the phenomenon of interest. The frequencies that the power is concentrated at appear to be the frequencies of important dynamic mechanisms. Thus the dynamic processes related to these frequencies should be contained in the model.

To test the ability of a model on reproducing observations, the model skill should be tested. As described, if the output of the model correlates strongly with the observations, the model is considered contains the key physical mechanisms operating in the area of interest. Thus the model can be used to study more detailed processes in this ocean area

[McMurtry, 2017]. In our study, the model is used to investigate the roles of wind and barotropic tide in driving mixing in seasonally stratified shelf seas.

In the study in the following chapters (Chapter 4 to Chapter 6), several hypothesis are made which concern the role of wind and tide in producing shear over the thermocline. In the ocean such processes are complicated since in the real ocean, the wind driven processes and the tide interact as so the individual impacts are hard to separate. Application of the model however allows the impacts of the wind and tide to be separated. Furthermore the study of the switching between shear drivers is limited by the spatial and temporal extent of the observed data. The 1D Turbulence Closure Numerical Model study is not constrained by the same limitations and will be used to reproduce the shear over thermocline for varying conditions, including different bathymetry and water column structures and further clarify the mechanism behind the switch of driver of shear over thermocline.

3.2 Introduction to 1D Two-Layer Vertical Dynamical Numerical Model

3.2.1 Assumptions for the model

The 1D Two-Layer Vertical Dynamical Numerical Model (hereafter two-layer model), which were published by Burchard and Rippeth [2009], were able to reproduce the spikes of evolution of observed shear squared in the WIS09 mooring site (detailed information can be found in Chapter 4). The model is based on a simple dynamic equation (see equation 3.30) which the assumptions of the model are as follows:

- The water column is stratified into two mixed layers, the surface mixed layer and the lower mixed layer. The example of water column structure and the thickness of the surface and lower mixed layer, h_s and h_b, are shown in fig 2.1.
- The model does not contain mixing mechanism between surface mixed layer and lower mixed layer which implies that the water column structure is not automatically adjustable, thus the evolution of water column structure is not predictable, furthermore the development of shear based on the evolution of water column structure cannot be represent by the model. In this case, the surface mixed

layer and lower mixed layer have to be defined by the model user. As the water column structure varies in the real ocean, the chosen thickness of each layer should fits the conditions under all the observational period, which means either it is a fixed depth suits the entire period, or the depth of thermocline that defined by users has to coincident with the changing of thermocline.

- The air-sea heat exchange at the sea surface is not included in the model, since the heat exchange at the sea surface will cause the vertical motions, for example the convection, which is not the physical process we are interested and will make the modelled results more difficult to explain.

- In the real ocean, the buoyancy frequency (N^2) varies with the evolution of water column structure, however in the model, the assumption of a stable water column structure results in a temporal stable N^2, which suggests that all the mixing is created only by the variation of shear.

- The surface mixed layer is regarded as a well-mixed slab-layer and the energy into the mixed layer assumed spread to the whole mixed layer instantly, which results a unit of the velocity over surface mixed layer [Simpson and Sharples, 2012].

- The boundary forcing at the sea surface is by wind forcing, and at the sea bed is barotropic tide forcing through friction.

- In the surface and lower mixed layer, the inner frictions (see section 3.2.2) are ignored.

3.2.2 Model equations

The model [Burchard and Rippeth, 2009] is developed based on the 1D momentum equation which is:

$$\frac{\partial u}{\partial t} - \frac{\partial \tau^x}{\partial z} - fv = -g\frac{\partial \eta}{\partial x} \tag{3.1}$$

$$\frac{\partial v}{\partial t} - \frac{\partial \tau^y}{\partial z} + fu = -g\frac{\partial \eta}{\partial y} \tag{3.2}$$

Where u and v are the current velocity components, z is the depth, τ^x and τ^y are the shear stress components normalized by density at E-W and N-S direction respectively, f is the Coriolis coefficient, $\frac{\partial \eta}{\partial x}$ and $\frac{\partial \eta}{\partial y}$ are the surface elevation slopes.

The stresses at surface (τ_s) and bottom (τ_b) are defined as:

$$\tau_s^x = \rho_{air} C_{D10} U_{10} u_{10} \tag{3.3}$$

$$\tau_s^y = \rho_{air} C_{D10} U_{10} v_{10} \tag{3.4}$$

$$\tau_b^x = \tau^x(0) = C_{Db} U_{bt} u_{bt} \tag{3.5}$$

$$\tau_b^y = \tau^y(0) = C_{Db} U_{bt} v_{bt} \tag{3.6}$$

$$U_{bt}^2 = u_{bt}^2 + v_{bt}^2 \tag{3.7}$$

Where C_{Db} is the bottom drag coefficient, ranging from 0.0015-0.0025, U_{bt} is the bottom current speed, u_{bt} and v_{bt} are bottom current speed constituents at E-W and N-S direction.

The interfacial stress is defined as:

$$\tau_i^x = \tau^x(z_i) \tag{3.8}$$

$$\tau_i^y = \tau^y(z_i) \tag{3.9}$$

The internal depth z_i is ranged from$-\mathrm{h} < z_i < 0$, the surface mixed layer thickness is $h_s = -z_i$, while the lower mixed layer thickness is $h_b = h + z_i$.

The surface and lower mixed layer current velocity components are:

$$u_s = \frac{\int_{z_i}^{0} u(z)dz}{h_s} \tag{3.10}$$

$$u_b = \frac{\int_{-h}^{z_i} u(z)dz}{h_b} \tag{3.11}$$

$$v_s = \frac{\int_{z_i}^{0} v(z)dz}{h_s} \tag{3.12}$$

$$v_b = \frac{\int_{-h}^{z_i} v(z)dz}{h_b} \tag{3.13}$$

The depth mean velocity components are:

$$u_m = \frac{\int_{-h}^{0} u(z)dz}{h} \tag{3.14}$$

$$v_m = \frac{\int_{-h}^{0} v(z)dz}{h} \tag{3.15}$$

According to equations 3.10 - 3.15 the relationship of these velocity components is:

$$u_s h_s + u_b h_b = u_m h \tag{3.16}$$

$$v_s h_s + v_b h_b = v_m h \tag{3.17}$$

Substituting equations 3.3 - 3.17 into the momentum equations 3.1 and 3.2, and we get：

$$\frac{\partial u_s}{\partial t} - \frac{\tau_s^x}{h_s} + \frac{\tau_i^x}{h_s} - f v_s = -g\frac{\partial \eta}{\partial x} \tag{3.18}$$

$$\frac{\partial u_b}{\partial t} - \frac{\tau_i^x}{h_b} + \frac{\tau_b^x}{h_b} - f v_b = -g\frac{\partial \eta}{\partial x} \tag{3.19}$$

And

$$\frac{\partial v_s}{\partial t} - \frac{\tau_s^y}{h_s} + \frac{\tau_i^y}{h_s} + f u_s = -g\frac{\partial \eta}{\partial y} \tag{3.20}$$

$$\frac{\partial v_b}{\partial t} - \frac{\tau_i^y}{h_b} + \frac{\tau_b^y}{h_b} + f u_b = -g\frac{\partial \eta}{\partial y} \tag{3.21}$$

The bulk shear vector components are：

$$S_u = \frac{u_s - u_b}{h_{diff}} \tag{3.22}$$

$$S_v = \frac{v_s - v_b}{h_{diff}} \tag{3.23}$$

$$h_{diff} = \frac{h}{2} \tag{3.24}$$

Subtract equation 3.19 from equation 3.18, and subtract equation 3.21 from equation 3.20, then we get：

$$\frac{\partial S_u}{\partial t} - \frac{2\tau_s^x}{h_s h} + \frac{2\tau_i^x}{h_s h_b} - \frac{2\tau_b^x}{h_b h} - f S_v = 0 \tag{3.25}$$

$$\frac{\partial S_v}{\partial t} - \frac{2\tau_s^y}{h_s h} + \frac{2\tau_i^y}{h_s h_b} - \frac{2\tau_b^y}{h_b h} + f S_u = 0 \tag{3.26}$$

The interfacial shear stress can be represented by means of a quadratic friction law, which is:

$$\begin{aligned} \tau_i^x &= C_i u_{diff} U_{diff} \\ &= C_i (u_s - u_b)[(u_s - u_b)^2 + (v_s - v_b)^2]^{1/2} \\ &= \frac{1}{4} h^2 C_i S_u S \end{aligned} \tag{3.27}$$

$$\tau_i^y = \frac{1}{4} h^2 C_i S_v S \tag{3.28}$$

Where the C_i is the interfacial drag coefficient between the surface mixed layer and the lower layer.

The bulk shear squared is calculated from the shear vectors as:

$$S^2 = S_u^2 + S_v^2 \tag{3.29}$$

Multiply $2u_s$ with equation 3.25 and multiply $2v_s$ with equation 3.26 respectively, and add the two terms together, translate the equation from scale form into vector form, then we get the 1D two-layer vertical dynamic numerical model equation, which is:

$$\partial_t S^2 = \frac{4}{h}\vec{S} \cdot \left(\frac{\overrightarrow{\tau_s}}{h_s} + \frac{\overrightarrow{\tau_b}}{h_b}\right) - C_i \frac{h^2}{h_s h_b} S^3$$

$$= P(S^2) - D_i(S^2) \qquad (3.30)$$

Where $\frac{\overrightarrow{\tau_b}}{h_b}$ represents the tide forcing, $\frac{\overrightarrow{\tau_s}}{h_s}$ represents the wind forcing, and the $C_i \frac{h^2}{h_s h_b} S^3$ presents an interfacial friction. $\overrightarrow{\tau_s}$ is the surface shear stress vector, $\overrightarrow{\tau_b}$ is the bottom shear stress vector, $P(S^2)$ is the production of bulk shear squared and $D_i(S^2)$ is the dissipation by interfacial friction.

Equation 3.34 shows that the evolution of bulk shear squared is forced by wind (τ_s) and tide (τ_b) and dissipated by interfacial (C_i) friction.

In the study of western Irish Sea (Chapter 4) and northern North Sea (Chapter 5), the process we are concerned with is the production of bulk shear squared ($P(S^2)$). The dissipation by interfacial friction ($D_i(S^2)$) is neglected. Thus the equation used in the study is simplified to be:

$$\partial_t S^2 \approx \frac{4}{h}\vec{S} \cdot \left(\frac{\overrightarrow{\tau_s}}{h_s} + \frac{\overrightarrow{\tau_b}}{h_b}\right)$$
$$= \frac{4}{h} S[\tau_s cos(\beta_s - \alpha) + \tau_b \cos(\beta_b - \alpha)] \qquad (3.31)$$

Fig 3.1 shows the directions of the shear vector, surface stress vector and bottom stress vector. α is the direction of shear and β is the direction of boundary stresses, with β_s being the direction of surface boundary stress, and β_b the direction of bottom boundary stress, north direction is 0 °and anti-cyclonic rotation is positive. The angle between the shear and boundary stress is $(\beta - \alpha)$. As can be seen from equation 3.31, the evolution of bulk shear squared is not only related to the intensity of shear and the intensity of boundary stresses, but also related to the angle between the shear and the boundary stresses. The maximized shear squared production generated when the shear and boundary stress are alignment ($\alpha = \beta$), which coincident with the previous studies [Burchard and Rippeth, 2009; Brannigan et al., 2013].

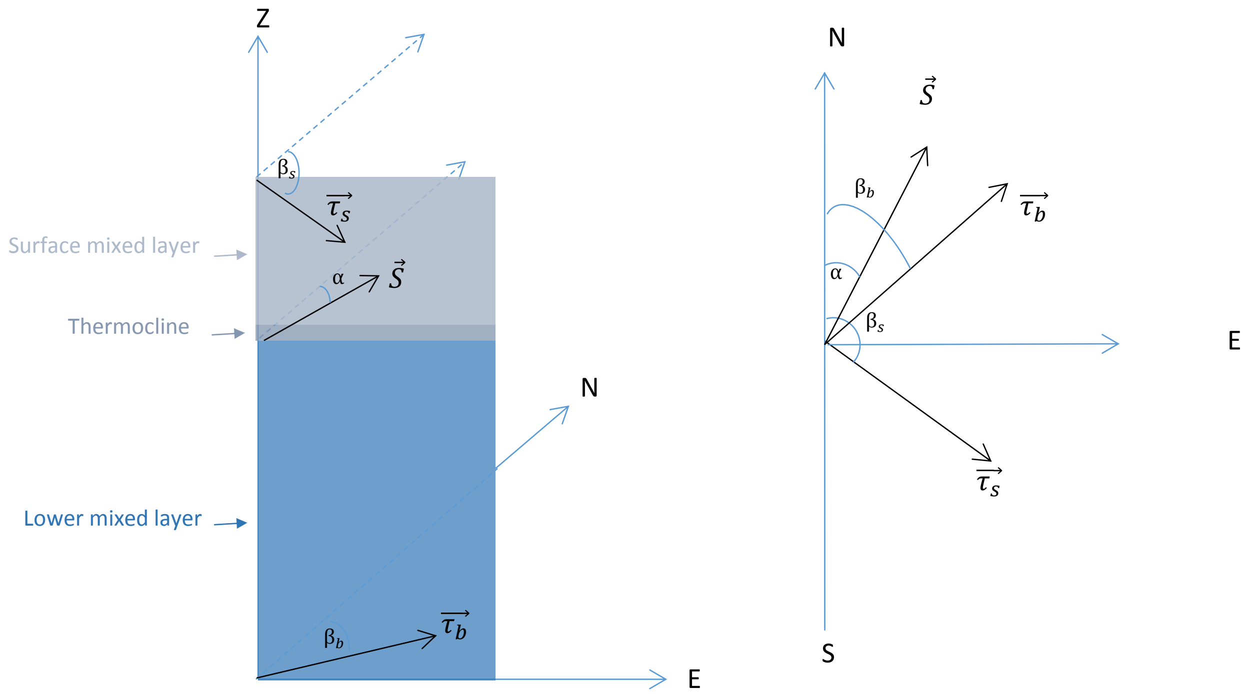

Fig 3.1 An example showing the different directions of shear and boundary stress. The left panel shows the boundary stresses and shear vectors in the water column, $\vec{\tau_s}$ is the surface stress, $\vec{\tau_b}$ is the bottom stress and $\vec{S}$ is the shear. Assuming that the northward direction corresponds to 0°, anti-cyclonic rotation is positive, the direction of surface stress is α, and the direction of boundary stress is β. β_s is the surface stress and β_b is the bottom stress. The right panel shows a bird's-eye view of all these directions. The angle between the shear and boundary stress, $(\beta - \alpha)$, is the parameter of interest to this study.

3.2.3 Data Interpolation

As the wind data and the ADCP data are not length agreement, for the calculation convenience, the interpolation was applied to the wind data to make it agree with data length of shear and boundary stresses during modelling. However, a problem arises with the interpolation of the angle of shear and boundary stresses when the direction angle crosses 0 ° with anti-cyclonic rotation. For example, when the angle turns from 330 ° to 70 °, the real rotation path should be 330 °, 355 °, 20 °, 45 ° and 70 ° (fig 3.2a), however the interpolate of the angle directly will results in a fake rotation path of 70 °, 135 °, 200 °, 265 ° and 330 ° (fig 3.2b). Thus the cos $(\beta - \alpha)$ term should not be estimated directly from the interpolated $(\beta - \alpha)$ due to the interpolation issue.

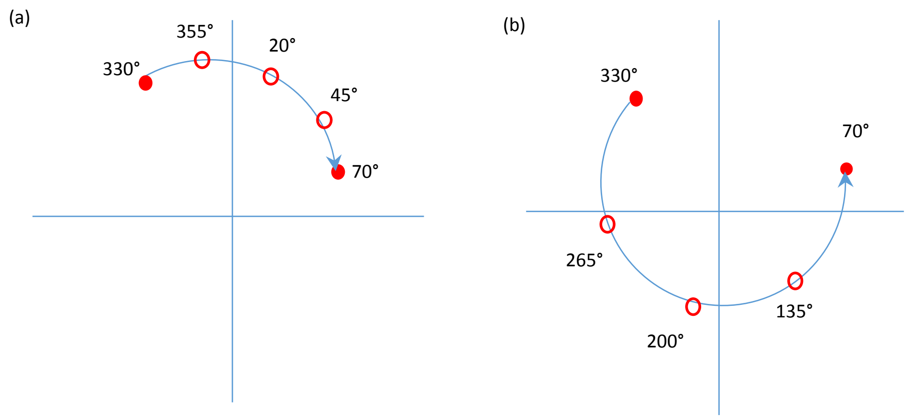

Fig 3.2 An example of the interpolation of the crossing of 0° angle variation (anti-cyclonic). (a) the real rotation path of the angle turns from 330° to 70°, which shows an anti-cyclonic rotation. (b) the fake rotation path from 330° to 70° estimated using a simple interpolation of angle due to the angle rotates crossing 0°. Note it actually shows a cyclonic rotation.

According to the product and sum formulas:

$$cos(\beta - \alpha) = cos\beta cosa + sin\beta sin\alpha \qquad (3.32)$$

To avoid the zero-crossing issue shown in fig 3.2, the interpolation should be applied on the sine or cosine form of shear direction (α) or boundary stress direction (β), for example $sin\,\alpha$, $sin\,\beta$, $cos\,\alpha$ and $cos\,\beta$, instead of interpolate directly on the angle itself $(\beta - \alpha)$.

Fig 3.3 shows an example of the performance for two different interpolation approaches (the green line and black line) with the vector rotating through 0 °, as in fig 3.2a. The y-axis in fig 3.3 does not represent the angle value for each approach but represents the value of the sine (angles). Assuming an anti-cyclonic rotation process occurs in the shelf sea, four data were picked from the angle rotating process as the sampled data. The sine form of the real rotating process is represented as blue solid line, and the sine forms of the four data are shown as the four red dots. Using the four example data as the original data, two interpolation approaches were applied. One way is to apply the interpolation on the four sampled angles, get a series of interpolated angles, and then estimated the sine form of these interpolated angles. This approach is represented in fig 3.3 by the green dotted line. The other way is to estimate the sine form for the four sampled angles first, and then apply the interpolation on the four sine forms, to get a series of interpolated sine form of angles. This, in fig 3.3, is represented by black dotted line.

As shown in fig 3.3, when the angles rotating from 330 ° - 359 ° and 40 ° - 70 °, the two approaches does not have significant difference, and they both coincident with the result from real rotating process. However, when the rotation start to cross 0 °, which is from 359 ° to 40 °, the two approaches shows a great divergence. The black dotted line still coincide with the real rotating process (the blue line), whilst an unexpected sinusoid appears on the green dotted line.

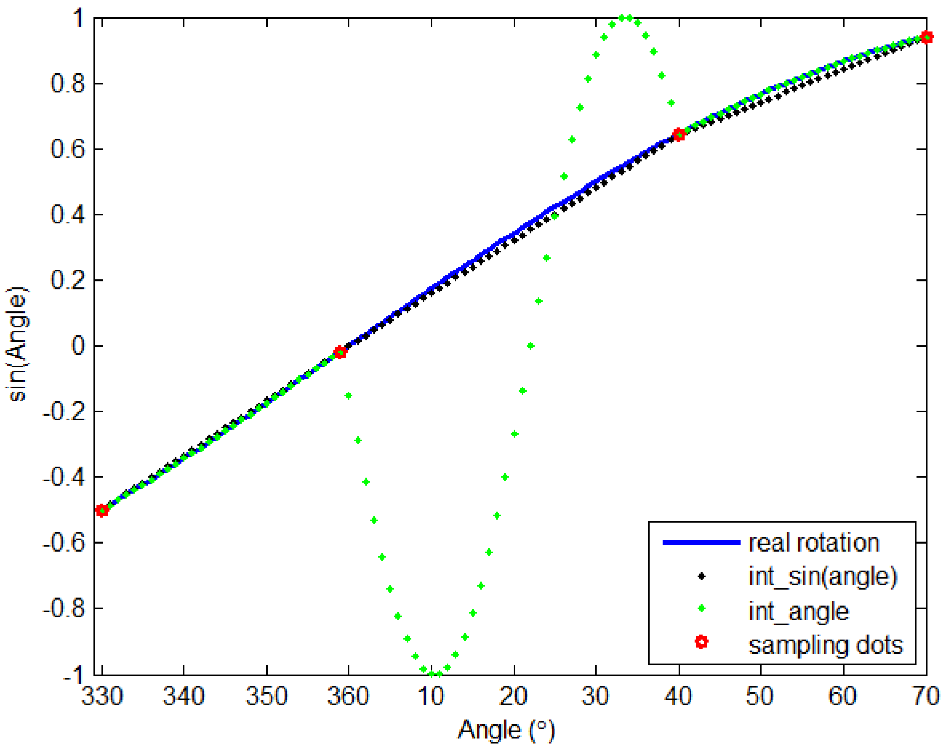

Fig 3.3 Example of the performance of two different approaches to interpolation for a vector rotating cross 0°. The blue solid line represents the sine form of the actual angle rotating process which is from 330° to 70°. The four red dots are the sine form of four sampling data during the angle rotating process which were considered as the sampled data. The blue line and the red dots are the original data not been interpolated. All the interpolations are based on the original four red dots, and the interpolated results are then compared with the blue line. The black dotted line and the green dotted line represents two approaches to interpolate the sampled data (red dots); one way is to interpolate the sine form of the sampled data (the four red dots) which the results shown as black dotted line and the second way is to interpolate the sampled data first and then estimate the sine form (green line). Compare with the sine form of physical process in the real ocean (blue solid line), before and after the sampled data rotate across 0°, which are the regions of 330° to 359° and 40° to 70°, the performance of interpolate applied on the sampled data (green dotted line) is better than interpolate applied on the sine form of sampled data (black dotted line), however in the region that the sampled data are crossing 0°, where is from 359° to 40°, the performance of interpolate applied on the sampled data (green dotted line) have significant divergence with the sine form of real physical process in the ocean (blue solid line) and the interpolate applied on the sine form of sampled data (black dotted line) is coincide with the sine form of real physical process in the ocean (blue solid line).

3.3 Introduction to 1D Turbulence Closure Numerical Model

Due to the lack of knowledge of more detailed physical mechanisms of turbulence, the study of turbulence highly depends on the model based on experimental lab data and observation data. Then the model was introduced in the turbulence study as a powerful tool. Those models with the key hydrodynamic mechanism included, could be used in the study of further detailed information of turbulence process. The model employed in our study is a 1D Vertical Turbulence Closure Numerical Model (hereafter TC model) TC22aDem, which is based on the Mellor-Yamada 2.2a turbulence closure scheme [Mellor and Yamada, 1974; Mellor and Yamada, 1982; Simpsons et al., 1996; Simpson and Sharples, 2012]. The model is forced by the wind and tide. It is an idealistic rather than predictive model, which is used for deepening our understanding of the physical mechanisms in the ocean. It describes the evolution of the whole water column in the response to wind and tide forcing, by enabling the generation of turbulence and simulating the consequent mixing and hence modification of the water column structure.

One potential shortcoming from TC22aDem model is that in the real shelf sea the solar heat would possibly create a new shallower thermocline over the deeper old thermocline when the wind stress is weak [Lincoln, 2012], however due to the lack of solar heating module, this could not be examined using the TC22aDem model.

3.3.1 The closure problem

The closure problem can be the simply consider as the difficulty to find a firm solution for an equation set without the help of additional constant or additional equation. Mathematically, finding a solution for an equation set, which was named as equation set 1, sometimes requires new unknown parameters involved in (and form equation set 2), however in some case no solution can be found to this equation set 2 without additional equations (and then form equation set 3). For example, in some cases, in order to solve a second order moments equation, we have to involve a third order moment, and to solve the third order moments equation, a forth order moments is needed [McMurtry, 2017]. The requirement of endless introducing new parameters and new equations is known as the closure problem.

Closure problem is a stumbling block in the study of turbulence which is still waiting for its perfect solution. A widely accepted way to deal with the closure problem is to offer an empirical estimation, for example a closure equation or an evaluation for the unknown parameters, so that the equation can be closed and so removing the need to introduce further new terms [McMurtry, 2017]. Mellor-Yamada (MY) closure scheme is one of the most widely used closure solutions. More detailed information about MY closure scheme can be found in Mellor and Yamada [1974; 1982].

The TC model is based on the equation of motion in x and y direction, which is [Umlauf and Burchard, 2005; Simpson and Sharples, 2012; Simpson et al., 1996]:

$$\frac{\partial u}{\partial t} = fv - \frac{1}{\rho}\left(\frac{\partial P}{\partial x} + \frac{\partial \tau_x}{\partial z}\right) \tag{3.33}$$

$$\frac{\partial v}{\partial t} = -fu - \frac{1}{\rho}\left(\frac{\partial P}{\partial y} + \frac{\partial \tau_y}{\partial z}\right) \tag{3.34}$$

Where u and v are the current velocity components, z is the distance from sea surface, τ_x and τ_y are the shear stress components at E-W and N-S direction respectively, f is the Coriolis coefficient, $\frac{\partial P}{\partial x}$ and $\frac{\partial P}{\partial y}$ are the horizontal pressure gradients, ρ is the water density and t is the time of evolution.

The shear stress components are [Simpson and Sharples, 2012]:

$$\tau_x = -\rho N_z \frac{\partial u}{\partial z} \tag{3.35}$$

$$\tau_y = -\rho N_z \frac{\partial v}{\partial z} \tag{3.36}$$

Where N_Z is the vertical eddy viscosity.

Water density, ρ, fluctuates as a function of water temperature, T, and water salinity, S. The T and S over time are described by the advection diffusion equation [Simpson et al., 1996; Simpson and Sharples, 2012]:

$$\frac{\partial (T,S)}{\partial t} = \frac{\partial}{\partial z}\left(K_z \frac{\partial (T,S)}{\partial z}\right) \tag{3.37}$$

Eddy diffusivity K_z and eddy viscosity N_z are the unknown parameters. The length scale L and intensity of turbulence velocity q, which ultimately rely on empirical equations in the Mellor Yamada 2.2a turbulence closure scheme, with the following relationship [Simpson et al., 1996; Simpson and Sharples, 2012]:

$$N_z = S_M q L \tag{3.38}$$

$$K_Z = S_H q L \tag{3.39}$$

$$L = \kappa(z+h)\sqrt{\frac{-z}{h}} \tag{3.40}$$

Where S_M, S_H are the stability function, which is a tool to justify the stability state and based on local buoyancy frequency (equations 3.41-3.43). q is the intensity of the turbulence which is the root mean square speed of the turbulent motion, L is the length scale that related to the distance from boundary, and κ is von Karman's constant which is 0.41.

In Mellor Yamada 2.2a turbulence closure scheme, S_M and S_H based on the Galperin quasi-equilibrium function, and are presented as [Galperin et al., 1988; Deleersnijder et al., 2003]:

$$S_M = \frac{0.39 - 3.09 G_H}{1 - 40.80 G_H + 212 G_H^2} \tag{3.41}$$

$$S_H = \frac{0.49}{1 - 34.68 G_H} \tag{3.42}$$

Where G_H is [Deleersnijder et al., 2003]:

$$G_H = -\frac{L^2 N^2}{q^2} \tag{3.43}$$

N^2 is the buoyancy frequency which only affected by the vertical hydro-dynamic process instead of heat since the TC model does not contain solar heat input.

The turbulent kinetic energy E_k is defined as $\frac{q^2}{2}$ [Simpson et al., 1996]. The evolution of turbulent kinetic energy can be estimated by the following equation [Tennekes and Lumley, 1972; Simpson et al., 1996]:

$$\frac{\partial E_k}{\partial t} = \frac{\partial}{\partial z}\left(N_z \frac{\partial E_k}{\partial z}\right) + N_z\left[\left(\frac{\partial u}{\partial z}\right)^2 + \left(\frac{\partial v}{\partial z}\right)^2\right] + K_z\left(\frac{g}{\rho}\frac{\partial \rho}{\partial z}\right) - \frac{q^3}{B_1 l} \tag{3.44}$$

Where the Mellor Yamada constant B_1=15.

The process of the closure model calculation loop is shown in fig 3.4.

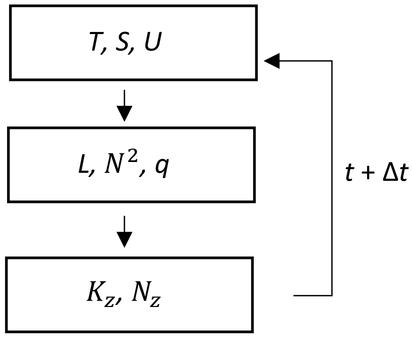

Fig 3.4 A simplified schematic of the TC model calculation flow. The temperature (*T*), salinity (*S*) and water current velocity (*U*) describe the initial water column state. The length scale (*L*), buoyancy frequency (N^2) and intensity of the turbulence (*q*) are estimated from the *T*, *S* and *U*. The vertical viscosity coefficient (N_z) and the vertical eddy diffusivity (K_z) are estimated from the *L*, N^2 and *q*. The temperature (*T*), salinity (*S*) and water current velocity (*U*) at next time step (*t*+Δ*t*) are not from observation but estimated through K_z and N_z.

3.3.2 Precautions: Numerical instability

A common problem with models of stratified flow, including the TC model we employ, is numerical instability. An input over a threshold could cause a considerably error to the output, and this is named numerical instability. In the MY closure scheme, the model instability arise from a positive feedback between shear and eddy viscosity, the increase of shear will decrease eddy viscosity and further again increase shear etc. [Deleersnijder, 1992]. This positive feedback is limited in MY2.2a model by introducing a limitation of $-0.28 \leq G_H \leq 0.0233$ [Galperin et al., 1988], to damp the strong positive feedback from shear on S_M [Deleersnijder et al., 2003]. A more detailed discussion on the limitation of G_H can be found in Deleersnijder [1994].

Due to the numerical instability, the wind speed and tide amplitude should be limited to avoid the appearance of 'output discontinuity'. In the sensitivity test in Chapter 6, the wind speed should no bigger than the original data and the model run hours should be no longer than 20 days. Meanwhile, another interesting limitation is the first data of wind speed should smaller than a threshold, for example 6.8 ms^{-1}, which the reason has not been figured out. The limitation of the first data of wind speed varies with the intensity of tide force.

3.4 Difference between TC model and two-layer model

The key difference between the two models is the TC model contains the physical mechanism of mixing between the surface mixed layer and the lower mixed layer while the two-layer model does not.

The TC model could identify the process causing a switch from flow to shear instability and mixing, while the two-layer model can only estimate shear. The water column structure in TC model evolves with time while the default setting in two-layer model is that the water column structure is always constant. Thus the TC model can be used to describe the evolution of water column structure response to wind and tide forcing through the whole water column due to the energy flux caused by the diapycnal motion. While the response of wind and tide in two-layer model is mainly concentrated on two layers separately due to the lack of the diapycnal transport.

Chapter 4

Shear generation during development of seasonal stratification

In this chapter, we present and analyse data collected in the seasonally stratified zone of the western Irish Sea (hereafter WIS) during spring and early summer of 2009. The study aims at identifying the dominant driver for the bulk shear, by studying diapycnal mixing within the thermocline in the WIS09 mooring site. A two-layer model is used alongside the observations to aid interpretation of the observations and identification of the processes responsible for enhanced shear across the thermocline.

4.1 Data collection

Our study is based on a wind-driven nutrient pump research project in 2009. Data, obtained from moorings and from the ship, were collected between two cruises of the RV Prince Madog PD20/09 and RV Prince Madog PD27/09 on 19th May 2009 (day 138) and 7th July 2009 (day 189). During the first cruise, the ADCPs and thermistor moorings (with a met station on buoy) were deployed in the seasonally stratified water (figs 4.1 and 4.2) at 53°47 N, 5°38 W (the WIS09 mooring site). These moorings were then recovered during the second cruise. The maximum water depth at the mooring location was 95 m.

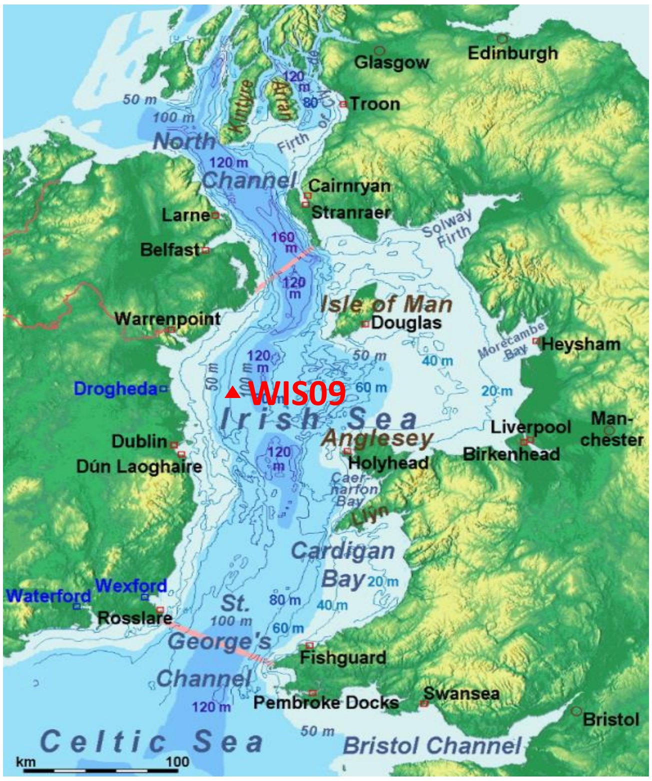

Fig 4.1 Bathymetry map of Irish Sea (Ulamm, 2014) and the location of WIS09 mooring site (red triangle)

The surface and bottom time series of temperature and salinity were measured using two mooring MicroCAT CTDs (fig 4.2), and which were located close to the surface on the mooring buoy, and close to the sea bed on the mooring anchor respectively, linked with the deployed thermistor moorings. In the upper 45 m of the water column, 20 Star-ODI thermistors were attached to the mooring string at an interval of 2.5 m, to collect temperature data across the surface mixed layer, the thermocline, and part of the lower mixed layer. The met station, which is attached to the surface buoy, failed to work during the mooring period. Thus, in this chapter, the meteorology data (wind speed and direction) were obtained from the British Meteorological office reanalysis model, with a resolution of 3 hours. The location of modelled wind data has been taken from the WIS09 mooring site.

The single CTD profile data and water samples at the WIS09 mooring site were collected during both cruises, where the temperature and salinity profiles could be used to estimate the density structure of the water column in each cruise respectively.

Two ADCPs were deployed on the mooring: a 300 kHz ADCP on a sea bed mount which covered the whole water column, and a 600 kHz RDI Workhorse broadband ADCP on sub-surface floatation (fig 4.2), positioned in the middle of the water column at -45 m. These instruments were employed to collect high resolution velocity profiles across the upper half of the water column. However, the 300 kHz ADCP failed and did not collect any data during this mooring period. Thus, the current data used in this study is that from the 600 kHz ADCP which covered the upper half of the water column.

In this chapter, we will examine the time series of the temperature profile and current velocity profile, the single temperature and salinity profiles from the ship cruises, and the time series of wind velocity from the British Meteorological office reanalysis model.

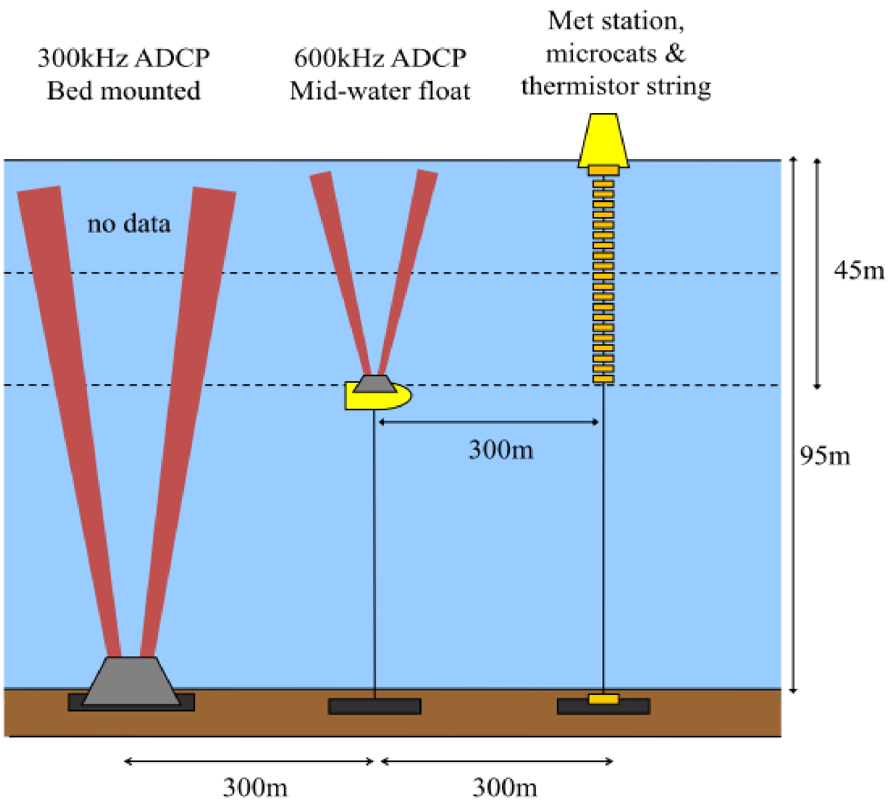

Fig 4.2 Graph of several instruments deployed at the mooring site at an interval of 300 m [Lincoln, 2012]. The 300 kHz RDI Workhorse bed ADCP is mounted on the left and aims to measure the whole water column. However, it failed to collect data during the mooring period due to a software fault. A 600 kHz mid-water floated ADCP in the middle, which is located at -45 m, the data profile covers the upper 45 m of the water column. The mooring site located on the right side includes a met station (yellow trapezoidal), two Microcat CTDs (big orange rectangles below the met station and at the bottom) and the string with 20 Star-ODI thermistors (20 smaller orange rectangles in the middle). The met station failed to collect data in the mooring period. The two Microcat CTDs located at the mooring buoy and the mooring anchor were included to measure a more accurate surface and bottom temperature and salinity. The 20 Star-ODI thermistors cover the whole upper 45 m of the water column in 2.5 m intervals.

4.2 Stratification of WIS09 mooring site

4.2.1 Two factors that affect stratification: temperature and salinity

I. Evolution of temperature and salinity structure

CTD profiles at the first and second cruise show the change in temperature, salinity, and hence density structure over the period of the two cruises. On 19th May (day 138), the beginning of the 2009 research cruise, the sea temperature in the surface mixed layer was 10 ℃ and about 9 ℃ in the lower mixed layer at WIS09 mooring site, while during the second cruise, on 7th July (day 189), those were 15 ℃ and 10.5 ℃, respectively (fig 4.3). The temperature changes indicate an increase of 5 ℃ in the surface mixed layer, which is higher than the 1.5 ℃ warming in the lower mixed layer. The difference between surface temperature and bottom temperature rises from 1 ℃ to 4.5 ℃ during this period. The salinity from surface to bottom at mooring site WIS09 is fairly constant throughout the duration of the data collection. On 19th May (day 138), the salinity in the surface mixed layer is near 33.91 ‰ and about 34.20 ‰ in the lower mixed layer while on 7th July (day 189), they are 33.89 ‰ and 34.21 ‰, respectively (fig 4.3).

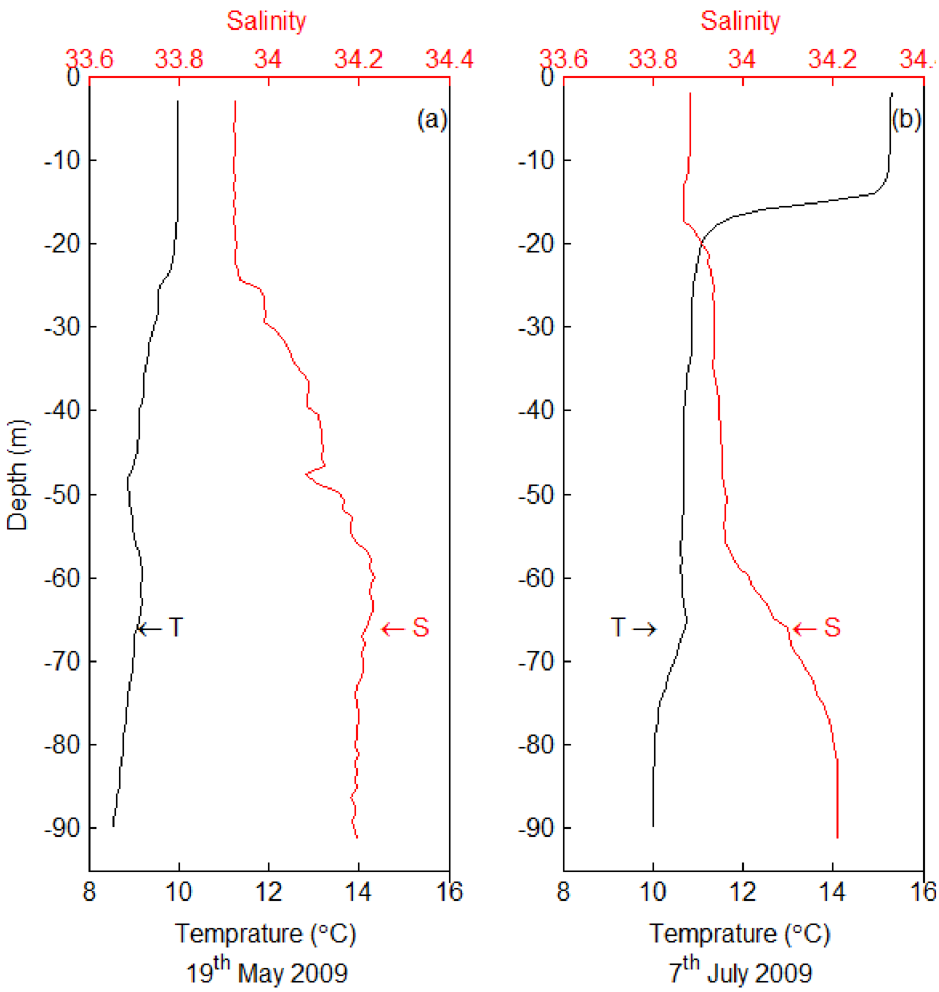

Fig 4.3 The temperature (black line) and salinity (red line) profiles at WIS09 mooring site on 19th May 2009 and 7th July 2009 respectively. In the upper 15 m of the water column, the temperature evolves from 10℃ (a) to 15.2℃ (b), while the lower part (-90 m to -20 m) shows a temperature increase from 9℃ (a) to 11℃ (b). The temperature structure starts to form in May (a) and is well established in July (b). The salinity profile from May (a) to July (b) hardly varies over the entire water column.

II. Evolution of water stratification

In the stratified WIS, the water column is divided into surface mixed layer and lower mixed layer by the thermocline. The thermocline is a thin horizontal layer where the greatest vertical density gradient occurs in the water column. It prevents mixing between surface and bottom waters and therefore acts to maintain the difference in water temperature, nutrient concentration and particulate matter.

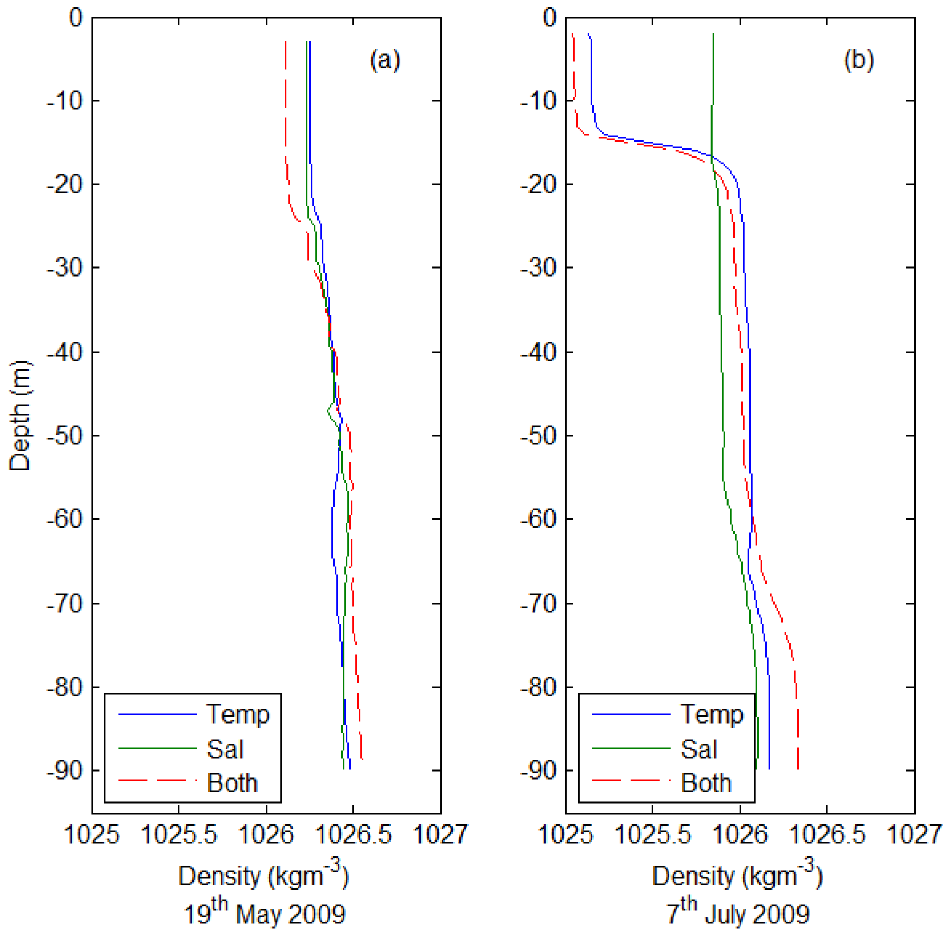

Fig 4.4 The contribution of temperature and salinity to the density profile at WIS09 mooring site on a) 19th May 2009 and b) 7th July 2009. The blue and green line indicate the impact of temperature and salinity on the density profile, respectively, and the red line contains contributions from both temperature and salinity, which is called combined contributed density profile. The similarity of these three profiles in panel a does not affect the study of shear in the stratified water column since the water column is not well stratified in May. But in panel b, the pattern of combined contributed density profile (red) is much more affected by temperature (blue) than by salinity (green). This observation suggests that in this area, the variation in density profile is dominated by changes in temperature rather than changes in salinity.

The three density profiles of temperature, salinity and the combination of both factors are calculated by using the seawater state equation which was accomplished by the Matlab routine sw_dens0.m. On 19th May (day 138) when the CTDs from the ship were deployed, stratification of the water column was weak in WIS; this is reflected by the nearly linear shape of the density profile (fig 4.4a) from the sea surface (1026.1 kgm^{-3}) to the bottom (1026.5 kgm^{-3}). In fig 4.4a the vertical pattern of the salinity contributed density profile, the temperature contributed density profile and the combined contributed density profile are similar. The density differences from surface to bottom are smaller than 0.5 kgm^{-3}, and no single parameter dominated the density profile (fig 4.4a).

During the second cruise on 7th July (day 189), the water column shows a clear two-layer structure with a 3 m thick thermocline (fig 4.4b); the density difference of the surface and lower mixed layer increases from less than 0.5 kgm^{-3} (day 138) to 1.4 kgm^{-3} (day 189). In fig 4.4b, the vertical profile of salinity impact on density does not vary much compared to that in fig 4.4a. But both the temperature contributed and the combined contributed densities decrease from about 1026.2 kgm^{-3} to around 1025.1 kgm^{-3} and the combined contributed density profile varies along with the temperature contributed density profile. The density profile could thus be represented by the temperature profile, and the water column displays stratification.

Fig 4.5 shows the time evolution of the WIS09 mooring site temperature profile: during the period of our interest, the thermocline lies 20 m - 30 m below the sea surface at the WIS09 mooring site. The entire water column was slowly heated up during the mooring period: the upper 25 m (-25 m to 0 m) increased in temperature by about 5 ℃ and the -45 m to -35 m increased about 1℃, which agrees with the ship based measurements depicted in fig 4.4. On days 155, 164 and after day 177, some periods of increased surface mixed layer temperature occur during the entire measuring period, deepening of the surface mixed layer occurs.

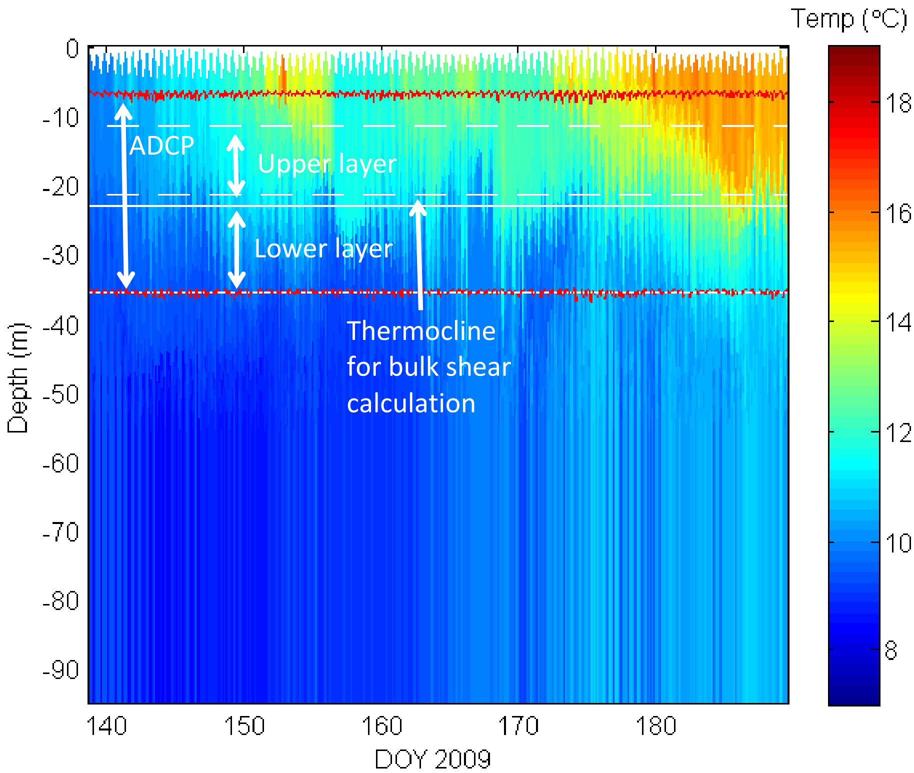

Fig 4.5 The time series of the water column temperature profile at the WIS09 mooring site. The thermocline deepens from May (about -15 m) to July (about -35 m). Around days 153, 167 and 175 - 188, there are three warm water events at the sea surface, the strongest event is on day 153 and the longest event is from days 175 to 188. The warm water at the surface starts to deepen from day 175 and goes down to 25 m beneath sea surface on day 185, which creates a 'second' thermocline (-25 m) above the original thermocline (-35 m). In the lower mixed layer, temperature increases over time as well from around 9 ℃ to about 12 ℃. The zone between the red lines shows where the ADCP data is valid as the ADCP covers the upper 45 m. The data below -55 m is assumed the same as the water temperature at around -45 m; the zone between the white dashed lines is defined to be the surface mixed layer; the zone between the white solid lines is defined as the lower mixed layer; and the zone between the dashed line and the solid line is defined as the thermocline for bulk shear.

A water column with a strong thermocline is defined as a well-stratified water column, and the stratification can be quantified by the potential energy anomaly Φ [Simpson, 1981; Simpson and Sharples, 2012], which is:

$$\Phi = \frac{1}{h}\int_{-h}^{0}\left(\rho_m - \rho(z)\right)gzdz \tag{4.1}$$

$$\rho_m = \int_{-h}^{0}\rho(z)dz \tag{4.2}$$

Where $\rho(z)$ is the water density at depth z, sea surface depth is 0 m and bottom is -h m, ρ_m is the depth mean density. Detailed information on Φ can be found in Chapter 1.

Since the thermocline depth varies during the mooring deployment as shown in fig 4.5, in order to estimate the bulk shear, we define the surface mixed layer as extending from -22 m to -12 m and the lower mixed layer from -35 m to -24 m (fig 4.5).

4.2.2 The wind and tide over the period of the mooring deployment

Time series of the wind at the mooring location over the period of the mooring deployment are shown in fig 4.6. During this period the wind speed is mostly between 5 ms^{-1} and 10 ms^{-1}, occasionally rising to 15 ms^{-1} (for example on days 157 and 168). There is no significant storm event (i.e. wind speeds exceeding 24.5ms^{-1} as defined by the Beaufort scale) during the study period.

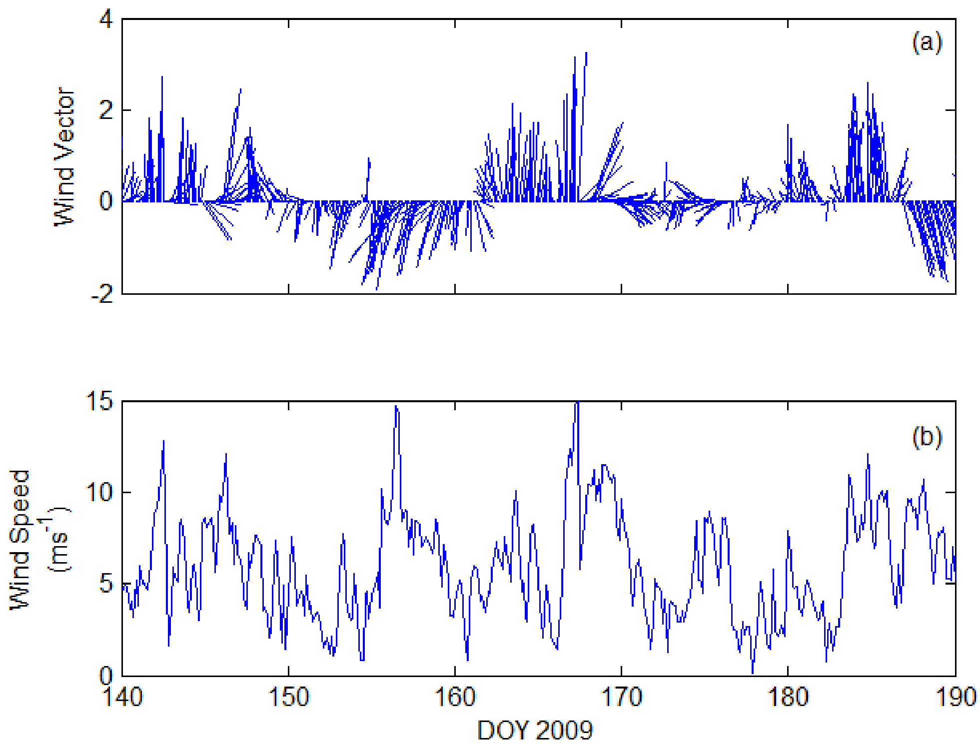

Fig 4.6 a) Wind velocity including wind speed and direction. Due to the mooring MET station at WIS09 mooring site failing to work, the meteorological data is replaced with data from the British Meteorological office reanalysis model. The time resolution of the wind data is 3 hours. Since the model creates a wind field, the location of the wind time series in panel a is extracted to fit the location of the mooring. b) wind speed. Most of the time, the wind speed is between 5 ms^{-1} - 10 ms^{-1}: it exceeds 10 ms^{-1} during 5 periods, namely days 142, 147, 157, 166 - 170 and 183 - 188. On days 157 and 166 - 170, the wind velocities reach up to 15 ms^{-1}. During the mooring period, no significant storm events (wind speed exceeding 24.5 ms^{-1}) occurred.

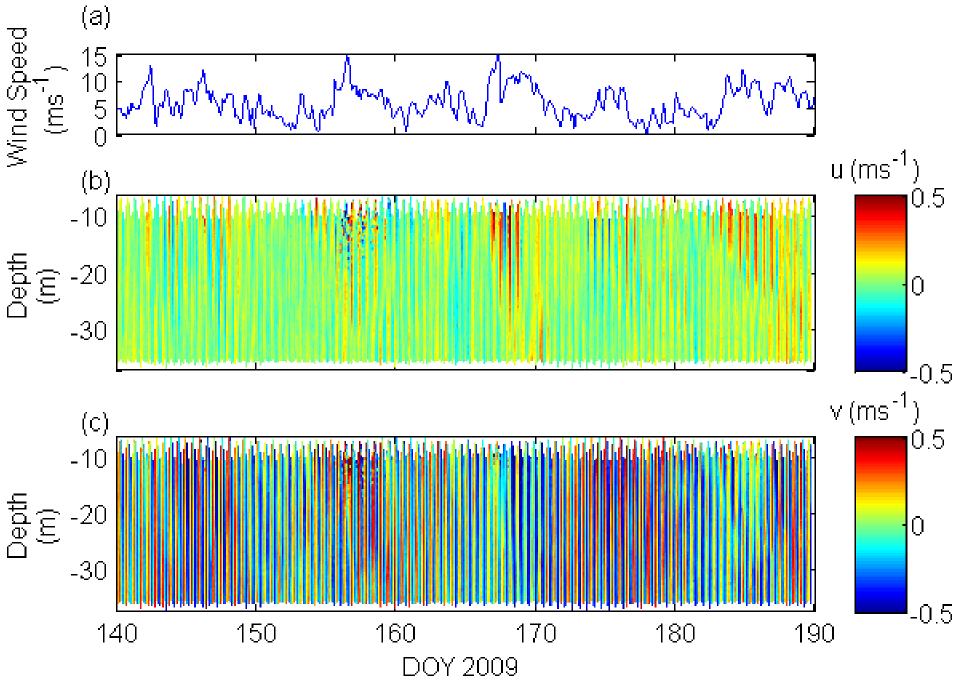

Fig 4.7 a) The time series of wind speed. b) observed current velocity profile at E-W direction. c) as panel b, but at N-S directions. In panel b, three significant periods of enhanced current velocity are evident around days 156 - 158, 166 - 169 and 184 - 187. And the maximum depth of current velocity weakening is 30 m below sea surface. Compared to the current velocity strengthening date in panel b, the current velocity weakening date in panel c and the wind peaks in panel a, it is clear that all the three events occur coincidently.

Fig 4.7 shows the wind speed, current velocity profiles of v at N-S direction and u at E-W direction. Comparing panels b and c we could find, that the intensity and variation of the v component of current velocity variation (velocity in most periods is from -0.5 ms^{-1} to 0.5 ms^{-1}) is stronger than the u component (velocity in most periods is from -0.2 ms^{-1} to 0.2 ms^{-1}) in the whole water column.

Comparison of panels a and b in fig 4.7 shows a strong correlation between enhanced currents in the surface mixed layer and high wind speed events. The wind peak is coincident with current velocity peak at surface, which is obvious especially on days 155 - 160, 165 - 170 and 183 - 188. This suggests that the increase of surface mixed layer current velocity u in E-W direction is coincident with the increase of wind speed. The wind effect reaches down to 30 m below sea surface but is not evident below that.

In fig 4.7, panels b and c, we could find that the currents flow direction switch 180° at semi-diurnal frequency throughout the water column, and the enhanced currents are observed at depths of up to 30 m below the surface when the enhanced wind speed events occurs (for example on days 157 and 168 in panel b). But most of the time the wind does not appear to propagate more than 20 m below sea surface (for example on days 145 and 185).

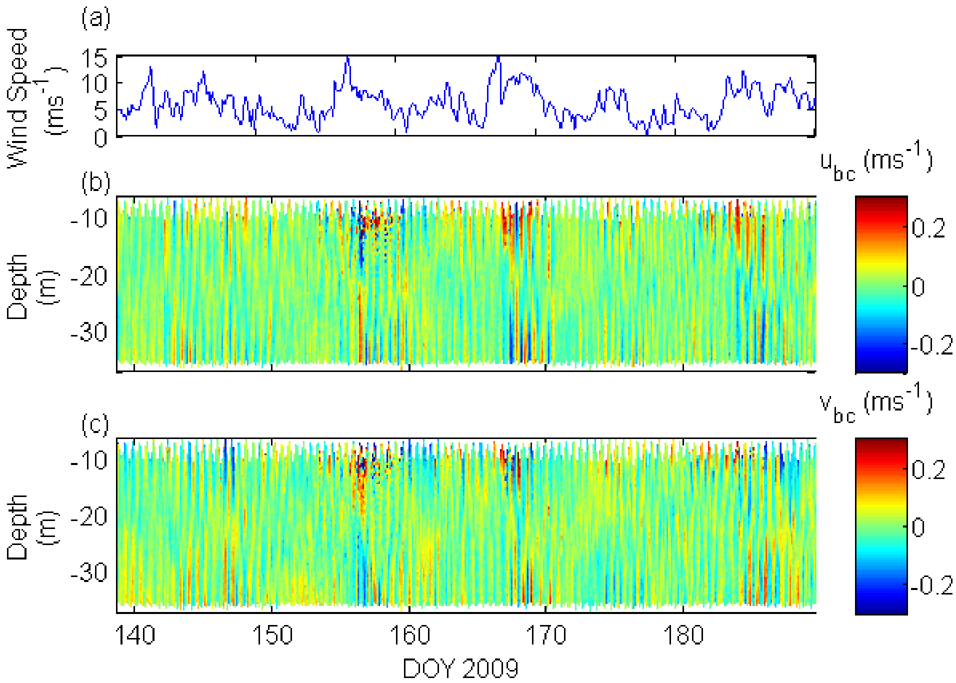

Fig 4.8 a) The time series of wind speed (see fig 4.6). b) the evolution of baroclinic current profile (subtracting the depth mean flow from the raw current velocity data) at E-W direction and c) as panel b, but at N-S direction. The intensity of the current velocity in the upper part (-25 m to -5 m) of the ADCP covered zone (the zone of -35 m to -5 m where ADCP data is valid, shown in fig 4.5) is related to the current velocity in the lower part (-35 m to -25 m) of the ADCP covered zone. The ADCP data below -35 m and above -5 m are unreliable. The baroclinic current strengthens at three periods, days 157 - 158, 168 - 169 and 184 - 186, which is coincident with the enhanced wind periods in panel a. The baroclinic strengthening appears at both the surface and the lower parts at the same time but with a 180° phase lag (more detailed current structure shown in fig 4.9). The magnitudes of the baroclinic current in both directions show no significant difference: the baroclinic current velocity in the N-S direction is slightly smaller than that in the E-W direction. A 180° flow direction switch over the whole water column occurs twice daily, more detailed information can be found in fig 4.9.

The baroclinic current, which is estimated from the depth average current velocity subtracted from the raw current velocity data, is shown in fig 4.8 (panels b and c, for E-W and N-S direction components). The estimated baroclinic current was taken from the ADCP artefact and that artefact was caused by the undersampling of the water column (the ADCP data below -35 m and beyond -5 m are unreliable). Since the ADCP only covers the vertical region of the water column, from -50 m to 0 m, the depth average of the current velocity in our calculations does not represent the depth mean velocity for the whole water column at the mooring site. The vertical region from -35 m to -5 m, where ADCP data is valid, has been clearly separated into two parts by the baroclinic current: The -25 m to -5 m region is the upper part and the -35 m to -25 m region is the lower part.

Based on the observations in fig 4.7, the wind appears not to be able to transfer momentum to the lower mixed layer. However, the baroclinic current shows that the upper part baroclinic current velocity variance is coincident with the variance of baroclinic current velocity of the lower part (fig 4.8), which is obvious especially on days 155 - 160, 165 - 170 and 183 - 188.

As can be found in both panel b and panel c (fig 4.8), there are several enhanced baroclinic current velocity events during the mooring period. These enhanced baroclinic current velocities coincide with the enhanced wind velocities in panel a. The intensities of the E-W and N-S direction components of baroclinic current velocities have no significant difference; neither do the intensities of the upper and lower part of the baroclinic currents. In order to obtain more detailed information of the baroclinic current velocity structure, a two days period (days 158 - 160) baroclinic current profile is shown in fig 4.9.

In the upper part of the ADCP covered zone, the direction of the current switches by 180° with an approximate frequency of twice per day. The intensities of baroclinic current velocity in the lower parts are comparable with those in the related upper parts, but with a significant 180° phase lag.

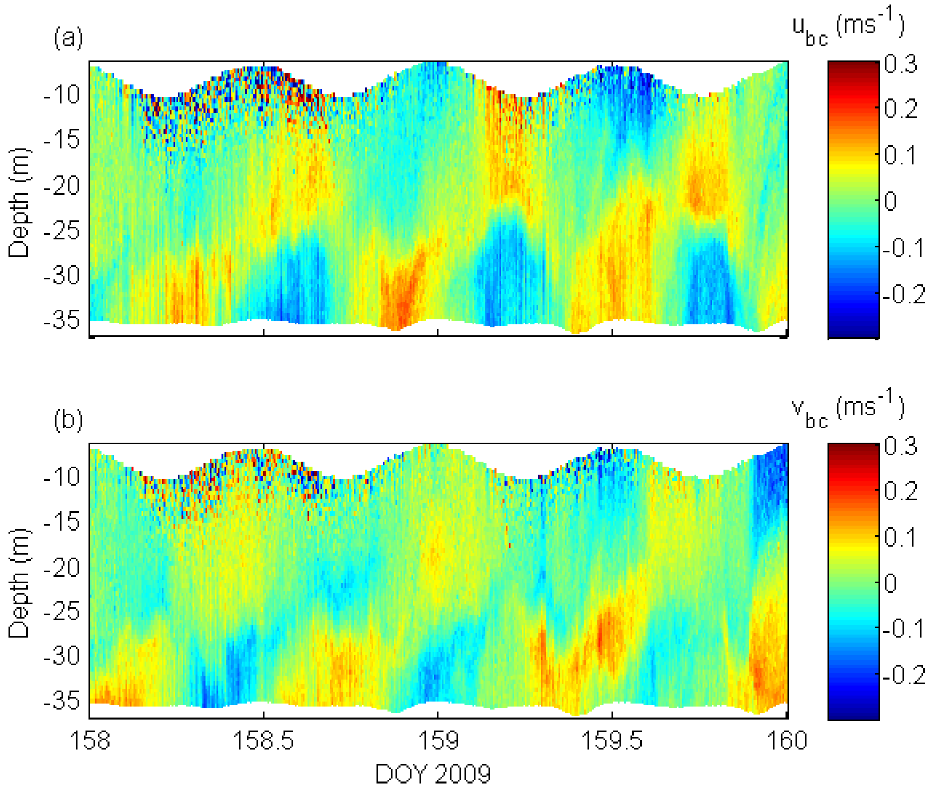

Fig 4.9 A 180° phase lag between the surface and the lower parts of the ADCP covered zone in baroclinic current of E-W (a) and N-S (b) directions. To better illustrate the baroclinic current, a 2 days (days 158 - 160) velocity structure was picked out from fig 4.8. Water current velocity components in both directions clearly show the phase lags between the surface and the lower parts of the ADCP covered zone. Also, in both panels the current components directions switch by 180° nearly twice a day.

The baroclinic current directions can be estimated, according to both panels, by combining the E-W direction and N-S direction current velocity at the same time and same depth. Baroclinic currents at two heights are chosen as examples to represent the movement of baroclinic currents in the surface and lower mixed layer. The 'surface mixed layer example height' is -12.1 m, the 'bottom mixed layer example height' is -34.6 m. Figs 4.10 - 4.11 are the progressive vector plot on days 164 - 170. The baroclinic current of both the surface mixed layer and the lower mixed layer rotate anti-cyclonically.

The rotary spectral analysis was applied on the baroclinic current velocity for both surface and lower mixed layer as shown in figs 4.12 and 4.13. At the lower mixed layer, the dominant frequency is the inertial frequency. However at the surface mixed layer, there is no dominated frequency. This suggests that the baroclinic current at the WIS09 mooring site is related to wind near the sea bottom and is affected by some other phenomenon at the sea surface.

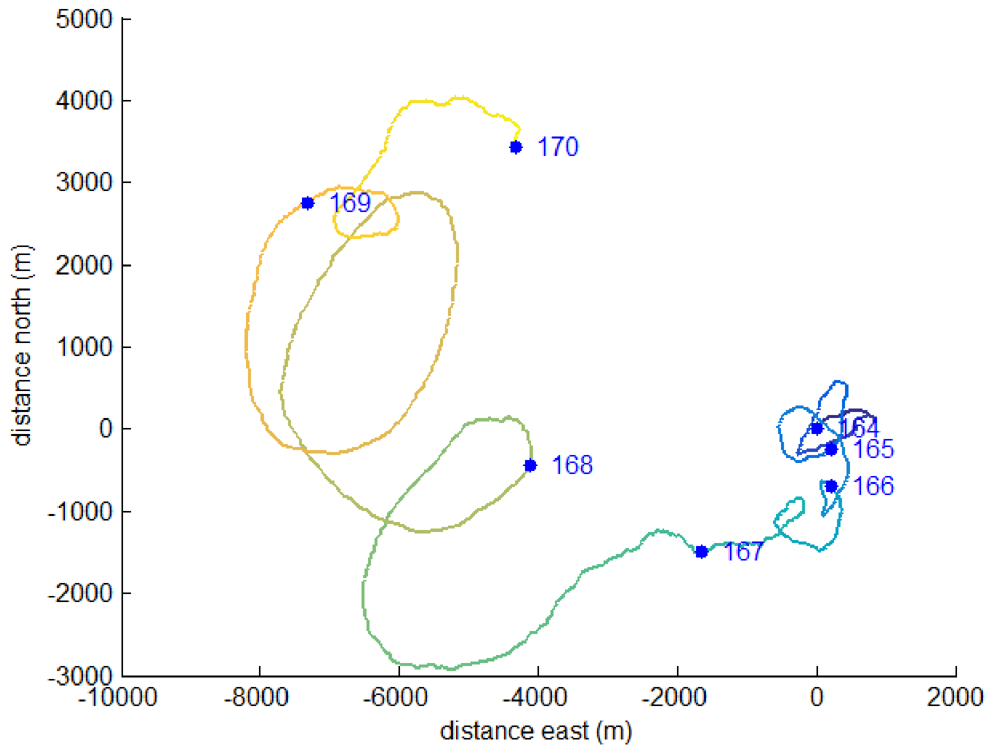

Fig 4.10 The baroclinic current directions can be estimated by combining the E-W direction and N-S direction current velocity at the same time and same depth. The lower mixed layer (data shown for -34.6 m) baroclinic current velocity progressive vector plot showing the baroclinic current rotating anti-cyclonically on days 164 - 170. The lower mixed layer water flows northwest ward with an anti-cyclonic rotation; the gradient color shows the trace of the water parcel movement (The movement starts from the purple color which is day 164 and ends on day 170, in yellow).

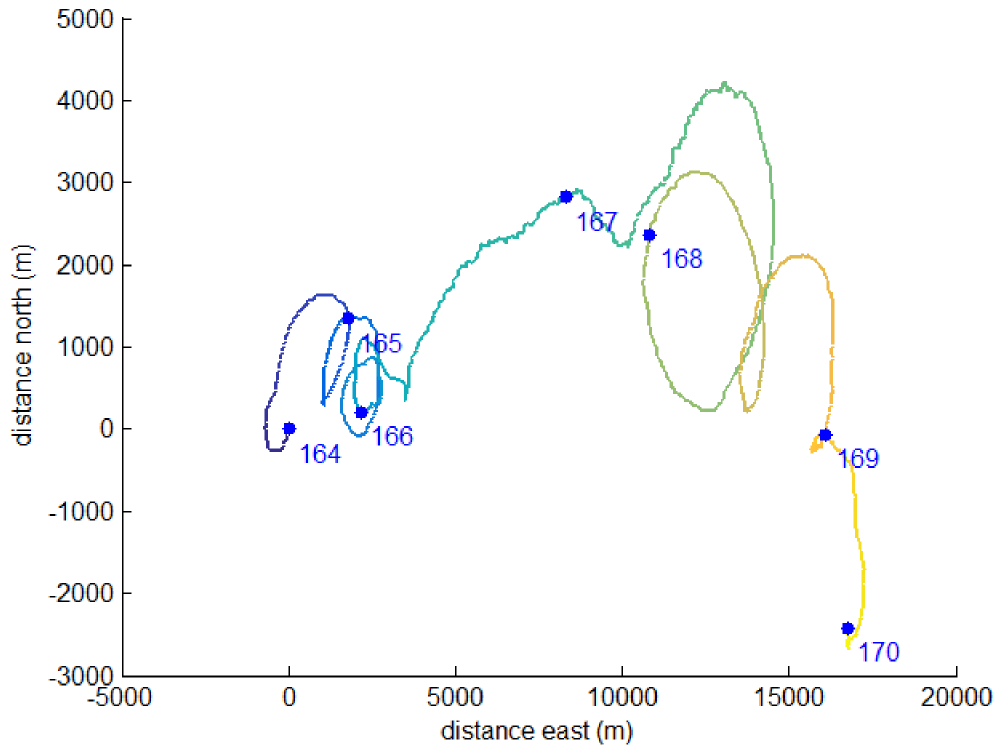

Fig 4.11 Surface mixed layer (data shown for -12.1 m) progressive vector plot showing the baroclinic current motion of weak anti-cyclonic rotation on days 164 - 170. The surface mixed layer current flows Southeast ward with an anti-cyclonically rotation. The gradient color shows

the trace of the water parcel movement (The movement starts from the purple color which is day 164 and ends at day 170, in yellow).

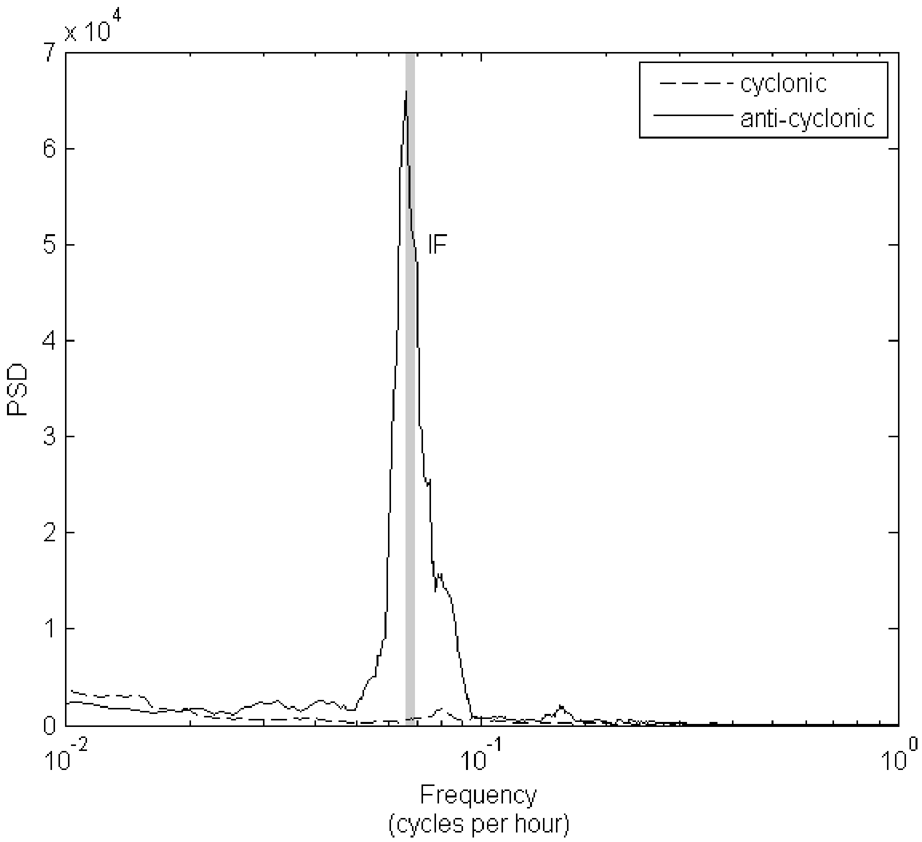

Fig 4.12 Rotary spectral analysis of the baroclinic current of lower mixed layer. The solid line is the anti-cyclonic constituent and the dashed line is the cyclonic constituent. The grey bar indicates the position of local inertial frequency (IF, 0.0674 cycles per hour at the WIS09 mooring site). The anti-cyclonic rotation is the dominant rotation compare with the cyclonic rotation, the dominant frequency concentrated at the inertial frequency.

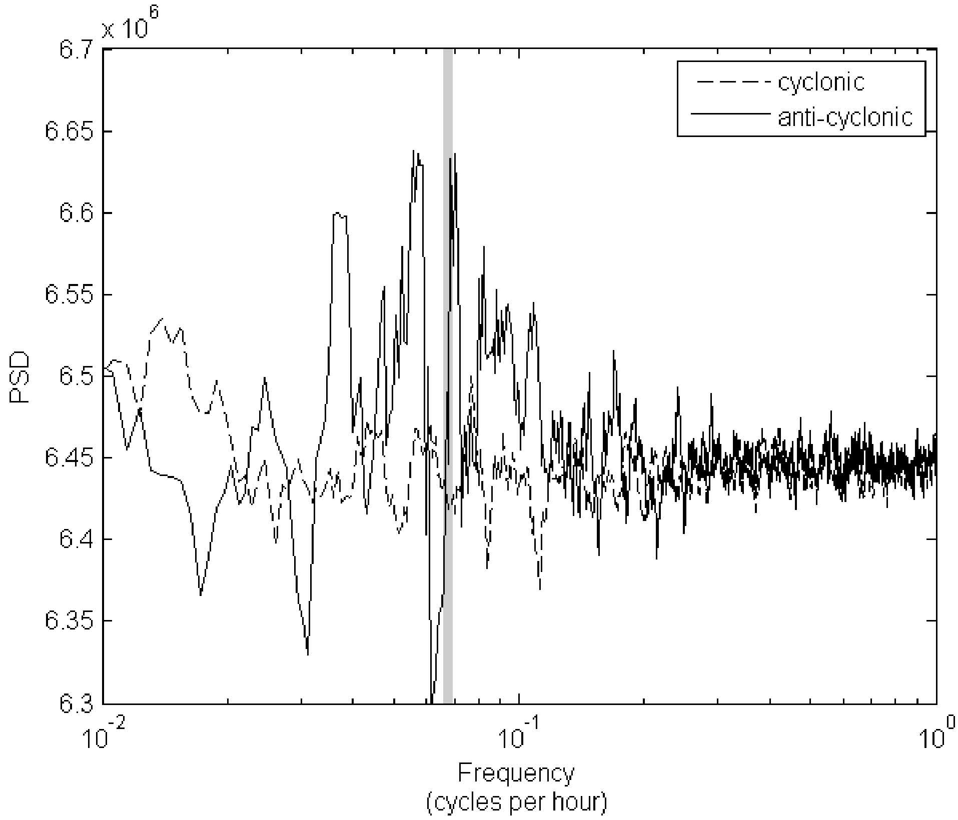

Fig 4.13 Rotary spectral analysis of the baroclinic current of surface mixed layer. The solid line is the anti-cyclonic constituent and the dashed line is the cyclonic constituent. The grey bar indicates the position of local inertial frequency (IF, 0.0674 cycles per hour at the WIS09 mooring site). The anti-cyclonic rotation is the dominant rotation compare with the cyclonic rotation, there is no dominant frequency in this motion.

Barotropic current velocity is defined as the depth averaged flow. Harmonic analysis (or tidal fitting, accomplished by Matlab routine t_tide.m [Pawlowicz et al., 2001]) applied on the barotropic current velocity provides the barotropic tidal current (blue lines in fig 4.14 a and b). Figs 4.14a and b show the comparison between the barotropic currents and barotropic tides in E-W and N-S direction, respectively. In fig 4.14a, the E-W barotropic current has a greater velocity (0.1 ms^{-1} to 0.4 ms^{-1}) than the E-W barotropic tide, which is about 0.1 ms^{-1}. Especially on days 155 - 160 and 165 - 170, the barotropic current time series has two sets of peak bursts with a velocity of 0.4 ms^{-1}, which is 3 to 4 times faster than the concomitant E-W barotropic tidal current. This is evidence of that the E-W barotropic current at the WIS09 mooring site is not significantly driven by the barotropic tide. Comparing fig 4.14a and c, it shows that the two peak burst periods in panel a are coincident with the bursts of wind in panel c. We could hardly find the same conclusion when comparing fig 4.14b and c in the two periods of days 155 - 160 and 165 - 170. Thus the wind effect on the E-W component of the barotropic current (red line in panel a) will be more apparent than that on the N-S component of the barotropic current (red line in panel b).

In fig 4.14b, the N-S component of the barotropic current is similar to the N-S component of the barotropic tide, with the same magnitude of 0.3 ms^{-1}, and coincident with the spring and neap tidal signal during most mooring periods, except on days 168 - 171. This similarity clearly suggests that there is a strong driving relationship between the barotropic current and barotropic tide in the N-S direction.

In fig 4.14a and b, it can be seen that for both the N-S and E-W directions, period of spring-neap cycle is 15 days, the spring tide velocity of the E-W direction is 0.07 ms^{-1}, and that of the neap tide is 0.04 ms^{-1}. For the N-S direction, the spring tide velocity is 0.4 ms^{-1} and that of neap tide is 0.25 ms^{-1}. The N-S barotropic tide is stronger than the E-W barotropic tide.

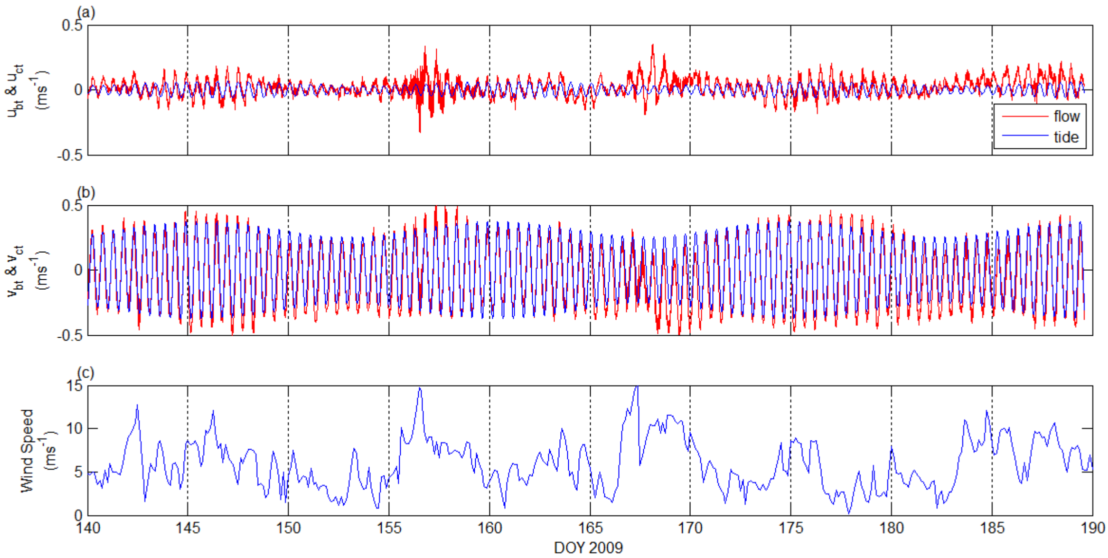

Fig 4.14 The barotropic current velocity (the depth averaged flow), the barotropic tide (tidal fitting of barotropic current) and wind speed. a) The E-W barotropic current velocity u_{bt} (red line) and the E-W barotropic tide u_{tc} (blue line). The E-W barotropic current, which ranges from 0.1 to 0.4 ms^{-1}, has a greater velocity than the E-W barotropic tide, which is about 0.1 ms^{-1}. The spring-neap tide cycle is 15 days. The spring tides occur on days 147, 162 and 177 and the neap tides occur on days 153, 168 and 183. There are three significant velocity divergences during the entire mooring period in which the barotropic current is significantly greater than the barotropic tide, by a factor of 2 - 4. These divergences happen on days 156 - 157, 167 - 170 and 188 – 190. b) the N-S barotropic current velocity v_{bt} (red line) and the N-S barotropic tide v_{tc} (blue line). The N-S barotropic current velocity is slightly higher but still comparable with the N-S barotropic tide most of the time, the magnitude of the barotropic tide is about 0.4 ms^{-1}. c) wind speed (see fig 4.6).

A brief summary of what all the observations reveal:

1. The variation of the water column structure (density profile) at WIS09 mooring site is dominated by the variation of the temperature determined density profile rather than the one that is salinity determined.

2. The water column structure evolves during the mooring period from weakly structured to well-structured and the thermocline deepens over this period. The temperature of the whole water column slowly increased during the mooring period and the temperature variation of the surface mixed layer (5 ℃) is much larger than that of the lower mixed layer (1 ℃). On days 180 - 190, a new and shallow thermocline appears above the old and deep thermocline.

3. During the mooring period, the wind has five peak burst periods on days 142, 147, 157, 166 - 170 and 183 - 188. The increase in wind speed is correlated to a rise in sea surface temperature, a deepening of the thermocline, an increase in the surface mixed layer current velocity and the E-W and N-S directional barotropic current velocity, especially in the middle two periods on days 157 and 166 - 170.

4. The N-S direction of the barotropic current is dominated by the barotropic tide and the E-W direction of the barotropic current is more strongly influenced by the wind.

5. An increased surface mixed layer current velocity appears to be related to the strength of the wind. The interaction of wind and current velocity seems to hardly affect the lower mixed layer at the WIS09 mooring site. However, the 180 ° phase lag between the upper and lower part of the baroclinic current velocity, suggests an indirect path for wind impact on the lower mixed layer.

4.3 Observed data analysis

4.3.1 Estimates of bulk shear

Shear in the thermocline is a result of differences in the horizontal current velocity between mixed layers above and below the thermocline. Shear instability is the primary source of diapycnal mixing through the following process: The significant increases of shear, known as shear spikes, lead to a decrease of the Richardson number. When the Richardson number is below 0.25, shear instability is triggered and turbulent eddies are generated. The interaction of turbulent eddies will ultimately cause turbulent mixing and then develop into diapycnal mixing.

The variation in the depth of the thermocline makes it challenging to estimate the shear in the thermocline, so we use the bulk shear, which is the general shear between the surface mixed layer and lower mixed layer, to represent the shear variability in the thermocline. To calculate bulk shear, the average velocity difference between the surface mixed layer and the lower mixed layer has to be divided by the distance between two mixed layer centers [Burchard and Rippeth, 2009; Lincoln, 2012] according to the equation $S_{bk} = \frac{\overline{U_u} - \overline{U_b}}{h_{diff}}$ (as described in Chapter 2). The S_{bk} is the bulk shear, $\overline{U_u}$ is the mean velocity of the surface mixed layer, $\overline{U_b}$ is the mean velocity of the lower mixed layer and h_{diff} is the height difference between the centers of the two layers. Using this definition, the shear direction follows the surface mixed layer current velocity direction. In the calculation, the surface mixed layer is defined as -21.6 m to -11.6 m (fig 4.5), which equals 22 ADCP bins (an ADCP bin is a 0.5 m interval; see fig 4.2), and the lower mixed layer is defined as -35.6 m to -23.1 m, which equals 25 ADCP bins.

Fig 4.15 shows a time series of the evolution of bulk shear squared. It shows bulk shear squared spikes, which are periods of enhanced bulk shear squared, appearing occasionally in the time series of bulk shear squared, namely on days 157, 167 - 169 and 183 - 187. The bulk shear squared spikes, which range from 5×10^{-4} s^{-2} to 8×10^{-4} s^{-2}, are 5 to 8 times bigger than the normal bulk shear squared, where the average value is about 1×10^{-4} s^{-2}. Since the bulk shear squared spikes are significantly stronger than the normal shear, and since the Richardson number is defined as $Ri = \frac{N^2}{S^2}$ (where N^2 is buoyancy frequency squared and S^2 is the shear squared), shear squared spikes combined with a constant N^2 result in a reduced Richardson number, potentially leading to shear instability.

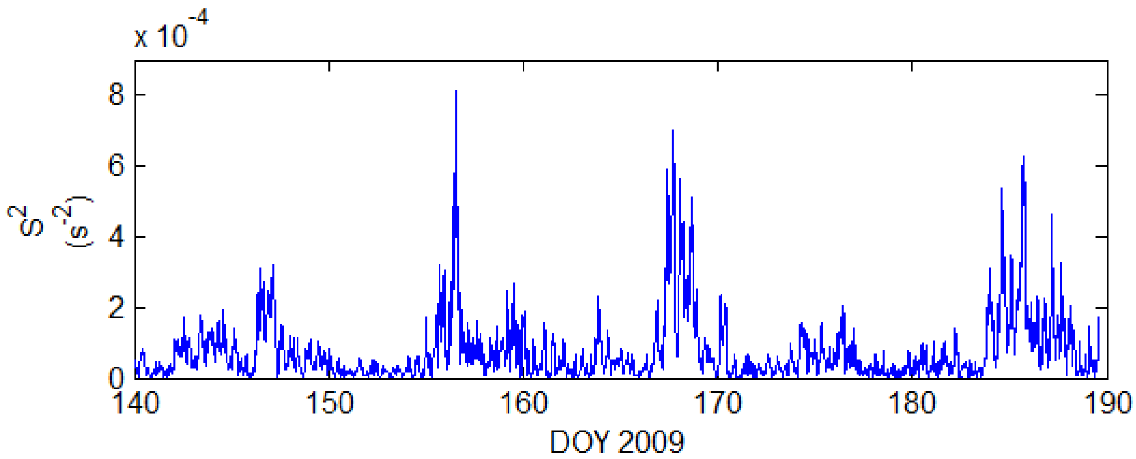

Fig 4.15 The bulk shear squared. The bulk shear squared represents the intensity of bulk shear, which is estimated from the observed mean current velocity difference of the surface mixed layer and lower mixed layer over the distance between the two layer centers at the WIS09 mooring site. Most of the time, the bulk shear squared is below 2×10^{-4} s^{-2}. However, there are three significant bulk shear spike events over the mooring period, which occur on days 157, 167 - 169 and 183 - 187. During these periods, the bulk shear squared is larger than 6×10^{-4} s^{-2}.

4.3.2 The dominant frequency of bulk shear

In order to further investigate the nature of the shear, rotary spectral analysis was applied to identify the distribution of bulk shear across the frequency domain. If the spectrum shows a concentration of power density on a certain frequency, this frequency is considered the dominant frequency of bulk shear.

The rotary spectrum of bulk shear for the period of the observations at WIS09 mooring site is shown in fig 4.16. The solid line is the anti-cyclonic component of bulk shear and the dashed line is the cyclonic component, whilst the grey bar indicates the local inertial frequency ($IF = 2\Omega sin\varphi$ where Ω is the rotation rate of the Earth and the φ is latitude. The local inertial frequency at the WIS09 mooring site is 0.0674 cycles per hour). Fig 4.16 reveals that the bulk shear during the mooring period is strongly associated with the near-inertial wave band. The bulk shear is dominated by anti-cyclonic rotation with negligible cyclonic movement.

The anti-cyclonic rotation at the inertial frequency of bulk shear is coincident with the movement of the inertial current on the Northern Hemisphere (anti-cyclonic rotation with inertial frequency), which implies that the bulk shear is correlated to the inertial current. As the inertial current is caused by a sudden change in wind direction or intermittent wind, the correlation of bulk shear and inertial current further implies that the bulk shear is correlated to wind.

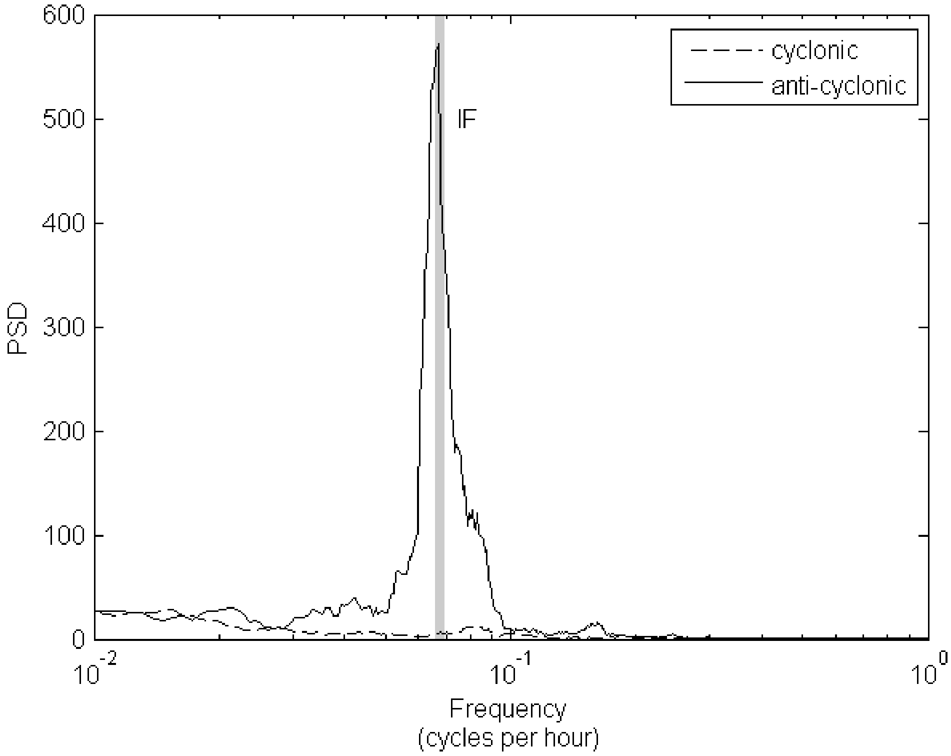

Fig 4.16 Rotary spectral analysis of bulk shear. The solid line indicates the anti-cyclonic constituent and the dashed line is the cyclonic constituent, the grey bar shows the position of the local inertial frequency (0.0674 cycles per hour at the WIS09 mooring site). The anti-cyclonic rotation of bulk shear dominates compared to the cyclonic rotation, and the dominant frequency of bulk shear is concentrated at the local inertial frequency.

4.3.3 Bulk shear and wind speed

The wind is generally quantified by two parameters: the wind speed and the wind direction. The momentum transfer from wind to the sea surface can be represented by wind stress τ_s. As shown in section 4.3.2, the bulk shear is dominated by the inertial frequency which is related to wind. To investigate the relationship between shear and wind, the role of each parameter in producing bulk shear must be identified.

Fig 4.7 shows that the changes in wind speed (panel a) are coincident with changes in the surface current (panel b). Furthermore, during periods of enhanced wind, the shear appears to be enhanced, as is evident in fig 4.17.

By comparing panel b and c in fig 4.17, it is clear that the general pattern of shear variation is similar to the variation of wind stress. It is obvious that the bulk shear peaks coincide with wind peaks on days 146 - 147, 155 - 157, 167 - 169 and 183 - 186. On the other days the wind is relatively weak and the bulk shear is low. A correlation analysis was applied between the shear variation and wind variation, and the result (r = 0.46) suggests that the bulk shear variability is a response to the wind intensity.

The other phenomenon shown in fig 4.17b and c is that on some days, for example days 156 - 157, strong winds coincide with significantly enhanced shear. However, there are also some periods with strong winds but weak bulk shear, for example days 142 - 143. This implies that the bulk shear is not simply related to the enhanced wind speed.

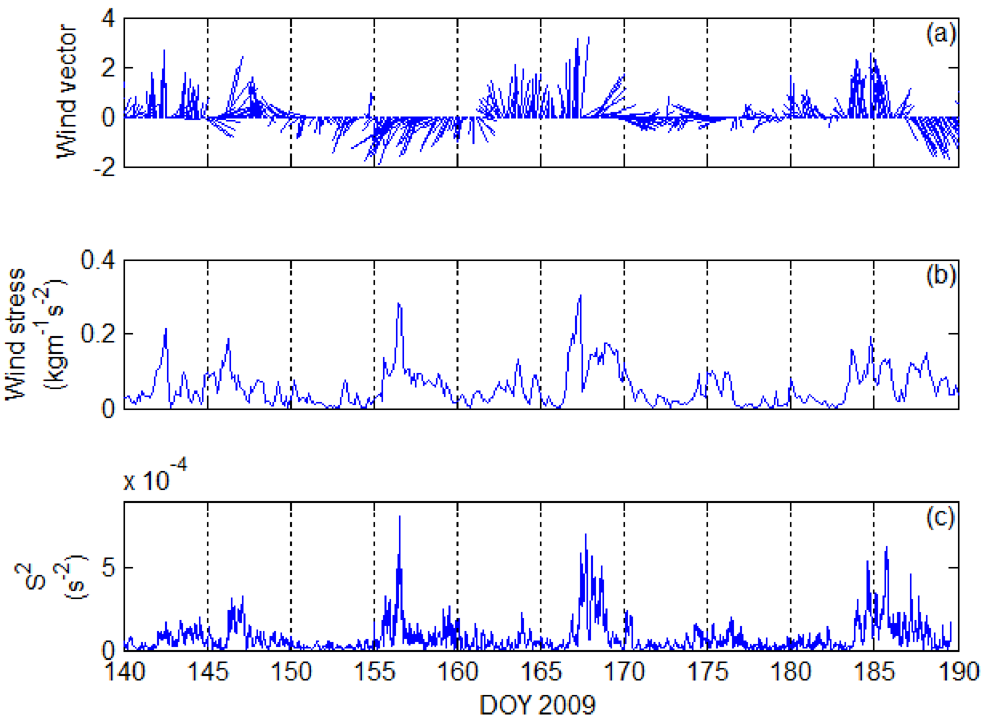

Fig 4.17 The relationship between wind stress and bulk shear squared. a) The time series of wind vector (see fig4.5); b) wind stress estimated from wind vector (equations 2.1 - 2.3 in Chapter 2). The wind stress in panel b is directly proportional to wind speed (in panel a); four main wind stress spikes (over 0.2 $kgm^{-1}s^{-2}$) occur on days 143 - 146, 157, 167 - 169 and 184 - 186; c) bulk shear squared from observations at the WIS09 mooring site (see fig 4.14)

4.3.4 Bulk shear and wind direction

The evolution of bulk shear squared $\frac{dS^2}{dt}$ is a suitable parameter to investigate the energy transport related to production of bulk shear squared. Positive $\frac{dS^2}{dt}$ indicates a growth in bulk shear and implies an energy input, while a negative $\frac{dS^2}{dt}$ suggests a decrease of bulk shear intensity. Fig 4.18 shows a comparison of bulk shear squared, wind-bulk shear vector directions and the evolution of bulk shear squared. Panel a shows the time series of bulk shear squared in which three significant shear spikes can be discerned. Panel b displays the angle between wind vector and bulk shear vector. Panel c shows the time series of bulk shear squared. The evolution of bulk shear squared reaches its peak (panel c) when the wind vector aligns with the bulk shear vector (panel b). This is the moment (orange dashed line) of the maximum rate of transfer of energy. After around 3.5 hours (interval of time between orange dashed line and red dash-dotted line), with the angle between bulk shear and wind enlarged to 90° (panel b), the transfer of momentum ceases to augment the shear, the bulk shear hits its peak value (panel a) and $\frac{dS^2}{dt}$ becomes 0 (panel c). From day 183.5 to 186, wind and shear alignment (at times indicated by the position of orange lines) is a key process in creating shear spikes. It suggests that the shear spike is created by alignment of wind and bulk shear, and hence that shear spike production is related to both factors of the wind-shear direction and the magnitude of wind velocity. A similar conclusion has been drawn earlier by Burchard and Rippeth [2009], Lincoln [2012] and Brannigan et al. [2013].

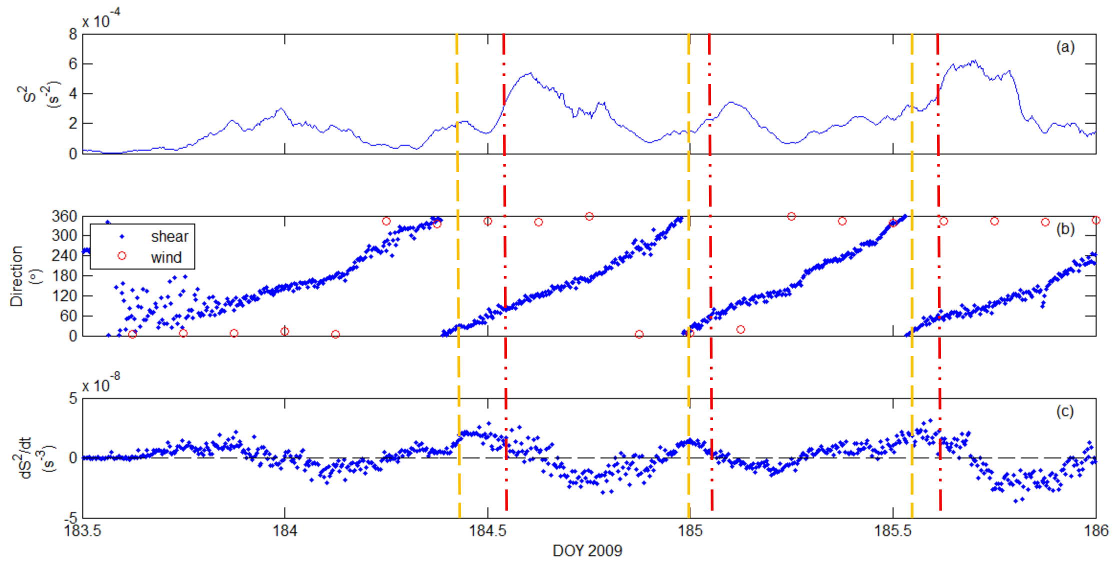

Fig 4.18 Relationship between shear spikes, evolution of bulk shear squared, and bulk shear-wind vector alignment. a) Bulk shear squared (see fig 4.15); b) comparison of bulk shear direction and wind direction: red circles are the wind direction, which is almost constant at around 0° from day 183.5 - 186, and the blue dotted lines are the shear directions, which rotate anti-cyclonically with a period of 0.6 - 0.8 days; c) blue dotted lines are the evolution of the bulk shear squared from observation, which have a period of 0.6 - 0.8 days. The orange dashed lines show the times when wind and bulk shear vectors are aligned (on days 184.4, 185 and 185.6) and the times when evolution of bulk shear squared reaches its peaks. The red dash-dotted lines show the times that wind and bulk shear vectors are at about 90° (on days 184.6, 185.1 and 185.7), which are also the times when bulk shear squared hits 0, and the bulk shear spike occurs.

4.4 1D Two-Layer Vertical Dynamic Numerical Modelling

To test the idea that the spikes in shear are a result of wind-shear alignment we apply a 1D two-layer vertical dynamical numerical model [Burchard and Rippeth, 2009] to attempt to replicate the shear creation at the WIS09 mooring site.

Detailed information on the philosophy, the assumptions and the equation derivation of the model are shown in Chapter 2. The model equation is:

$$\partial_t S^2 = \frac{4}{h}\vec{S}\cdot\left(\frac{\vec{\tau_s}}{h_s}+\frac{\vec{\tau_b}}{h_b}\right) - C_i\frac{h^2}{h_s h_b}S^3 = P(S^2) - D_i(S^2) \tag{4.3}$$

Where $\frac{\vec{\tau_b}}{h_b}$ represents the tide forcing, $\frac{\vec{\tau_s}}{h_s}$ represents the wind forcing, and the $C_i\frac{h^2}{h_s h_l}S^3$ represents bottom friction. $S^2$is the bulk shear squared; $\vec{\tau_s}$ is the surface shear stress vector and $\vec{\tau_s} = \tau(0)$; $\vec{\tau_b}$ is the bottom shear stress vector and $\vec{\tau_b} = \tau(h)$; h is the water column depth; h_s is the surface mixed layer thickness; h_b is the lower mixed layer thickness; C_i is the interfacial drag coefficient; $P(S^2)$ is the production of bulk shear squared; and $D_i(S^2)$ is the interfacial friction.

To quantify the bulk shear contribution from wind and tide individually, two modelling processes were applied. The first one assumes that the model is only driven by wind, while the second one assumes it is only driven by the tide. To test the ability of the model to reproduce the observed shear squared production for the WIS09 mooring site, a third model run was performed to test the model in a combined wind and tide driven scenario. The predicted shear squared production for each of the three model runs is shown in fig 4.19. The red line is shear squared production from the model that was driven by both wind and tide; the black line only by wind, the green line only by tide, and the blue dotted line is the evolution of bulk shear squared $\frac{dS^2}{dt}$ (or $\partial_t S^2$) as estimated from observation.

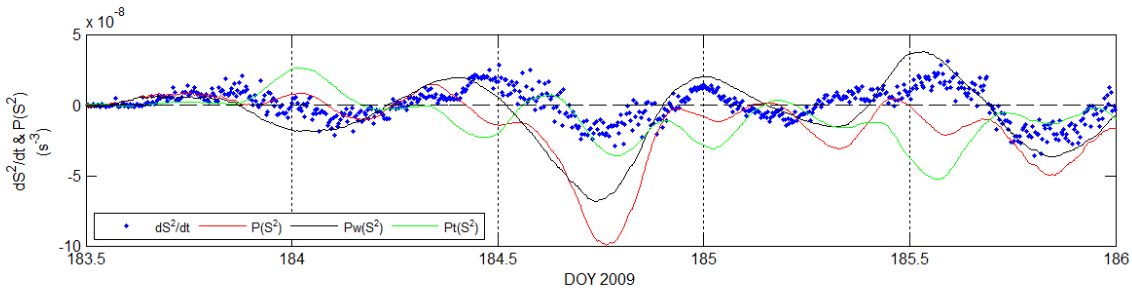

Fig 4.19 Similarity of evolution of bulk shear squared (blue dotted line) and the two-layer modelled shear squared productions (solid lines) (details of two-layer model in Chapter 3). Three separate model runs related to shear squared production: one shows the model runs with only wind forcing (black line), one is the model runs with only tide forcing (green line) and the third displays the model runs under combined wind and tide forcing (red line). Correlation analysis of observations and the model results are: r = 0.68 (wind only model), r = 0.23 (tide only model), and r = 0.48 (combined force model). The wind only model provides the beast correlation.

From the results presented the best agreement with the observed evolution of shear squared production is obtained for the case of only wind driven mixing (r = 0.68). The tide driven model renders less precise fits (r = 0.23) as is also the case with the combined wind and tide driven scenario (r = 0.48) (detailed information see section 4.5).

To further investigate the relationship between the wind, tide, and evolution of shear, a coherence analyses was carried out using the observed time evolution of bulk shear squared and the three model predictions.

4.5 Modelled data analysis: correlation and coherence analysis

In order to further examine the relationship between wind velocity, barotropic current velocity, and bulk shear, we performed a correlation and coherence analysis between boundary stress and bulk shear. Correlation analysis helps to identify any relationships between the two time series in the time domain. More specifically, coherence analysis reflects any relationship in a spectral domain and identifies any relationship between variations of the two signals. Detailed explanation of the analysis methods can be found in Chapter 2.

The results of the coherence analysis are shown in fig 4.20, which examines the relationship between the bulk shear and boundary stress (the surface stress from wind and the bottom stress from barotropic tide).

As introduced in section 4.2.2, the surface stress is estimated based on a low resolution reanalysis of meteorology data from the Met Office. It is worth noting that the low resolution may reduce the strength of the correlation.

In fig 4.20 the very low *r* value of 0.04 (dashed line) indicates that there is no clear relationship between bulk shear and the bottom stress. There is a stronger relationship between bulk shear and surface stress with an *r* value of 0.46 (solid line). The highest coherence between the bulk shear squared and surface stress is nearly 1, and is found at low frequency (between 10^{-3} and 10^{-2} cycles per hour). This relationship indicates that the underlying low frequency component, which represents the basic shear pattern, is strongly related to the windy events. In other words, low frequency variability of the bulk shear can be explained by the low frequency variability of the wind due to the passage of strong wind events. There is no peak of inertial frequency and the M2 tidal frequency in the wind data as the wind does not naturally contain these two frequencies.

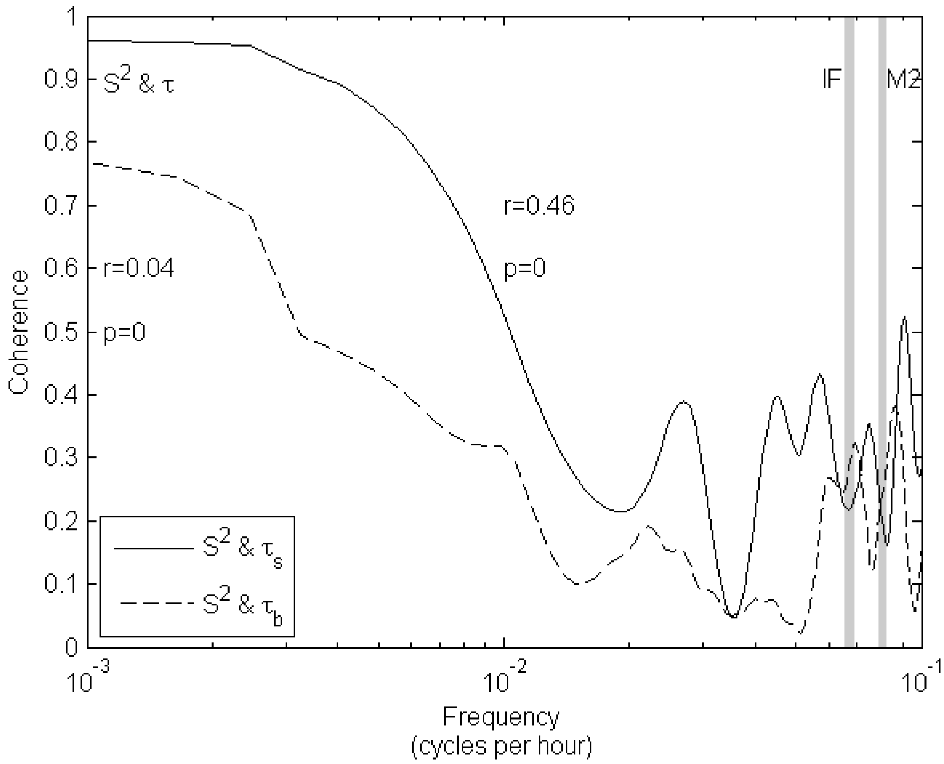

Fig 4.18 Correlation (r and p values) and coherence (dashed and solid lines) analysis of bulk shear squared and boundary stresses. The coherence of bulk shear square with wind stress (solid line) and bed stress (dashed line) are shown, as well as the r and p values. For both conditions, the p values are below 0.05; the higher *r* value (0.46) for the surface stress than the bottom stress (0.04) indicates this parameter is more important. The two grey bars show the position of the inertial frequency (shown as IF, 0.07 cycles per hour) and the M2 tidal frequency (0.08 cycles per hour). The coherence of the bulk shear squared and surface stress shows several peaks over the frequency domain. However, the peaks we are concerned with in this figure are in the low frequency section (10^{-3} - 10^{-2} cycles per hour). The coherence at low frequency close to 1 suggests enhanced shear tends to correlate with windy periods, which also have a low frequency. The inertial frequency and M2 tidal frequency are ignored because the surface stress does not naturally contain these two frequencies, and thus should not have a frequency in common with the bulk shear at inertial frequency and M2 tidal frequency.

In order to investigate the role of wind and tide in shear production respectively, the coherence of modelled shear squared production and the time evolution of bulk shear squared are shown in figs 4.21 - 4.23.

Fig 4.20 shows the observed S^2 and S^2 as provided by the tide only model, the r value (r = 0.23) is smaller than that of the other two comparisons: r = 0.48 for the combined wind and tide model (fig 4.21), and r = 0.68 for the wind only model (fig 4.23). Even though the barotropic tide could have impact on the shear generation across thermocline through bottom stress, however from fig 4.20 and section 4.3.2, the tide is not the dominant driver in the production of shear at WIS09 mooring site. The higher *r* value in figs 4.21 and 4.23 further proves this conclusion. Modelled shear squared production driven by wind as shown in fig 4.23 is strongly related to the observations, especially at inertial frequency. In fig 4.21, there is a coherence peak at inertial frequency, unlike in fig 4.22. Comparing figs 4.21 and 4.23 leads to the following observations：

1. The correlation coefficient r is higher in the model with wind forcing (fig 4.23, *r* = 0.68) rather than with wind and tide forcing combined (fig 4.21, *r* = 0.48). This suggests that the inclusion of the tide reduces the agreement between the model and the observations in shear squared production, and that the wind is the key driver in shear squared production. Alternatively, the model may miss some physical process responsible for producing shear driven by tide at the WIS09 mooring site.

2. Figs 4.21 (combined model) and 4.23 (wind only model) both show coherence peaks that appear in figs 4.21 and 4.23 are at the inertial frequency. The location of coherence peak shows that among all the components with different frequencies, the most similar components of shear squared production and time evolution of bulk shear are their inertial frequency components. These peaks imply that the ability of the models to reproduce the wind-driven currents at the inertial frequency is better than at other frequencies. Here, with wind as the only driver, when compared to other driver conditions, these two time series data sets have the strongest correlation. Thus the model performs better in reproducing the observations if the observation contains a higher percentage of inertial frequency energy and a lower percentage of tidal frequency energy. This implies that the model performs better for regions with strong wind and weak tides.

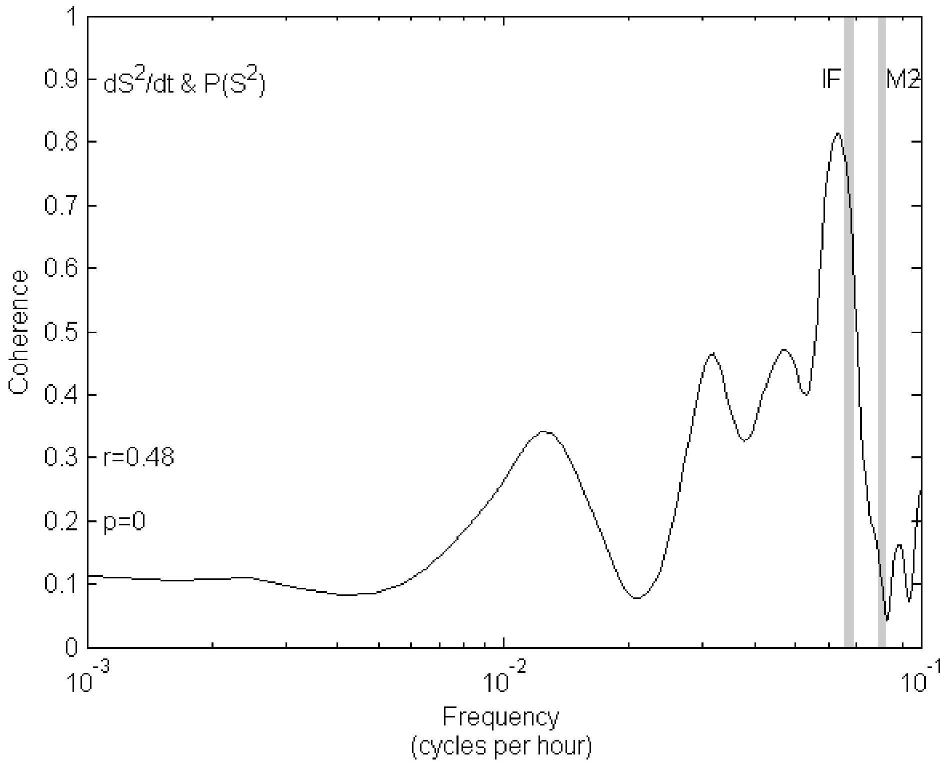

Fig 4.21 Correlation (r and p values) and coherence (solid line) analysis of observed bulk shear squared and two-layer modelled (combined wind and tide model) shear squared production. The *r* value 0.48 shows that these two factors are related, and the $p < 0.05$. The peak value (0.81) near the inertial frequency indicates a strong similarity of near inertial frequency components in the observation and the model. The trough near the M2 tidal frequency indicates they hardly have common components at this frequency.

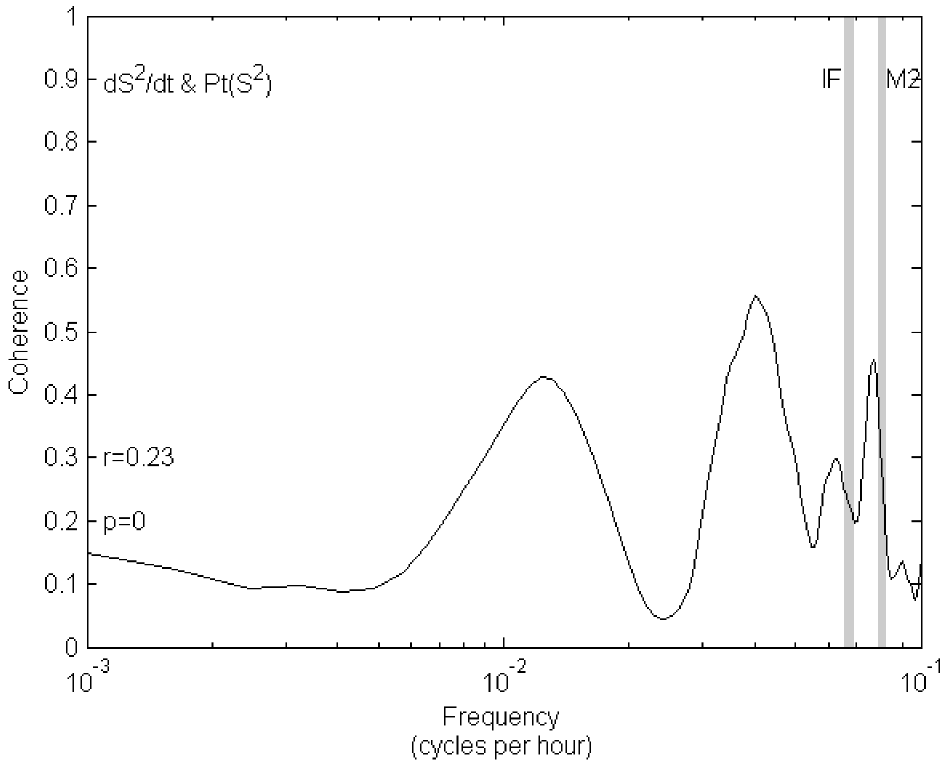

Fig 4.22 Correlation (r and p values) and coherence (solid line) analysis of observed bulk shear squared and two-layer modelled (tide only model) shear squared production. The low *r* value 0.23 shows these two factors are hardly related, *p* value is < 0.05. Even though there is a peak value at M2 tidal frequency which of interest, due to the weak *r* value, the coherence is considered to be less important.

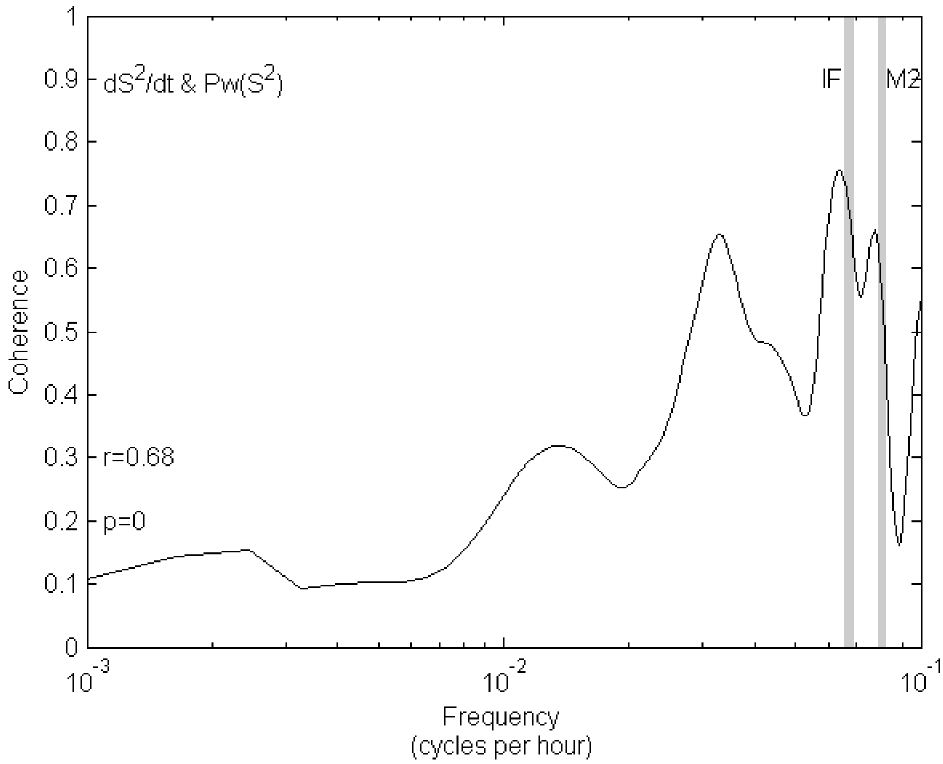

Fig 4.23 Correlation (*r* and *p* values) and coherence (solid line) analysis of observed bulk shear squared and two-layer modelled (wind only model) shear squared production. The *r* value 0.68 shows these two factors are related, and the *p* value < 0.05. There are two peaks at the near inertial frequency (the peak value is 0.76) and the near M2 tidal frequency (the peak value is 0.66) respectively. The peak at near inertial frequency is the greatest among all the peaks which shows that shear squared production from the wind driven model has the greatest similarity with the evolution of bulk shear squared at the near inertial frequency. The peak at the M2 tidal frequency is an issue worth studying in the future, since the evolution of bulk shear squared from observation may contain the M2 tidal frequency, but it is not a natural frequency component in a wind driven motion. A way to explain that is that the current velocity data used to run the model comes from observations which may introduce some tidal signal to the model, thus even though the model is purely wind driven, the results may still contain M2 tidal frequency.

4.6 Summary

1. The temperature variation is the dominant factor determining the variation of density structure at the WIS09 mooring site.

2. During the mooring deployment, the water column structure developed from weak stratification with a shallow thermocline, to strong stratification with a deep thermocline.

3. During the mooring deployment, the periods of increased wind speed are coincident with periods of increased sea surface temperature, thermocline deepening and baroclinic current velocity increase.

4. There is a 180° phase lag of baroclinic velocity currents between the surface mixed layer and the lower mixed layer.

5. At the WIS09 mooring site, the production of shear over the thermocline is dominated by the current velocity interacting with wind rather than tide. The low frequency (10^{-3} to 10^{-2} cycles per hour) bulk shear is driven by low frequency wind stress which is linked to the passage of strong wind events. The timing of the high frequency shear spikes is related to wind-shear vector alignment.

6. The two-layer model performs better in producing the shear squared production near inertial frequency than at other frequencies. The stronger the inertial frequency component in the observation is, the better the model skill to replicate the observations.

Chapter 5

Shear generation towards the breakdown of seasonal stratification

In this chapter the data collected in the seasonally stratified zone of the northern North Sea (hereafter NNS) during the autumn of 1998 are presented and analysed, with the specific aim of identifying the dominant driver for the bulk shear, and consequently the diapcynal mixing, within the thermocline in the NNS site during the autumn stratification decline. The same two-layer model that was used in the previous chapter, is combined with observations to aid the interpretation of the data and the identification of the key processes responsible for the enhanced shear across the thermocline.

5.1 Data collection

The observed data from NNS used in this chapter was collected as part of the PROcesses of Vertical Exchange in Shelf Seas (PROVESS) project and is available on British Oceanographic Data Centre (BODC) website (https://www.bodc.ac.uk/data/bodc_database/). The sea water salinity, the sea water temperature, the water current velocity and the meteorology data (wind speed and wind direction) are available. More detailed information on PROVESS project can be found in Howarth et al. [2002].

The salinity and temperature single profiles covering the entire water column. They were collected using a CTD from the research vessels at the beginning and at the end of the period of interest: on 8th September and 2nd November in 1998.

The first CTD profiles were collected during the cruise VLD174 (PROVESS N-1). The cruise period was from the 5th September to the 17th September 1998, and was organised by the Alfred Wegener Institute, Helmholtz Centre for Polar and Marine Research, Germany. The instrument used in this cruise was a Sea-Bird SBE 911 CTD, with a water temperature sensor, a conductivity sensor and a Paroscientific Digiquartz pressure sensor. All the sensors were deployed at the same depth and set at a sampling frequency of 24 Hz. The data used in this study is the practical salinity and temperature of the water body. The location of the cast was 59 ° 19.8' N and 1 ° 0.4' E (see fig 5.1, site R), the mean depth was 104.0 m and the profile covers almost the whole water column, from -103.25 m to -1.98 m.

On the 2nd November the final profile was collected using a Neil Brown MK3 CTD with a water temperature sensor, a salinity sensor and a pressure sensor. The cruise was organised by Proudman Oceanographic Laboratory (now National Oceanography Centre, Liverpool), United Kingdom. The cast location was 59 °20.0' N, 0 °59.8' E (see fig 5.1, site A), the mean depth was 109.3 m and the profile covers from -105.47 m to -1.49 m. As in the former cruise, the sensors were all grouped at the same depth.

The time series of the sea temperature profile is measured from a subsurface mooring which was deployed by FS Valdivia (cruise 174) on 10th September 1998 (day 245) and recovered by RRS Challenger (cruise 140) on 1st November 1998 (day 305). The mooring nominal sampling interval is 5 minutes (300 s). The data was collected through an Aanderaa thermistor chain (a 50 m thermistor chain mooring with sub-surface buoyancy) with 11 water temperature sensors, the interval of the sensor is 5 m. The thermistor chain was deployed at 59°20.0' N, 1° 5.0' E (see fig 5.1, site X) where the mean depth is 113 m and the profile covers from -87.32 m to -37.32 m.

The current data were collected by a 150 kHz RDI Broad Band ADCP (Acoustic Doppler Current Profiler) with Bottom Pressure Recorder, which was mounted as fixed benthic lander from the 7th September to the 2nd November 1998 and located at 59°20.0' N and 1°25.1' E (see fig 5.1 site U). The data was collected with a temporal resolution of 10 minutes (600 s), and the instrument mounted in the frame (seabed lander-Workhorse Doppler frame D1) sat at 0.5 m above sea bed. The mean depth at this location is 107 m and the ADCP spans a range from -94.5 m to -10.5 m. The ADCP sampled over 21 bins with a resolution of 4 m. The centre of bin 1 was at -96 m.

The meteorology data from PROVESS project was collected from a moored surface meteorology buoy located at 59°20.6' N, 0°59.7' E (see fig 5.1, site S), over the period from the 6th September to the 16th October 1998 with a nominal sampling interval of 10 minutes. However, the wind direction data was invalid due to the vane being damaged by a rope during the deployment. There are two alternative meteorology data sources: one is observations from a nearby met station on the Frigg Oil Rig, which has a temporal resolution of 20 minutes (1200 s) and located at 59°54.0' N and 2°6.0' E (see fig 5.1 site Frigg Oil Rig). Another one is a European Centre for Medium-Range Weather Forecasts (ECMWF) reanalysis meteorology data, which has a much lower temporal resolution (6 hours). The resolution of meteorology data does not affect the general pattern of the production of bulk shear squared from 1D two-layer vertical dynamic numerical modelling, which will be introduced later in section 5.4, but it would contribute to a better performance in reproducing a detailed structure of the bulk shear square production and gain advanced accuracy in modelling (see fig 5.2).

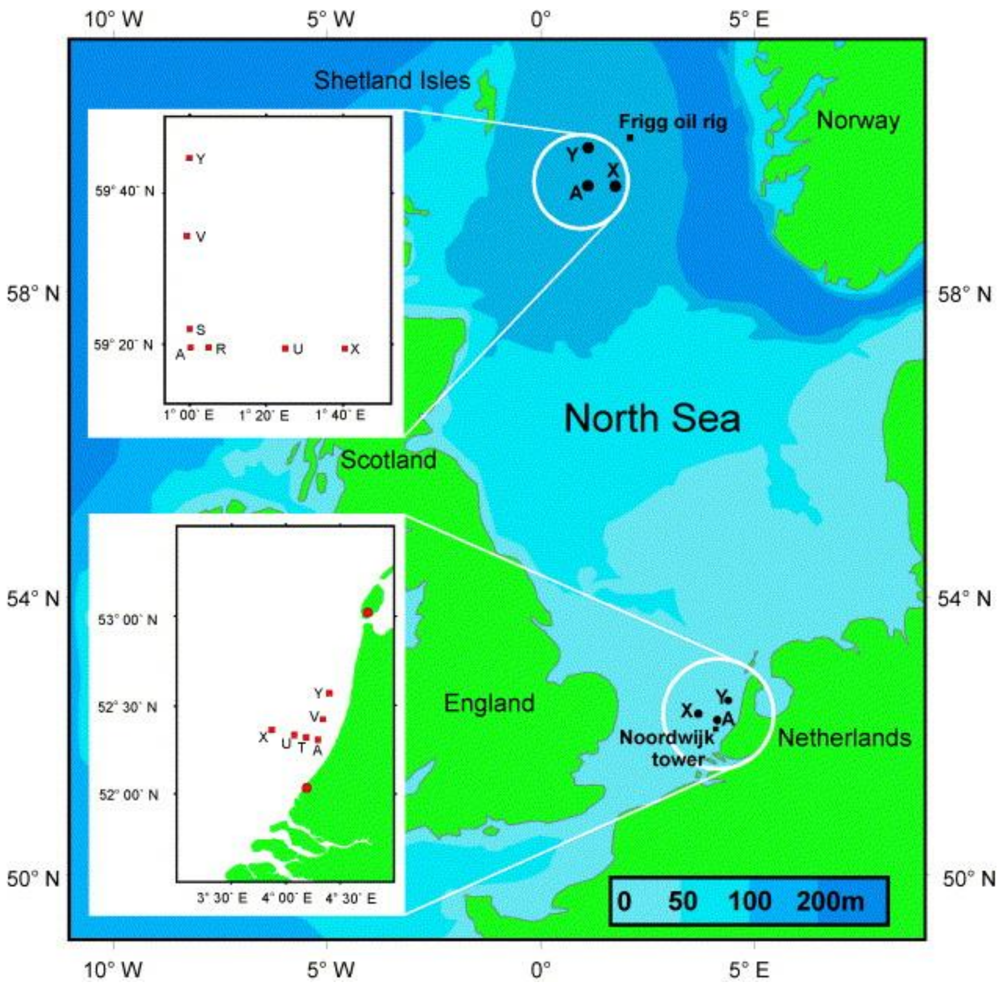

Fig 5.1 The mooring arrays of the PROVESS project in the North Sea. Both the mooring arrays in the northern North Sea (NNS) and southern North Sea (SNS) are displayed on the figure. However the mooring sites at SNS are less important since the observation data in this chapter are all from NNS. Six mooring sites are related to our study: the location of the first CTD cast during the cruise VLD174 was at 59° 19.8' N and 1° 0.4' E (site R); the location of the second CTD cast was at 59°20.0' N, 0°59.8' E (site A); the location of the moored thermistor chain was at 59°20.0' N, 1° 5.0' E (site X); the location of the mounted ADCP was at 59°20.0' N and 1°25.1' E (site U); the location of the moored surface meteorology buoy was at 59° 20.6' N, 0° 59.7' E (site S); the location of the nearby met station on the Frigg Oil Rig was at 59°54.0' N and 2°6.0' E (Frigg Oil Rig). [Howarth et al., 2002]

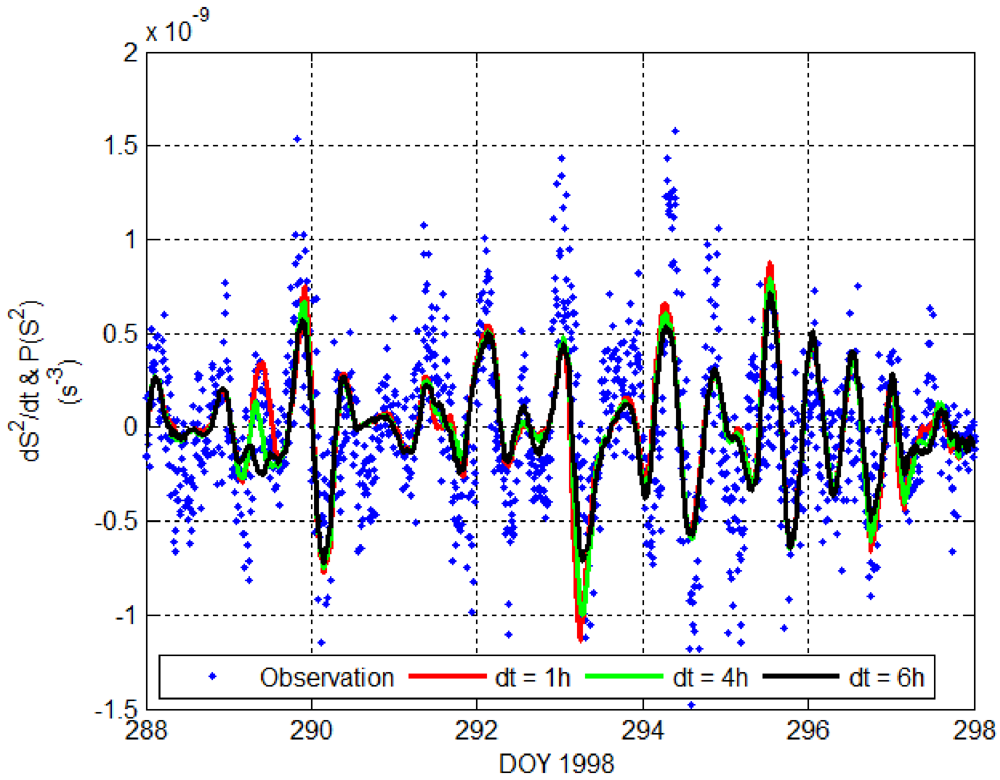

Fig 5.2 The example of 1D two-layer vertical dynamic numerical modelling with different resolutions of meteorology data. The blue dotted line is the time evolution of bulk shear squared estimated from observed water current velocity at NNS site. The three solid lines are the modelled production of shear squared with different temporal resolution of initial meteorology data. The period is days 288 - 298. The initial meteorology data is from the Frigg Oil Rig site and is time averaged to get the temporal resolution of 1 hour (red line), 4 hours (green line) and 6 hours (black line). The original temporal resolution of meteorology data is 20 minutes. The general patterns of three modelled lines are coincident most of the time, while in some detailed structures, for example the production of bulk shear squared on days 289 - 289.5, 293 - 293.3 and 297 - 297.5, the production of bulk shear squared with different temporal resolution (three solid lines) diverge especially on days 289 - 289.5. The modelled result with finer temporal resolution (red line, the resolution is 1 hour) of initial meteorology data fits the peaks of observed time evolution of the bulk shear squared better than the modelled result with coarse temporal resolution (black line, the resolution is 6 hours), which is obvious on days 289 - 289.5, 289.7 - 290, 293 - 293.3, 294.2 - 294.3, 295.3 - 295.5, 296.6 - 296.8 and 297 - 297.5.

The meteorology data of the Frigg Oil Rig is collected from a fixed platform and is supplied by the Norwegian Meteorological Institute (DNMI). The nominal cycle interval is of 20 minutes (1200 s) and is recorded from the 7th September to the 6th November (days 250 - 310). The in-situ anemometer is at the sea surface but is corrected to 10 m above sea level. The wind direction data should be used with caution since the direction in meteorological convention (the direction the wind blows ‘from’) is opposed to oceanographic convention (the direction the water flows ‘to’). We must take care not to directly compare the different conventions, but to transform directions to the same convention system.

The selected ECWMF reanalysis is the ERA-Interim. ERA-Interim data assimilated from the reanalysis system start from 1979 and keep updating with real time. Detailed information of ERA-Interim can be found in Berrisford et al. [2011] and Dee et al. [2011].

Fig 5.3 shows the comparison of the wind speeds (panel a) and directions (panel b) from these three sources. The blue line represents the meteorology data from local observation in PROVESS project, the black line is the ERA-Interim data and the red line is the Frigg Oil Rig data. In panel a, the general pattern of the wind speeds from three sources coincide and thus the wind speeds from Frigg Oil Rig site (red line) and ERA-Interim (black line) are all worth trusting. Therefore, they can be used to represent the local observation of wind speed. In panel b, the wind directions from the Frigg Oil Rig site (red line) and the ERA-Interim (black line) are coincident. The final selected meteorology data is the observation from the Frigg Oil Rig since its resolution (20 minutes) is finer than the ERA-Interim (6 hours) and thus is more likely to reveal more detailed information about the wind evolution.

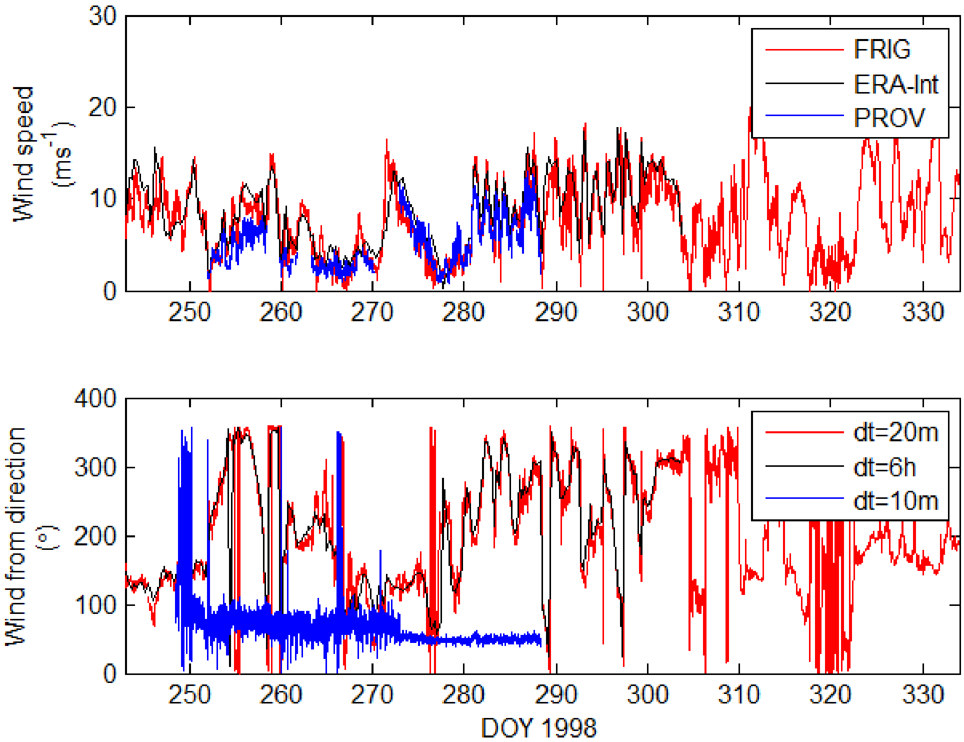

Fig 5.3 The meteorology data from three sources: the observed data from a fixed platform of Frigg Oil Rig (red line), the ERA-Interim reanalysis data from ECMWF (black line) and the moored data at NNS mooring site (blue line). The time resolutions are 20 minutes, 6 hours and 10 minutes respectively, and the time periods are days 243 - 334 (red line), 243 - 304 (black line) and 248.5 - 319.4 (blue line) respectively. Panel a represents the time series of wind speed and panel b shows the time series of wind direction. In panel a the general pattern of three time series of wind speed are coincident with each other, however the differences of wind speed magnitudes are obvious, especially on days 255 - 258, the average wind speed (10.5 ms^{-1}) from PROVESS project is about 1.5 times bigger than the average wind speed (7 ms^{-1}) from ERA-Interim reanalysis data. In panel b, the wind direction from the ERA-Interim reanalysis data (black line) coincident with the moored Frigg Oil Rig data (red line), and the moored data from NNS site (blue line) had been polluted, due to the direction vane damaged by a rope during the deployment and thus is not suitable to be used in the study. The meteorology data chosen in the study is the moored Frigg Oil Rig data, based on its high temporal resolution and reliability on both wind speed and wind direction. Part of the magnitude differences in both panels is from the difference of temporal resolution of data, which the data with finer resolution will present more oscillations.

Although the mooring/CTD sites differ geographically, previous study had shown hydrographic conditions to be horizontally uniform in the seasonally stratified NNS [Howarth et al., 2002]. For the purpose of this study, all the data is considered to be collected at one location and the theoretical site is named as NNS site which is located at 59 °20.0' N and 1 °E.

5.2 Stratification of the NNS site

5.2.1 Two factors that affect stratification: temperature and salinity

I. Evolution of temperature and salinity structure

At the beginning of the period of interest, on the 8th September, the sea temperature of the surface mixed layer was close to 12.7℃ , whilst that of the lower mixed layer was of about 7.9℃ in the NNS site. By the 2nd November, the surface mixed layer and the lower mixed layer water temperatures were 9℃ and 7.6℃ respectively (fig 5.4). The thickness of the thermocline reduced from 13 m (September) to 3 m (November) and the temperature difference between the surface and lower mixed layers decreased from 5.5℃ (September) to 1.8℃ (November). The bottom boundary of thermocline stayed at the same depth of -48 m whilst the upper boundary of the thermocline, deepened by 12 m from -45 m to -33 m. On the 8th September, the temperature structure below -48 m remained very weakly stratified with an average difference in temperature of 0.3℃. This can be compared to the temperature structure above -48 m when the temperature difference was about 3.7℃.

On 8th September 1998, the salinity had a three layer structure (fig 5.4 panel a) with a salinity of 34.4‰ above -3 m, the value of 34.7‰ between -15 m and -5 m and an average salinity of 35.3‰ between -104 m and -20 m. On 2nd November, a two layer salinity structure replaced the three layer structure observed in September. The two layers are the surface mixed layer, above -45 m (the salinity is 34.75‰) and the lower mixed layer, below -48 m (the salinity is 35.25‰).

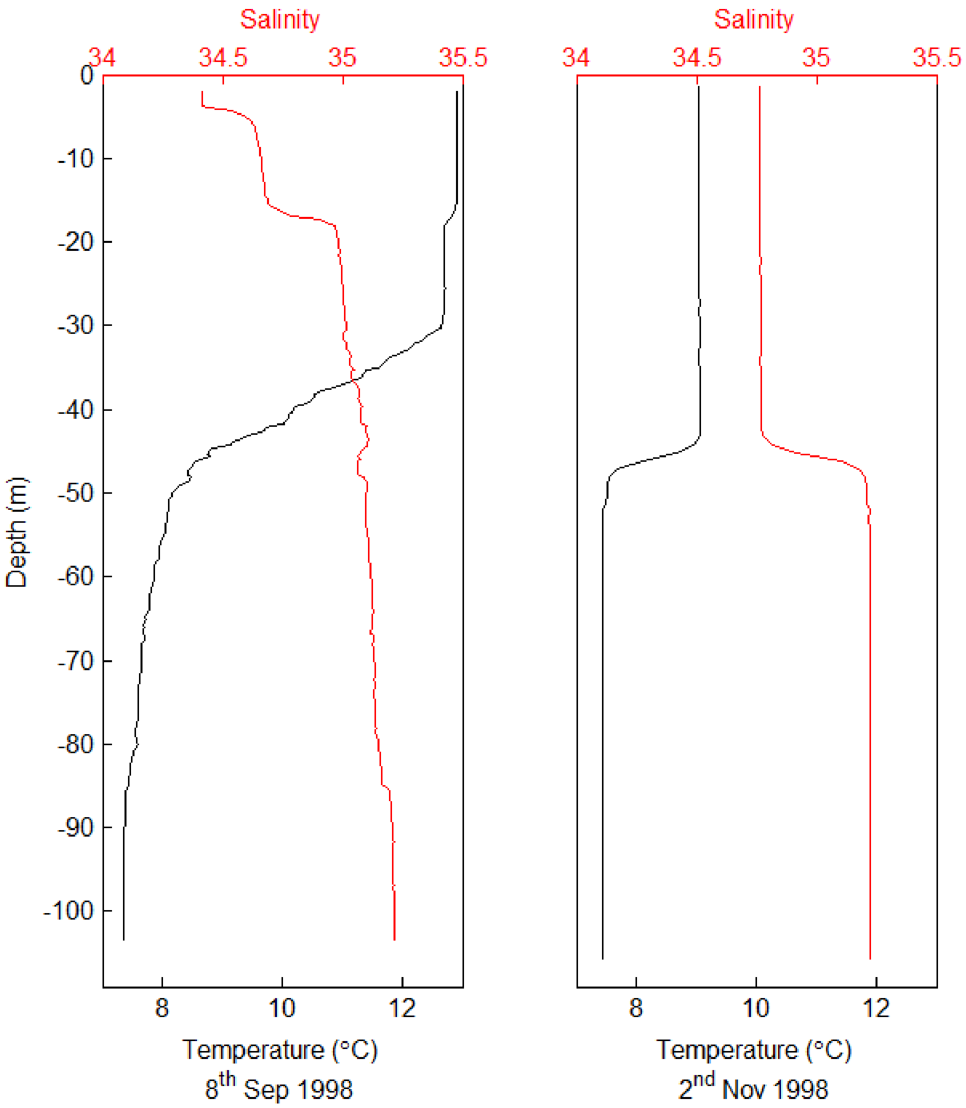

Fig 5.4 The temperature and salinity profiles at NNS site on the 8th September and the 2nd November 1998. The black line is the profile of the temperature and the red line is the profile of salinity. Except for the bottom 14 m, the temperature profile decreases from September to November over the whole water column. The largest temperature decrease is from 12.7℃ (September) to 9℃ (November) at the surface mixed layer (-33 m to 0 m) and the average temperature of the lower mixed layer (-104 m to -48 m) decreases from 7.9℃ to 7.6℃. The temperature variation of the surface mixed layer (3.7℃) is higher than that of the lower mixed layer (0.3℃). The thermocline thickness decreases from 13 m (panel a) to 3 m (panel b). The salinity increases over the whole water column from September to November except for the bottom 14 m. In September, the salinity profile is structured with a three layer shape, the first mixed layer (3 m thick) at sea surface with the salinity of 34.4‰, the second mixed layer at -15 m to -5 m with the salinity of 34.7‰ and the lowest mixed layer (-104 m to -20 m) which has a linear salinity profile with an average salinity of about 35.3‰. The salinity profile on 2nd November has a two layer structure. The two layers are from -45 m to 0 m and from -104 m to -48 m. The halocline becomes deeper, and the salinity difference in the two layer (0.5‰) system is slightly larger than that of three layer structure (0.25‰ and 0.3‰). In the two layer structure, the salinity of the surface mixed layer is 34.75‰ and the salinity of the lower mixed layer is 35.25‰.

II. Evolution of water stratification

The essential parameter in the study of water stratification is water density. The sea water density is determined by the salinity, the temperature and the water pressure based on the equation of state for sea water:

$$\rho = \rho(T, S, P) \tag{5.1}$$

Because of the shallow depths of shelf seas, it is normally possible to neglect the effects of pressure on density. In fig 5.5, three density profiles, one with a temperature only contribution (blue line), one with a salinity only contribution (green line) and the third with the combined temperature and salinity contribution (red line), are calculated in order to show the contributions of salinity and temperature according to equation 5.1. The calculation is accomplished by the Matlab routine sw_dens0.m [Morgan, 1992].

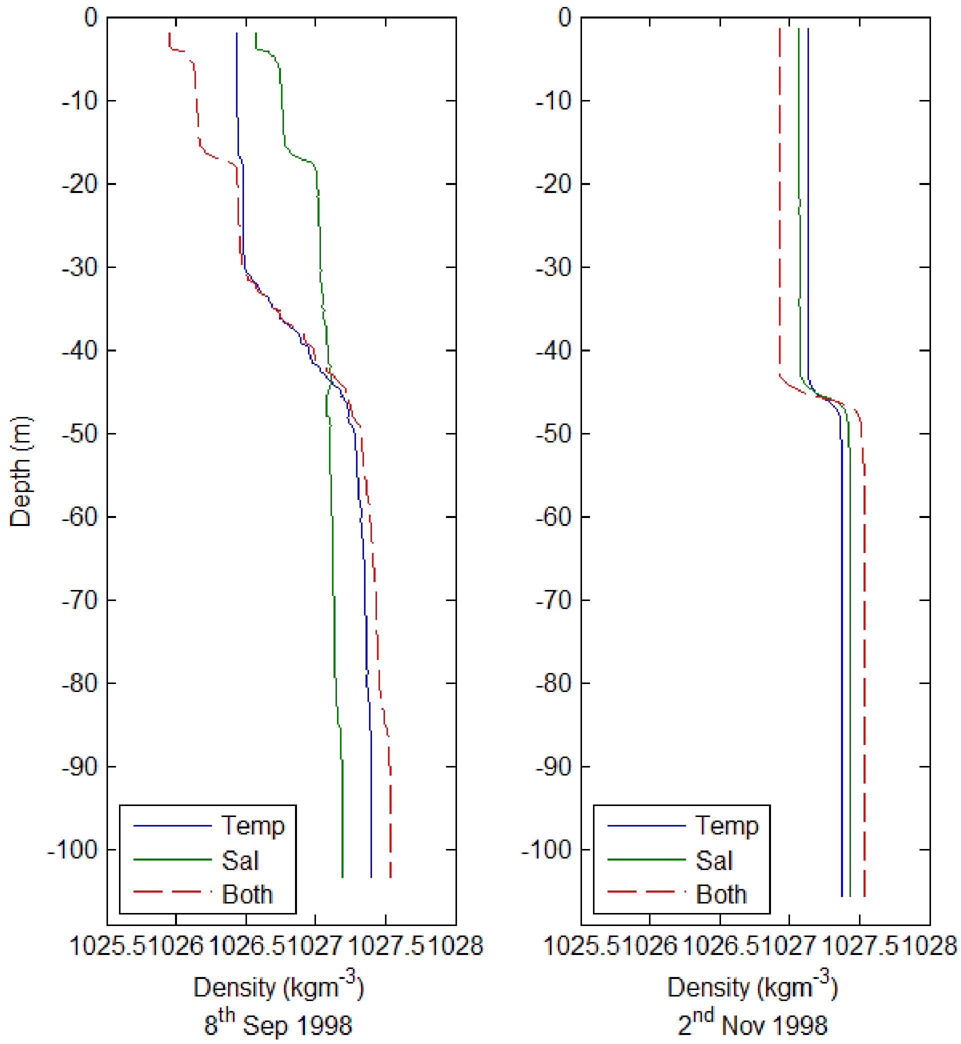

Fig 5.5 The contribution of temperature and salinity to the density profile on the 8th September and the 2nd November 1998. The blue line is the temperature only contribution to the density profile, the green line is the salinity only contribution to the density profile and the red line shows the density profile, which is clearly affected by both the salinity and the temperature, for this reason it is named 'both' in reference to this combined contribution. Panel a shows that both salinity and temperature could contribute to the density. However the strongest density variation, which is the density difference from 1026.5 kgm^{-3} to 1027.5 kgm^{-3}, at the position of -48 m to -33 m, is caused by the temperature contribution. In panel b the patterns of three density profiles are similar, thus it is hard to identify the contribution to density coming from each parameter. The dominant patterns of combined contributed density profile in panel a and b are all coincident with the patterns of the temperature profile where only density contributes.

On 8th September (day 243), when the CTD was deployed from the ship, the stratification at the NNS site is well established: the density profile shows a major two layer structure along the entire water column with a detailed structure of three layers at the surface mixed layer. The variation of the water density profile (red line) shows its major pattern coincident with the density profile where only the temperature (blue line) contributes, while its detailed structure above 85 m, shows a similar pattern of variation with the salinity profile (green line) where only the density contributes.

During the second cruise on the 2nd November (day 306), the water column clearly shows a two layer structure with a 3 m thick thermocline (fig 5.5 panel b). The density difference of the surface and the lower mixed layer decreased from about 1.1 kgm^{-3} (September) to 0.6 kgm^{-3} (November). In fig 5.5 panel b, all three density structure profiles have the similar shape over the water column. For these reasons, it is not clear which factor contributes most to the variation of density according to panel b. Both panels a and b, however, show a clear correlation of variation in the combined contribution to the density profile (red line) with the variation of temperature only influenced by density profile (blue line). For this reason, in the remainder of this chapter, it will be considered satisfactory to use the temperature structure in order to represent the density structure.

Fig 5.6 shows the time evolution of temperature at the NNS site from days 245 to 305 over the entire water column. Over this period the thermocline deepens from -45 m to -33 m. Over the same period of time the entire water column cooled down, the surface mixed layer temperature decreased from 13 ℃ to 9 ℃, and the lower mixed layer temperature, for example at -60 m, decreased about 0.5℃, from 8℃ to about 7.5℃.

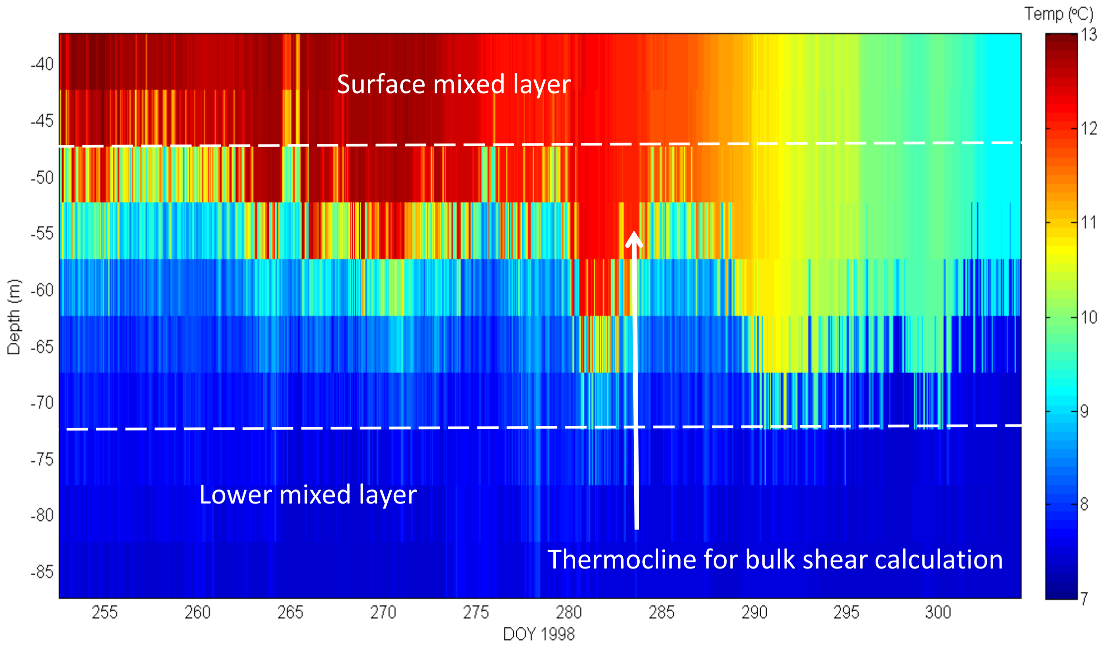

Fig 5.6 The time series profile of the sea temperature at the NNS site. The temperature dominated thermocline deepens along the entire mooring period, the bottom boundary of the thermocline deepens from -47 m (day 260) to -67 m (day 290). In this figure the variation of thermocline is bigger than that in fig 5.4. The surface mixed layer temperature decreases from 13℃ to 9℃, the lower mixed layer temperature, for example at -72 m, decreases of about 0.5℃. For calculation convenience, the thermocline is defined between -72 m to -47 m, which is between the white dashed lines.

Since the thermocline depth varies during the mooring deployment, for the purposes of estimating the bulk shear, we define the thermocline as extending from -72 m to -47 m. The lower mixed layer is set below -72 m depth, and the surface mixed layer is set above -47 m depth.

5.2.2 The wind and tide over the period of the mooring deployment

The moored meteorology data in this chapter is collected from a fixed platform of Frigg Oil Rig which is near the NNS site (detailed information see section 5.1). The evolution of wind is shown in fig 5.7 and the mooring period is during the days 250 - 305. Based on the wind speed, the wind time series can be separate into two stages by day 281. Before day 281, the wind appears as the windy period crossover the quite period. The wind speed of the windy period is above 10 ms^{-1} on days 251, 257 - 263 and 272, and the wind speed of the quilt period is below 10 ms^{-1} (in most time below 5 ms^{-1}) in the other days. During the whole mooring period, no significant storm event occurs, considering that a storm is defined as having a wind speed exceeding 24.5 ms^{-1} by the Beaufort scale.

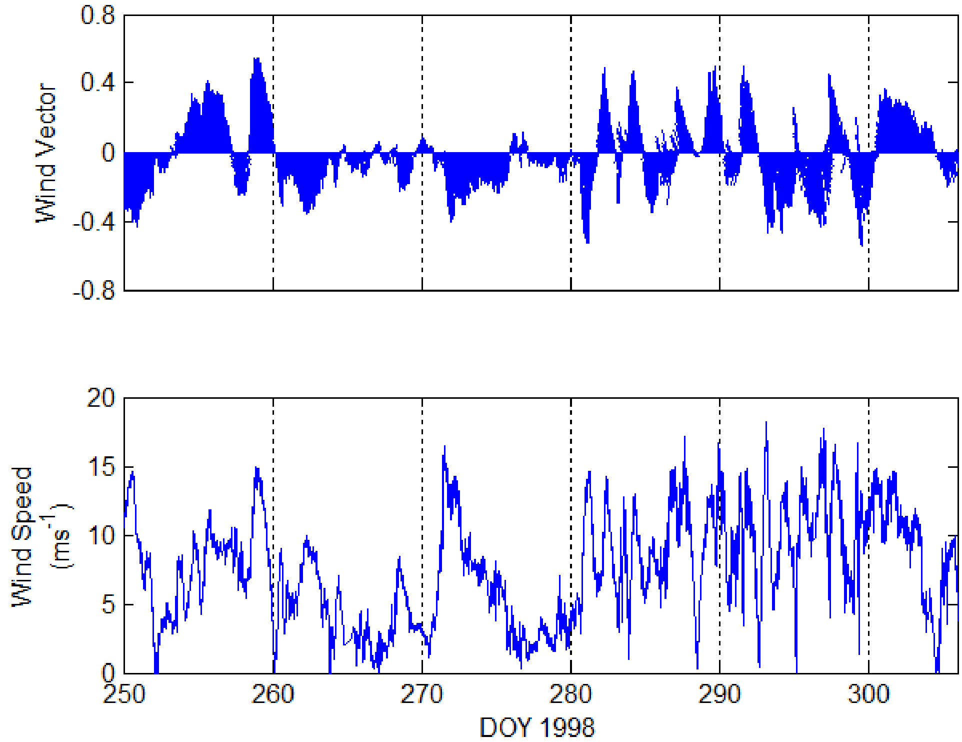

Fig 5.7 a) The meteorology data moored from nearby Frigg Oil Rig (detailed information see section 5.1). The resolution of wind is 20 minutes. b) the time series of wind speed. The wind speeds before day 281 and after have significant difference. Before day 281, the wind speed is below 10 ms^{-1} most of the time, there are three speedy wind events (wind speed about 15 ms^{-1}) occur before day 281 which are days 251, 259 and 272. After day 281, the wind speed is between 10 ms^{-1} to 15 ms^{-1} for most of the time. During the mooring period there is no significant storm events (wind speed exceeding 24.5 ms^{-1}) occurred.

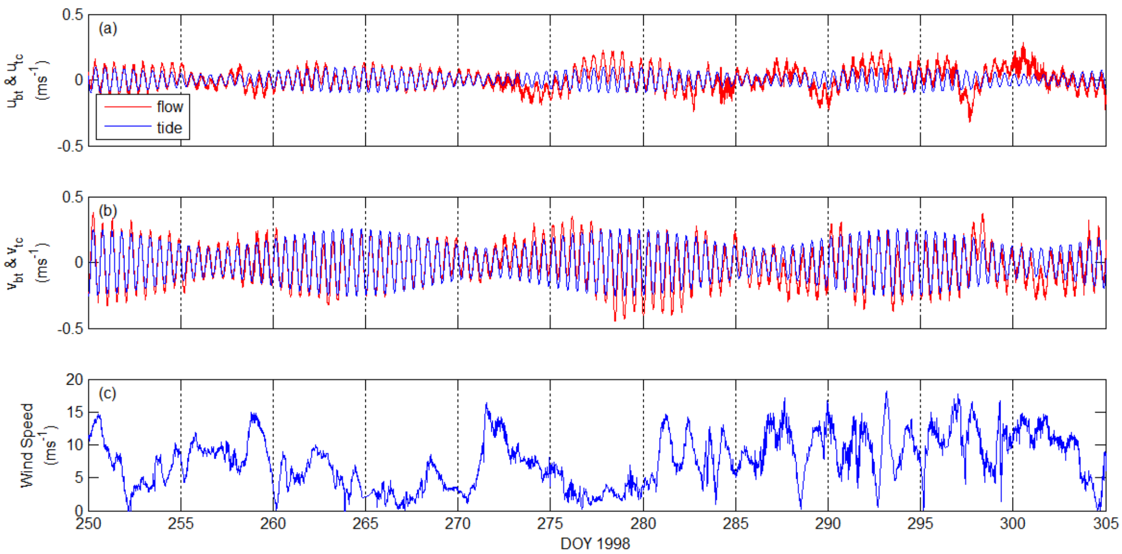

Fig 5.8 the barotropic current velocity (the depth average flow), the barotropic tide (barotropic tidal fitting of depth average flow) and the wind speed. a) The E-W depth average current velocity u_{bt} (red line) and the E-W barotropic tide u_{tc} (blue line). The E-W current velocity is slightly bigger but still comparable with the E-W barotropic tide which is about 0.1 ms^{-1} before day 272, after day 272 the barotropic current velocity divergence with the E-W barotropic tide. The spring-neap cycle is about 15 days with spring tides occurring on days 264, 279 and 194

and the neap tides occurring on days 258, 272, 288 and 303. b) the N-S depth average current velocity v_{bt} (red line) and the N-S barotropic tide v_{tc} (blue line). The N-S current velocity is slightly bigger but still comparable with the N-S barotropic tide and the magnitude is about 0.4 ms^{-1}. The divergence of barotropic current and of the barotropic tide is also conspicuous after day 272. c) wind speed (see fig 5.7). Comparing day 272 through the three panels, it is clear that this is a day in which the mooring site have weakest tide (neap tide, 0.1 ms^{-1}) and strong wind (wind event, i.e. >15 ms^{-1}).

Barotropic current (red lines in fig 5.8 panels a and b) is defined as the depth average flow. To estimate the barotropic tide (blue lines in fig 5.8 panels a and b), the barotropic tidal fitting, or harmonic analysis, which is accomplished using the Matlab routine t_tide.m [Pawlowicz et al., 2001], was applied on the barotropic current with the tide components of M2, S2 and M4. Panel a and b in fig 5.8 show the comparison of the barotropic current and the barotropic tide, which is the tide reconstructed from the tidal analysis, in the E-W and N-S direction respectively.

In fig 5.8 panel a, the E-W barotropic current has a similar velocity intensity compared to that of the E-W barotropic tide, which is of about 0.1 ms^{-1}. The barotropic current can be separated into two parts around day 272. Before day 272 the barotropic current is coincident with the barotropic tide, after day 272, the divergence occurs between the barotropic current and barotropic tide in E-W direction. The divergence appearing in the barotropic tide velocity is represented by a symmetrical wave packet, mirroring above and beneath 0, however the barotropic current velocity wave packet is not mirrored and the amplitude (0.25 ms^{-1} - 0.3 ms^{-1}) sometimes can be twice to three times larger than the amplitude of barotropic tide (0.1 ms^{-1}).

In fig 5.8 panel b, the velocity of the N-S barotropic current is comparable with the barotropic tide, which varies from 0.1 - 0.25 ms^{-1}. The same divergence observed in the E-W currents after day 272 is also observed in the N-S currents. The velocity divergence after day 272, during which the amplitude of the barotropic current (0.4 ms^{-1}) is larger than the amplitude of the barotropic tide (0.25 ms^{-1}), implies the involvement of some additional force. It is worth noting that the divergence was coincident with the wind velocity increasing on and after day 272, as shown in panel c, thus suggesting that the wind could be a strong candidate driving the divergence.

The spring tide occurs on days 264, 279 and 294 and the neap tides occur on days 258, 272, 288 and 303. The spring tide in the E-W direction is 0.1 ms^{-1}, and the neap tide is

0.05 ms^{-1}. For N-S direction, the spring tide is 0.25 ms^{-1} and the neap tide is 0.1 ms^{-1}, in which case the barotropic tide N-S vector is stronger than the E-W vector.

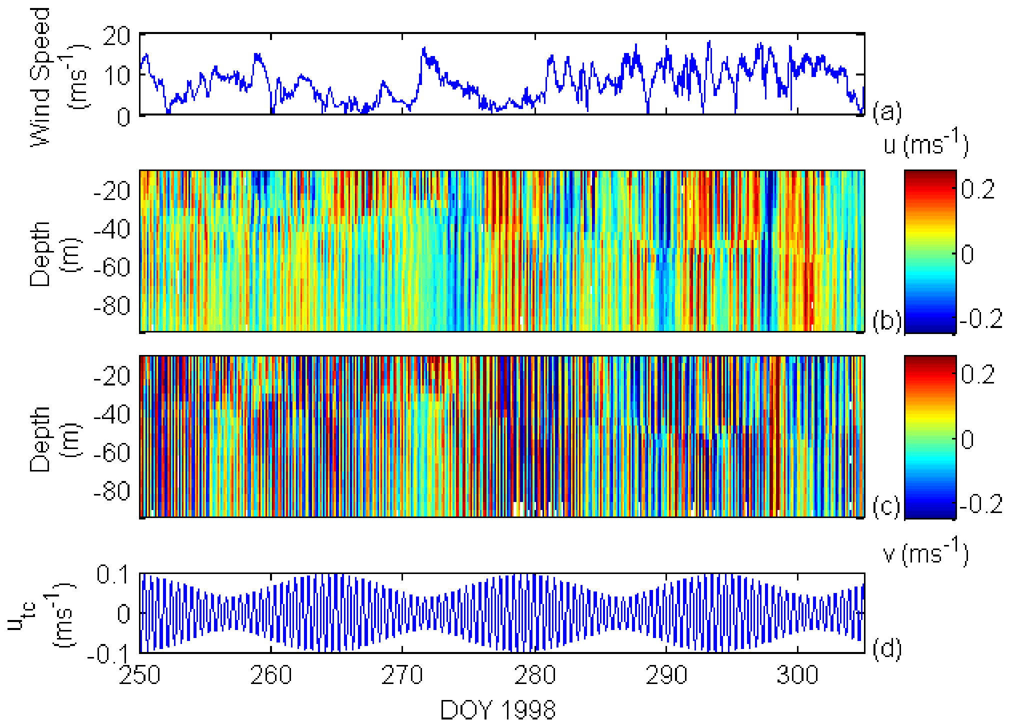

Fig 5.9 The time series of wind speed (panel a), current velocity profiles in the E-W (panel b) and N-S (panel c) direction and barotropic tide (panel d). Panel a is the wind speed (see fig 5.7), panel b is the profile of the current velocity u in the E-W direction, panel c is the profile of the current velocity v in the N-S direction and panel d is the barotropic tide in the E-W direction (see fig 5.8) to illustrate the timing of spring-neap cycle. Panel b shows several significant E-W direction current enhancements during the mooring period in the surface mixed layer and at the lower mixed layer. The current enhancement at the surface mixed layer is on days 260, 264 - 269, 277 - 280 and 290 - 303 and that at the lower mixed layer on days 273 - 281 and 288 - 303. The lower boundary of surface mixed layer current velocities enhancement varies during the mooring period, which is about -40 m from days 273 to 275, and is -50 m from days 288 to 303. In panel c the N-S direction current enhancement is most of the time not very obvious when compared with panel b, due to the strong intensity of the water column velocity in the N-S direction, but during days 297 - 298 a significant current velocity occurs throughout the water column. On days 259, 272 and 301, the water current velocity enhancements coincide with the wind peaks and tide neaps.

Fig 5.9 shows the wind speed (panel a), the current velocity profiles u, in E-W direction (panel b), and v in N-S direction (panel c) and finally the barotropic tidal flow u_{tc} in the E-W direction (panel d).

In panel b, before day 272, the current velocity enhancement occurs in the surface mixed layer from -40 m to the sea surface, but this enhancement is not evident in lower mixed layer, for example on days 260 and 264 - 269. After day 272, the current velocity enhancement is evident in both the surface mixed layer and the lower mixed layer. For example, the enhancement appears limited to the surface mixed layer on days 264 - 269, whist it appears to impact on the whole water column on days 277 - 278 and 292 - 294. Moreover, the enhancement is only evident in the lower mixed layer on days 287 - 288.

The enhancement of the current velocity appears with more frequency considering the N-S current velocity vector (Panel c) than considering the E-W current velocity vector (panel b), for example on days 274 - 283. The clearer enhancement signal appears where the tidal component flow is weaker.

Over most of the observational period, there does not appear to be any coincidence between the wind (panel a), barotropic tide (panel d) and water current velocity enhancement, however on days 259, 272 and 301, when strong winds coincide with neap tides, the water current velocity enhancements occur.

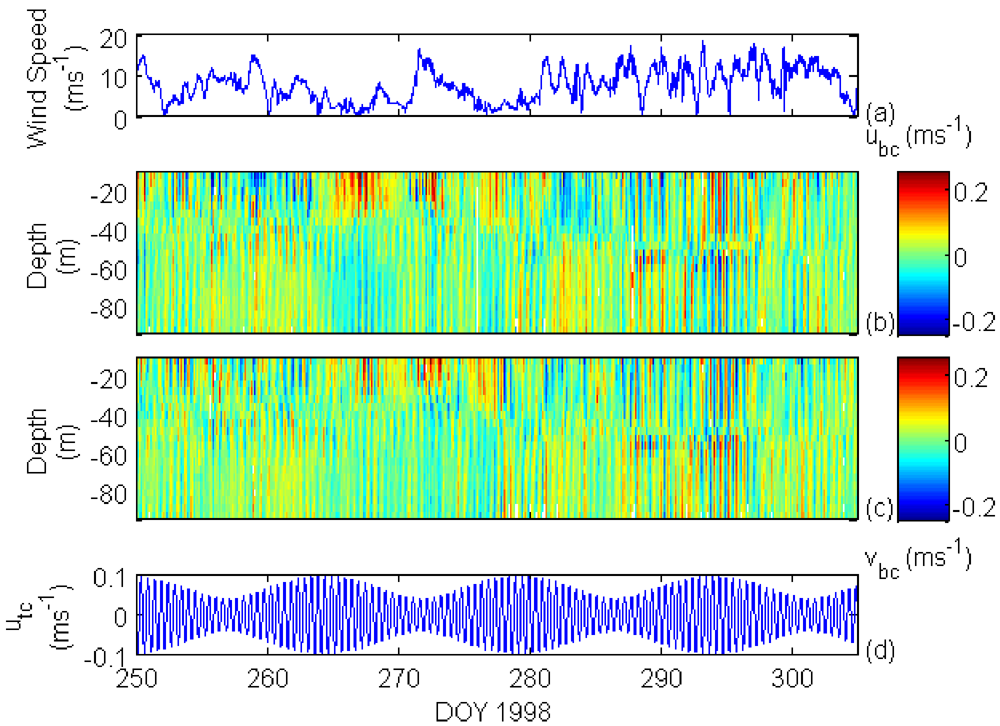

Fig 5.10 The time series of wind speed (panel a), the baroclinic current velocity (subtracting the depth mean flow from the raw current velocity data) profiles at E-W (panel b) and N-S (panel c) direction and the barotropic tide (panel d). Panel a is the wind speed (see fig 5.7), panel b is the profile of baroclinic current velocity $\boldsymbol{u_{bc}}$ in the E-W direction, panel c is the profile of baroclinic current velocity $\boldsymbol{v_{bc}}$ in the N-S direction and panel d is the barotropic tide in the E-W direction (see fig 5.8) which is used to present the spring-neap cycle of barotropic tide. For this reason it is not necessary to present the barotropic tide component at N-S direction in this figure. The magnitudes of baroclinic current in both directions have no significant difference, the baroclinic current velocity in the N-S direction is slightly smaller than that in the E-W direction.

Fig 5.10b and c show the baroclinic current, which is estimated by the depth average current velocity subtracted from the raw current velocity data in the E-W and N-S directions. The ADCP covers almost the whole water column, from -94.5 m to -10.5 m, and thus the baroclinic current profile is not the artefact. The water column is separated into two parts based on the current velocity direction switch, and the depth that separate the two layers varies along time series, but in general it is at the depth of -50 m. Six significant baroclinic current velocity enhancements can be found in panel b during the mooring periods which occur around days 259, 267, 272, 278, 287 and 293. Some of the enhancements are coincident with the strong wind and weak tide condition for example days 259 and 272, some with weak wind and strong tide condition, for example days 267 and 278, and some enhancements occur when both the wind and tide are strong. Thus there is no single standard explanation that could cover all the correlations of baroclinic current variation with wind and tide based on the time series of panels a, b and d. In panel c, the enhanced baroclinic current velocities also appears, and occurs at almost the same period as in panel b, the most significant enhancement occurs on days 267, 272 and 278. The intensity of the E-W baroclinic current is slightly bigger than in the N-S direction components. More detailed current structure is shown in fig 5.11.

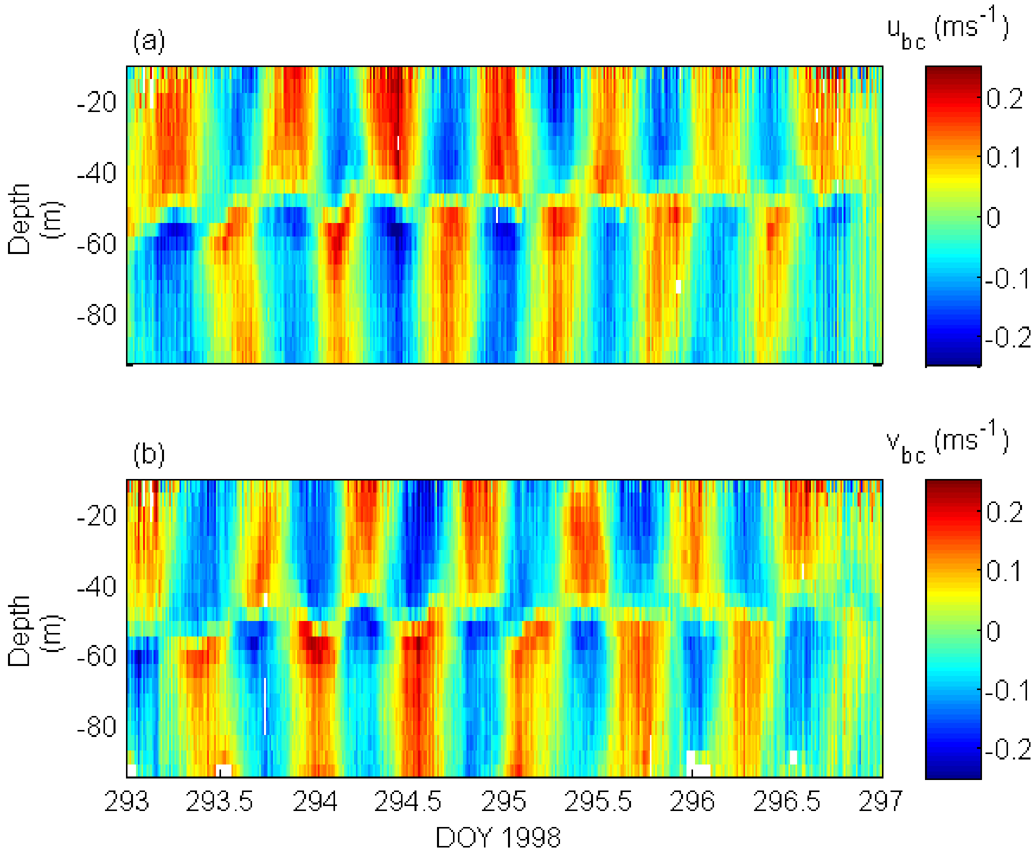

Fig 5.11 A four-day time series showing the baroclinic currents at the mooring site derived from removing the depth mean flow from the ADCP velocity profiles. Notice a 180° phase lag between surface mixed layer and lower mixed layer in baroclinic current of E-W (a) and N-S (b) directions. This plot is extracted from fig 5.10. Both current velocity components reveal the phase lag between the surface and lower mixed layers. Also in panels a and b, the currents flow rotate anti-cyclonic at surface mixed layer and bottom mixed layer (figs 5.12 & 5.13). The

oscillation period is of 14.95 hours.

The intensity of baroclinic current velocities at the lower mixed layer are comparable with those at the related surface mixed layer but with a significant 180 ° of phase lag. This shows the correlation of baroclinic current velocity variances of surface mixed layer and lower mixed layer, which is obvious especially on days 287 - 298 in fig 5.10.

In the entire water column the baroclinic current rotates (see fig 5.12 and 5.13) with a near 14.95 hours period. The baroclinic current directions can be estimated according to both panels by combining the E-W direction and N-S direction current velocity at the same time and same depth. Baroclinic currents at two heights are chosen as examples to represent the movement of baroclinic currents in the surface and the lower mixed layer. The ‘surface mixed layer example height’ is -22.5 m, the ‘bottom mixed layer example height’ is -86.5 m. Figs 5.12 - 5.13 are the progressive vector plot on days 293 - 297, the baroclinic current of the surface mixed layer and lower mixed layer all rotate anti-cyclonic.

The rotary spectral analysis was applied on the baroclinic current velocity for both surface and lower mixed layer as shown in figs 5.14 and 5.15. The rotary spectrums show that the baroclinic current frequency constituents are concentrated at the inertial frequency and the M2 tidal frequency. At the lower mixed layer, the first dominant frequency is the M2 tidal frequency and the second dominant frequency is the inertial frequency. However at the surface mixed layer, the first dominant frequency is the inertial frequency and the second dominant frequency is the M2 tidal frequency. This suggests that the baroclinic current at the NNS mooring site is related to M2 tide near the sea bottom and is more affected by the wind at the sea surface.

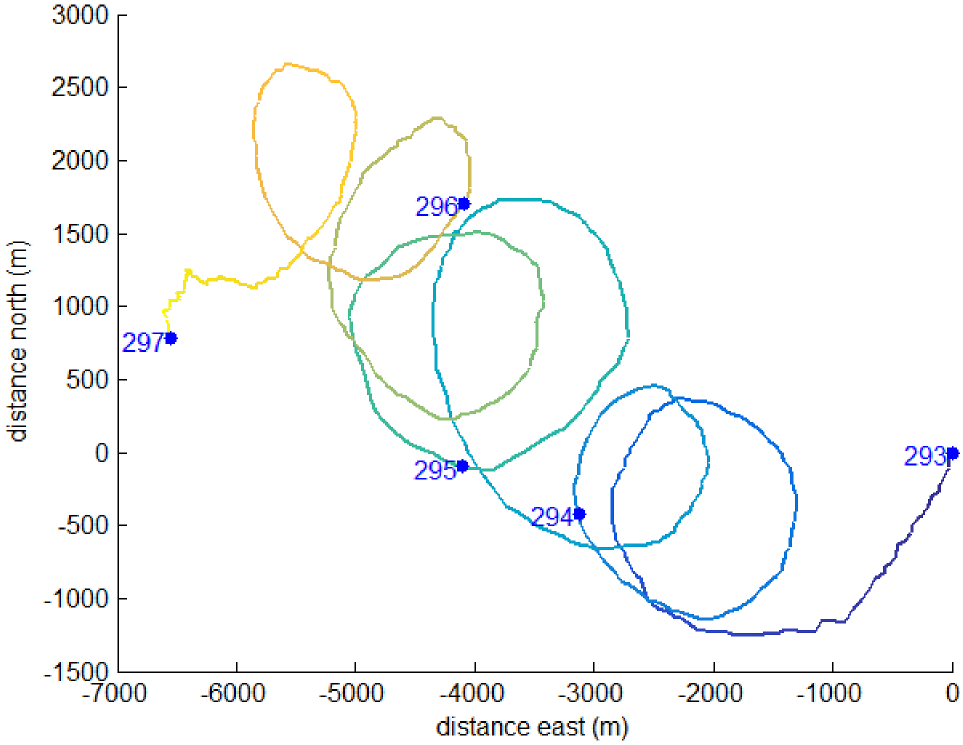

Fig 5.12 The baroclinic current directions can be estimated by combining the E-W direction and the N-S direction current velocity at the same time and at the same depth, which is taken from fig 5.11. The lower mixed layer (example of baroclinic current velocity at -86.5 m) progressive vector plot shows that the baroclinic current rotate anti-cyclonic on days 293 - 297. The lower mixed layer water current flows North West ward with an anti-cyclonic rotation, the gradient color shows the trace of the water parcel movement. The movement starts from the purple color which represents day 293 and ends on day 297, the color of which is yellow.

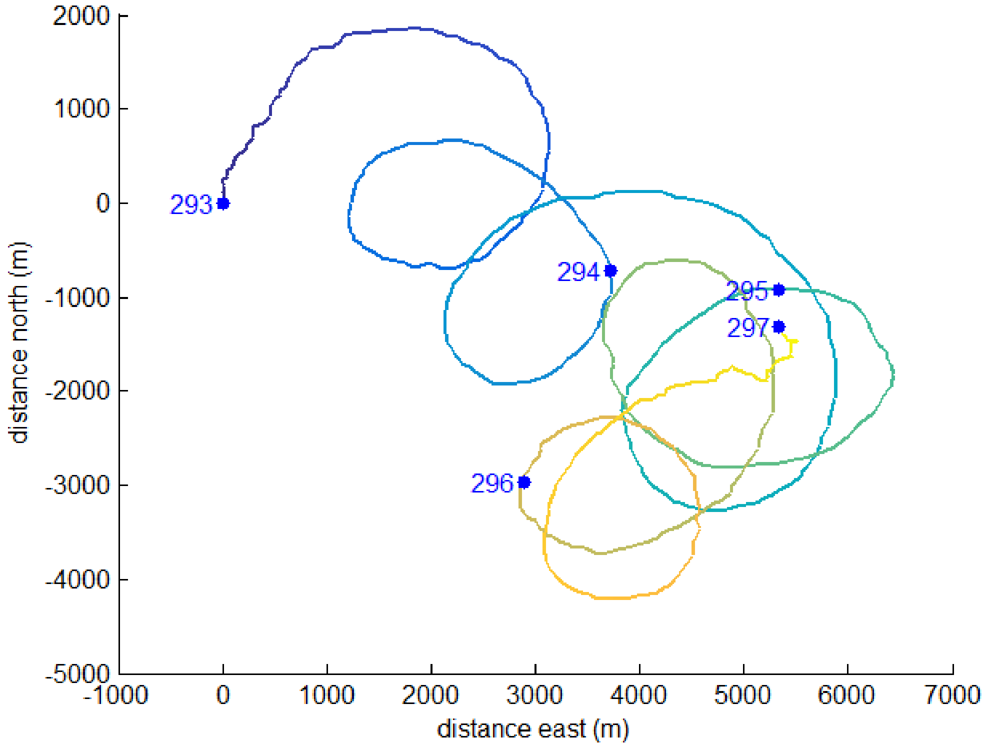

Fig 5.13 Surface mixed layer (the example baroclinic current velocity at -22.5 m) progressive vector plot showing the baroclinic current motion of anti-cyclonic rotation on days 293 - 297. The surface mixed layer current flows South East ward with an anti-cyclonic rotation. The gradient

color shows the trace of the water parcel movement. The movement starts from the purple color which represents day 293 and ends on day 297 the color of which is yellow.

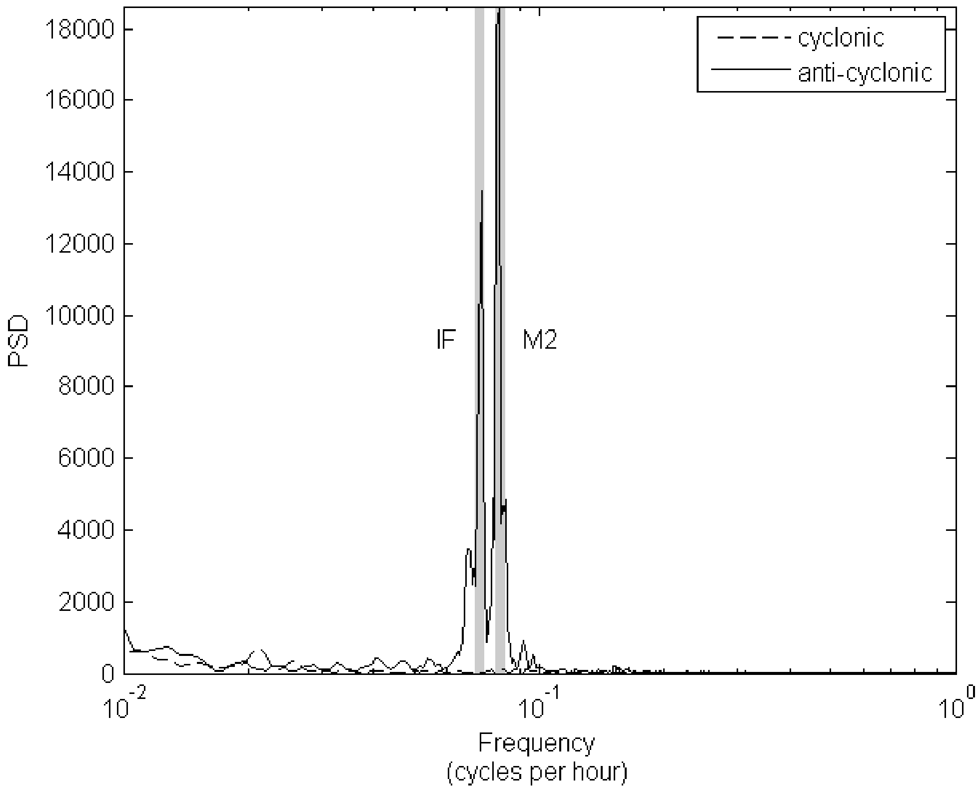

Fig 5.14 Rotary spectral analysis of the baroclinic current of lower mixed layer. The solid line is the anti-cyclonic constituent and the dashed line is the cyclonic constituent. The grey bar indicates the position of local inertial frequency (IF, 0.0719 cycles per hour at NNS site, period 13.9 hour) and M2 tidal frequency (M2, 0.0805 cycles per hour at NNS site, period 12.4 hour). The anti-cyclonic rotation is the dominant rotation compare with the cyclonic rotation, the first dominant frequency concentrated at the local M2 tidal frequency and the second dominant frequency concentrated at inertial frequency.

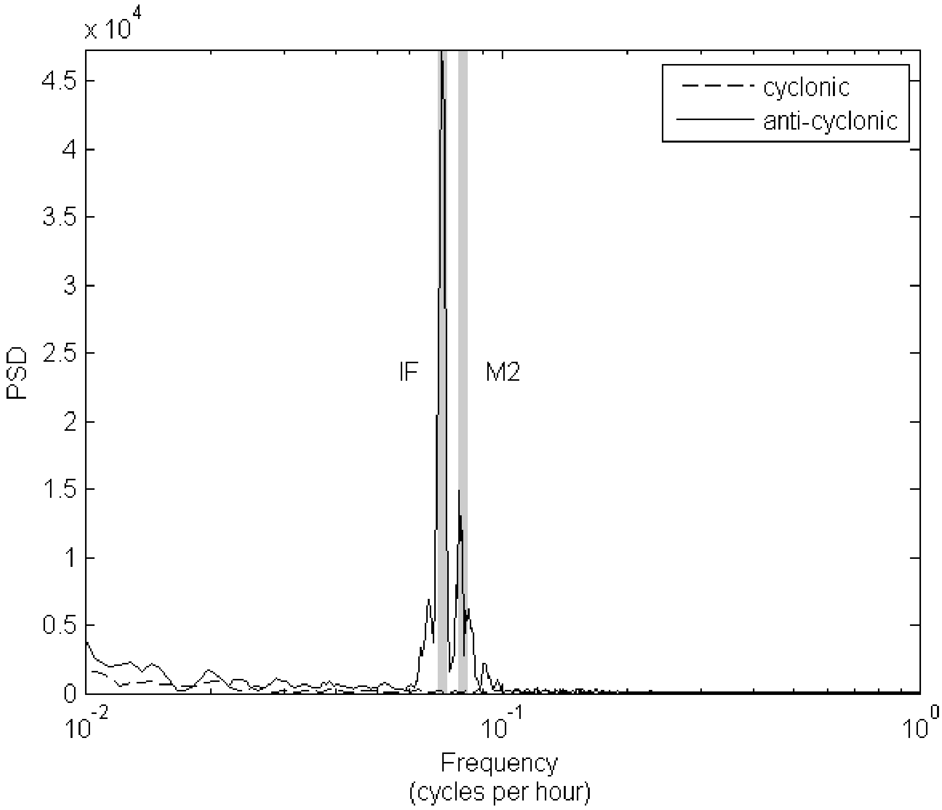

Fig 5.15 Rotary spectral analysis of the baroclinic current of surface mixed layer. The solid line is the anti-cyclonic constituent and the dashed line is the cyclonic constituent. The grey bar indicates the position of local inertial frequency (IF, 0.0719 cycles per hour at NNS site, period 13.9 hour) and M2 tidal frequency (M2, 0.0805 cycles per hour at NNS site, period 12.4 hour). The anti-cyclonic rotation is the dominant rotation compare with the cyclonic rotation, the first dominant frequency concentrated at the local inertial frequency and the second dominant frequency concentrated at M2 tidal frequency.

In brief, the observations reveal:

1. In NNS site, both the variation of temperature and the variation of salinity contribute to the variation of density. The evolution of temperature was chosen to represent the evolution of density due to the availability of long term continuous temperatures time series throughout water column.

2. The water column structure evolves from fully developed stratification toward a complete breakdown. The difference of temperature over thermocline falls from 4.8℃ in September to 1.4℃ in November. The thermocline also deepens along this observational period from -33 m in September to -45 m in November, and at the same time the thickness of the thermocline decreases from 13 m to 3 m.

3. The temperature of the whole water column slowly decreased during the observational period and the temperature variation of the surface mixed layer (3.7°C) over time is much larger than that of lower mixed layer (0.3°C).

4. During the observational period, there is some evidence of the observed current velocity enhancements coincident with periods of enhanced wind and neap tide, and of some oscillating current velocity enhancement coincident with the weak wind and spring tide. However, there is no clear correlation of the observed current velocity response to variations in wind and tide.

5. Before day 272 the barotropic current velocity is coincident with the barotropic tide velocity but after day 272 a divergence occurs.

6. The observed surface current velocity enhancement is reflected by an observed current velocity enhancement in the lower mixed layer but with a 180 ° phase lag.

5.3 Observation data analysis

5.3.1 Estimate of bulk shear

As stated in Chapter 4, the estimate of bulk shear in the NNS case is challenging because of the thermocline depth changes during the cruise of the measurements. The bulk shear is estimated using the equation $S_{bk} = \frac{\overline{U_s} - \overline{U_b}}{h_{diff}}$ as described Chapter 2, where S_{bk} is the bulk shear, $\overline{U_s}$ is the mean velocity of surface mixed layer, $\overline{U_b}$ is the mean velocity of lower mixed layer and h_{diff} is the height difference between the centers of the two layers. The shear direction follows the direction of the surface mixed layer current velocity. In the calculation for the NNS, the surface mixed layer is defined as -52 m to sea surface (fig 5.6), which covers 11 ADCP bins (ADCP bin is 4 m interval), and the lower mixed layer is defined as bottom to -57 m, which covers 9 ADCP bins.

Fig 5.16 shows a time series of the evolution of the bulk shear squared. Several periods of distinct shear squared spikes are evident over the observational period, with the most significant shear spikes on days 288 - 296. Shear spikes are also observed on days 267 - 268, 277 - 284 and 299 - 301. The bulk shear squared spike intensities range from 1.8×10^{-5} s^{-2} to 4.1×10^{-5} s^{-2}, which is 3 to 8 times larger than the normal bulk shear squared, which has an average value of about 0.5×10^{-4} s^{-2}. Since the bulk shear squared spikes represent a large increase in shear, as seen in section 4.3.1, they have the potential to generate shear instability.

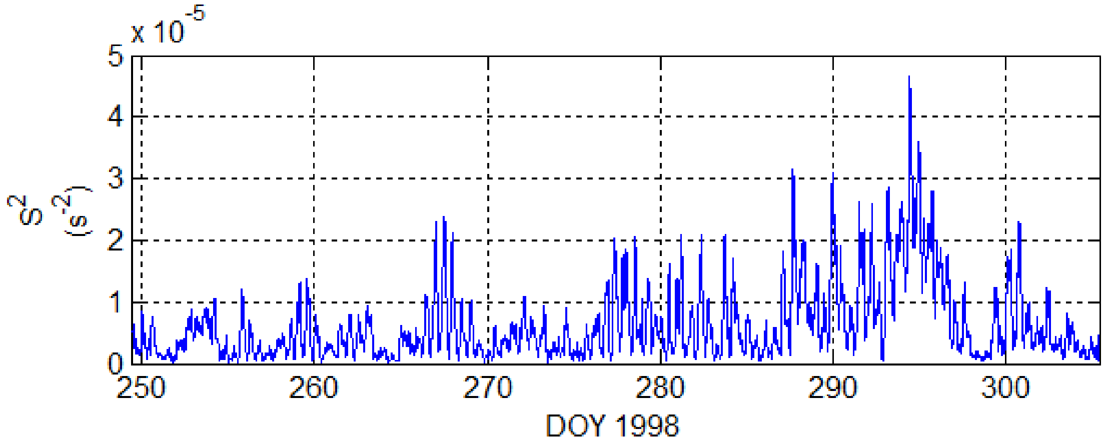

Fig 5.16 A time series of the bulk shear squared over the observational period. The bulk shear squared represents the intensity of the bulk shear, which is estimated from the observed mean current velocity difference of surface mixed layer and lower mixed layer over the distance between the two layer centers at NNS site. Three levels of bulk shear are defined as: below 1×10^{-5} s^{-2}, 1×10^{-5} s^{-2} to 2×10^{-5} s^{-2} and over 2×10^{-5} s^{-2}. The bulk shear squared spike includes the second and the third level. There are four periods of bulk shear squared during the mooring periods, which are on days 267 - 268, 277 - 284, 288 - 296 and 299 - 301. The maximum value obtained for the bulk shear squared is 4.5×10^{-5} s^{-2} at day 294.

5.3.2 Characteristics of the bulk shear

Rotary spectral analysis is used to further investigate the nature of the shear by identifying the distribution of bulk shear across the frequency domain.

The rotary spectrum of the bulk shear during the period of observations at the NNS site is shown in fig 5.17. The solid line is the anti-cyclonic component of the bulk shear and dashed line is the cyclonic component, whilst the grey bars indicate the local inertial frequency (The local inertial frequency at NNS site is 0.0719 cycles per hour) and M2 tidal frequency (0.0805 cycles per hour). Fig 5.17 reveals that the bulk shear during the observational period is strongly associated with the inertial wave band, which according to section 4.3.2 is correlated to the wind, but there is also a significant signal in the M2 wave band, associated with the M2 tide. The bulk shear is dominated by anti-cyclonic rotation with negligible cyclonic movement across the whole frequency range.

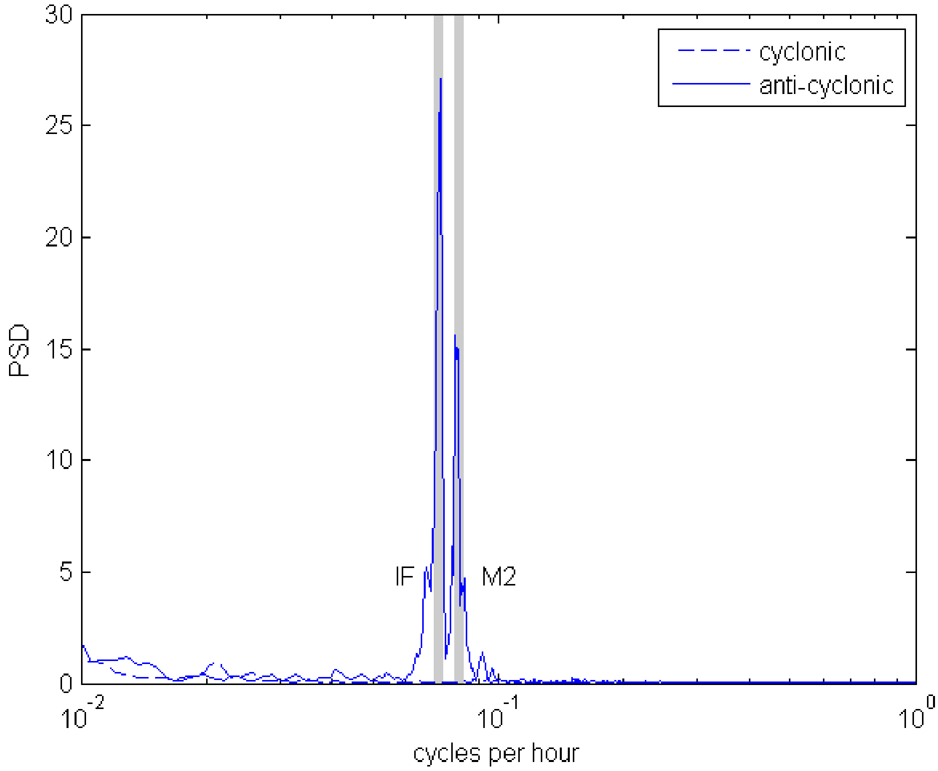

Fig 5.17 Rotary spectral analysis of the bulk shear for the entire observational period. The solid line is the anti-cyclonic constituent and the dashed line is the cyclonic constituent. The grey bar indicates the position of local inertial frequency (IF, 0.0719 cycles per hour at NNS site, period 13.9 hour) and M2 tidal frequency (M2, 0.0805 cycles per hour at NNS site, period 12.4 hour). The anti-cyclonic rotation of the bulk shear is the dominant rotation compare with the cyclonic rotation, the first dominant frequency of bulk shear concentrated at the local inertial frequency and the second dominant frequency of bulk shear concentrated at M2 tidal frequency.

As described in section 5.2.2 the divergence in the barotropic tide compared to the barotropic current appears after day 272, which could mean that the dominant driver of the current may switch after day 272. To try and look for evidence of a switch in forcing, two periods of bulk shear were selected for separate rotary spectral analysis. One is days 250 to 272 (fig 5.18) and the other is day 272 to 305 (fig 5.19). It is obvious from figs 5.18 and 5.19 that during both periods, two peaks located at inertial frequency and M2 tidal frequency, which, as described in Chapter 4, implies that there is energy concentrated in both the inertial and M2 frequency and further indicates that the bulk shear is driven by the wind and tide. The difference between figs 5.18 and 5.19 is the relative contribution from wind and tide to the bulk shear. In period days 272 - 305, the contribution from wind to the bulk shear is bigger than that from tide (fig 5.19). This is considered related to the average value of wind speed during this period being bigger than another period.

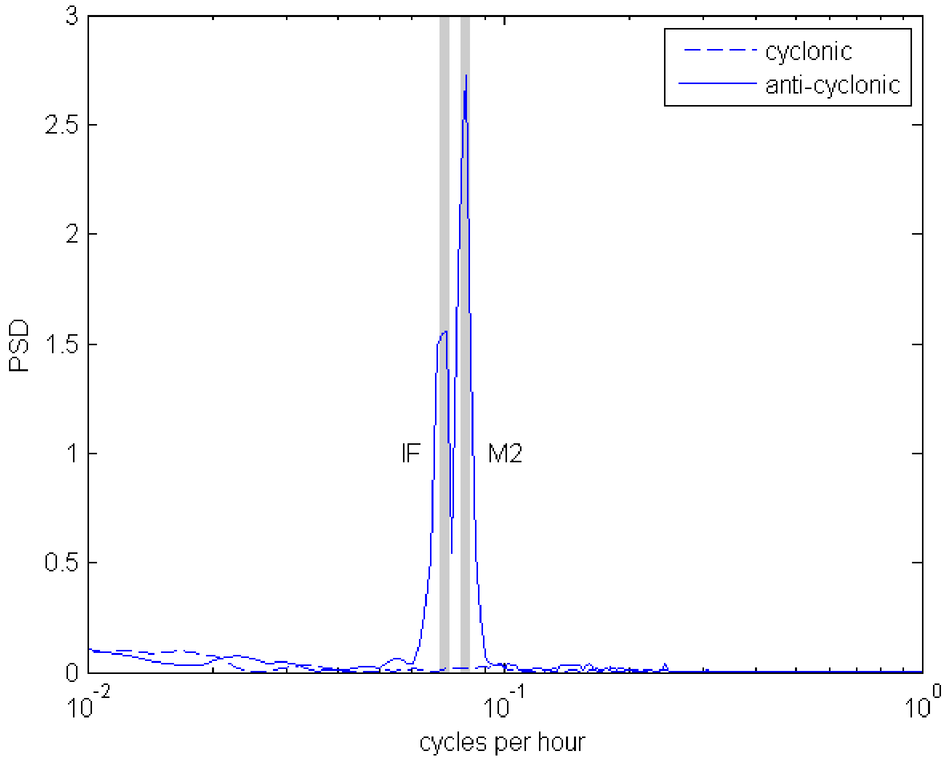

Fig 5.18 Rotary spectral analysis of bulk shear for days 250 - 272. The solid line is the anti-cyclonic constituent and the dashed line is the cyclonic constituent. The grey bar indicates the position of local inertial frequency (IF, 0.0719 cycles per hour at NNS site) and M2 tidal frequency (M2, 0.0805 cycles per hour). The anti-cyclonic rotation of the bulk shear dominants compare with the cyclonic rotation. The greatest peak at M2 tidal frequency indicate the first dominant frequency of the bulk shear concentrated at the M2 tidal frequency and the lower peak at inertial frequency indicate the second dominant frequency of the bulk shear concentrated at local inertial frequency.

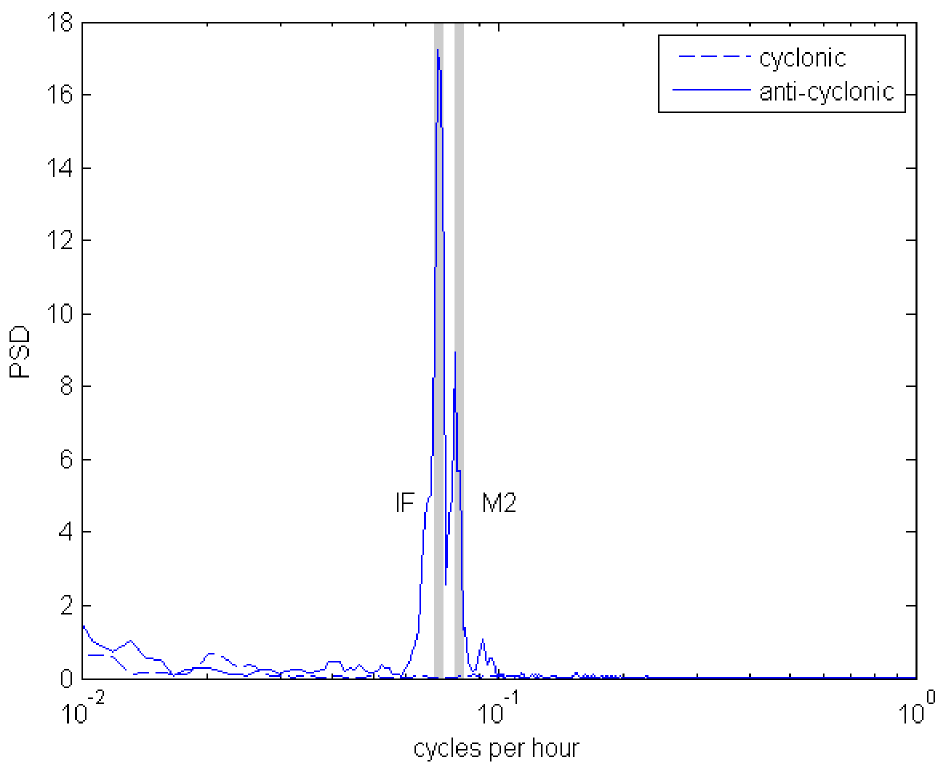

Fig 5.19 Rotary spectral analysis of bulk shear on days 272 - 305. The solid line is the anti-cyclonic constituent and the dashed line is the cyclonic constituent. The grey bar indicates the position of local inertial frequency (IF, 0.0719 cycles per hour at NNS site) and M2 tidal frequency (M2, 0.0805 cycles per hour). The anti-cyclonic rotation of the bulk shear dominants compare with the cyclonic rotation. The greatest peak at inertial frequency indicates the first dominant frequency of the bulk shear concentrated at the local inertial frequency. And the lower peak at M2 tidal frequency indicates the second dominant frequency of the bulk shear concentrated at M2 tidal frequency.

5.3.3 Bulk shear with wind and tide speed

As shown in section 5.3.2, the bulk shear spectrum is dominated by both the inertial frequency and M2 tidal frequency. To further investigate the relationship between shear, wind and tide, the role of each parameter in producing bulk shear must be identified.

Fig 5.20 shows the time series of wind speed (panel a), shear squared (panel b) and barotropic tide E-W vector (panel c). The time series of the barotropic tide in panel c represents the cycle of spring and neap tide. Comparing panel a and b in fig 5.20, the windy period does not appear to be correlated to enhanced shear. The comparison of panel b and c shows that the spring and neap tide does not appear to be simply correlated to the shear, except for days 290 - 300, a period in which the wind is intense as well. These results thus suggest that strong winds coincident with a spring tide may lead to shear spikes.

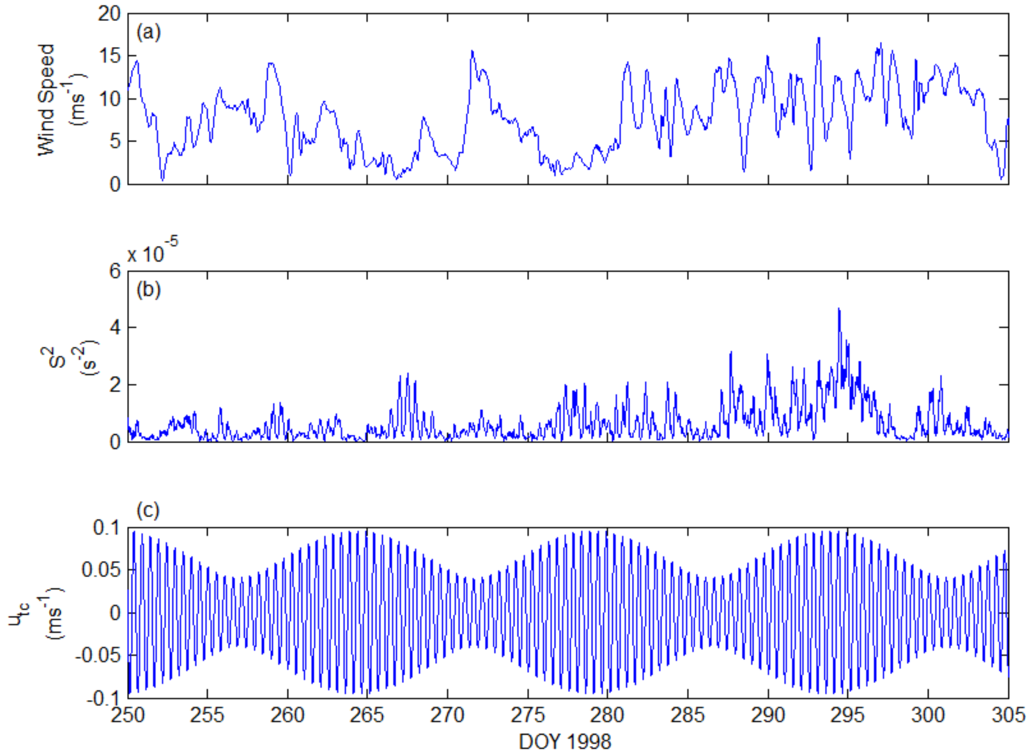

Fig 5.20 The relationship of wind speed, bulk shear squared and barotropic tide in the E-W direction. a) The time series of wind speed (see fig 5.7); b) the bulk shear squared estimated from ADCP observation of the NNS site (see fig 5.16); c) the barotropic tide in the E-W direction (see fig 5.8).The bulk shear squared variation does not clearly coincide with the variation of wind speed or the spring-neap cycle of barotropic tide. However during days 290 - 300, when the strong wind is coincident with the spring tide, the bulk shear square spikes occur. On day 295, the maximum bulk shear square occurs, which is 4.5×10^{-5} s^{-2}.

5.3.4 Bulk shear with wind and tide direction (days 288 - 298)

Fig 5.21 is the comparison among the bulk shear squared, the wind, the barotropic tide and the bulk shear vector directions, and the time evolution of the bulk shear squared during period of days 288 - 298. This period was chosen because the bulk shear spikes are most significant. Panel a is the time series of the bulk shear squared, panel b reveals the angle between the wind vector (red dotted line), the barotropic tide vector (green dotted line) and the bulk shear vector (blue dotted line), and panel c shows the time evolution of the bulk shear squared. Panel b and c reveals that the bulk shear-wind alignment at the NNS site, which is the overlap of red and blue dotted lines, sometimes leads to a $\frac{dS^2}{dt}$ peak (orange dashed line in panel c) but it is not always this case (red dashed line in panel c). The orange dashed lines are the examples of the bulk shear-wind alignments (panel b) creating the peak of the bulk shear's evolution (panel c). And the red dashed lines are the examples of the alignments failing to create the peak. The barotropic tide (green dotted line) aligns with bulk shear (blue dotted line) during days

288 - 291 and 293 - 296, however the alignment of baroclinic tide and of the bulk shear vector does not appear to affect the evolution of the bulk shear squared in the period of days 288 - 298. The peaks of evolution of the bulk shear created by the bulk shear-wind alignment is explained in Chapter 4 as it is the point of maximum energy input to the bulk shear, however the opposite situation is hard to explain and needs further study in the future.

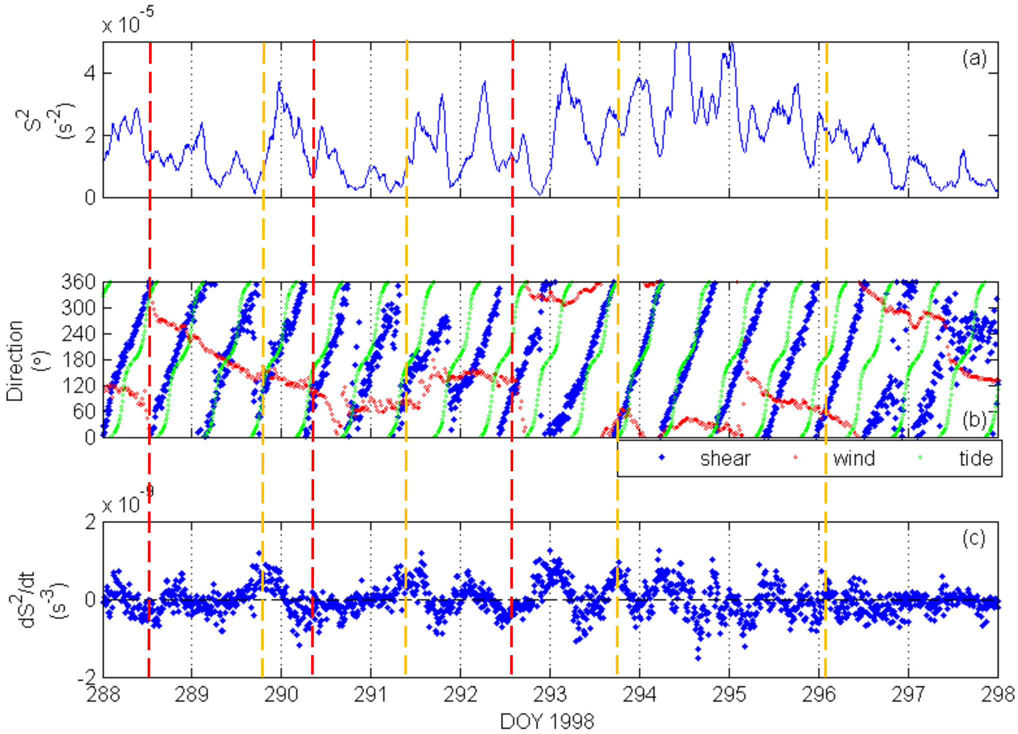

Fig 5.21 Relationship of shear spike, evolution of bulk shear squared, and bulk shear-wind-barotropic tide vector alignment. a) Bulk shear squared (see fig 5.16); b) comparison of the bulk shear direction, the wind direction and the barotropic tide direction: red dotted line is the wind direction, blue dotted line is the bulk shear direction, which rotates anti-cyclonically with a period of 0.6 day, the green dotted line is the barotropic tide, which rotates anti-cyclonically with a period of about 0.5 day; c) blue dotted line is the time evolution of the bulk shear squared from observation. The orange dashed line is the index showing the examples of the time in which the wind and the bulk shear vectors align (on days 289.7, 291.4, 293.8 and 296.1)and are coincident with the peak of the bulk shear squared evolution. The red dash-dotted line is the index showing examples of the time in which the wind and the bulk shear vectors are aligned (on days 288.5, 290.4 and 292.6) and not coincident with the peak of the bulk shear squared evolution.

The relationship between the tide-bulk shear alignment and the evolution of the bulk shear squared has been found in the period of days 260 - 270. Fig 5.22 is the comparison among the bulk shear squared (panel a), the barotropic tide-bulk shear directions (panel b) and the time evolution of the bulk shear squared (panel c) during days 260 - 270. The peaks of the bulk shear evolution appear to be coincident with the barotropic tide-bulk shear alignment, for several times during this period, on days 260.5, 262.5, 263, 266.9, 267.3, 267.9, 268.3 and 268.8, however it is not always the case.

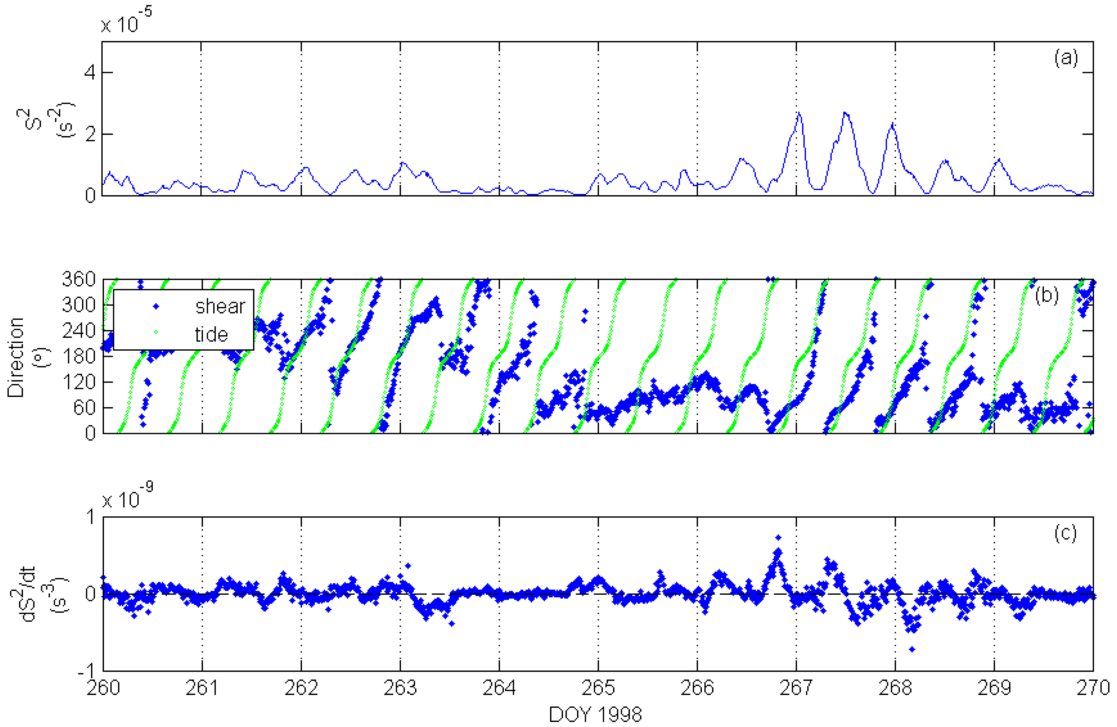

Fig 5.22 Relationship between the shear spike, the bulk shear-barotropic tide vector alignment, and the evolution of the bulk shear squared. a) Bulk shear squared (see fig 5.16); b) comparison between the bulk shear direction and the barotropic tide direction: the green dotted line is the barotropic tide direction which rotates anti-cyclonically with a period of about 0.5 day, the blue dotted line is the bulk shear direction, which rotates anti-cyclonically with a period of 0.6 day; c) the blue dotted line is the time evolution of the bulk shear squared from observation. The orange dashed line is the index showing the wind and the bulk shear vectors alignment (on days 260.5, 262.5, 263, 266.9, 267.3, 267.9, 268.3 and 268.8) coincident with the peak of the bulk shear squared evolution.

5.4 1D Two-Layer Vertical Dynamic Numerical Modelling

Three modelling processes were applied in this section, two of which are the single forced modelling, forced by the wind and tide respectively, and the third model is forced by the combined wind and tide. The two single forced models are for quantifying the bulk shear contribution from wind and tide respectively. And the combined forced model is for testing the ability of the model reproduces the observed shear squared production, which is the evolution of bulk shear square. The predicted shear squared production for each of the three model runs is shown in fig 5.23. The red line is shear squared production from model when the model is forced by both wind and tide. The black line is shear squared production from model with only wind force. The green line is under the scenario that the model is only force by the tide. And the blue dotted line is the time evolution of bulk shear squared $\partial_t S^2$ estimated from the observed water current velocity at NNS.

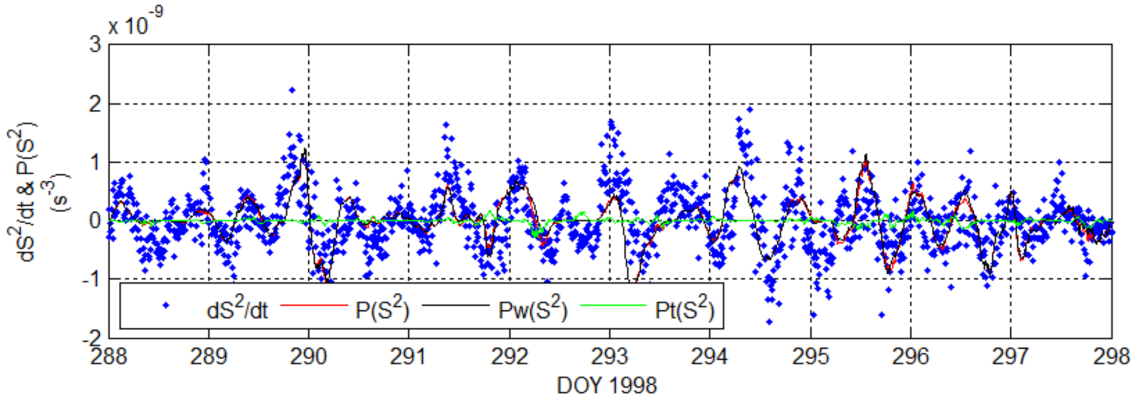

Fig 5.23 Similarity between the bulk shear squared evolution(blue dotted line) and the two-layer modelled shear squared productions (solid lines) (details of two-layer model in Chapter 3). Three separate model runs related to the shear squared production, one is the model runs with only the wind forcing (black line), one is the model runs with only the tide forcing (green line) and the other one is the model runs with both the wind and tide forcing (red line). Correlation analysis (see Chapter 2) has been applied between the evolution of the bulk shear squared from observation (blue dotted line) and each modelled results (solid lines) respectively, for which the r values are 0.39 (blue line and black line), -0.03 (blue line and green line) and 0.39 (blue line and red line).

The correlation indicates that the best agreement with the observed evolution of shear squared is the shear squared production with combined driver (r = 0.39). Poorer fits are obtained when the model is forced by the tide only (r = -0.03).The results from combined forcing are very close to the results obtained from the wind only forcing (r = 0.39).

5.5 Modelled data analysis: correlation and coherence analysis

The coherence analysis and the correlation are carried out to further examine the relationship between the wind velocity and the bulk shear. Detailed information of the analysis can be found in Chapter 2. The period chosen for analysis is days 250 - 305.

Figs 5.24 to 5.27 show the results of the coherence analysis. Fig 5.24 examines the relationship between the bulk shear with bottom stress (dashed line) and the surface stress (solid line). The very low r values (0.06 for bulk shear with bottom stress and 0.25 for bulk shear with surface stress) indicate that there is no clear relationship between bulk shear with the bottom stress and with the surface stress. The coherence spectrum of the bulk shear with the surface stress shows there are two peaks near to inertial frequency and to the M2 tidal frequency respectively. The two peaks, however, have no physical meaning since the surface stress (which estimated from wind speed) does not naturally contain the inertial frequency and the M2 tidal frequency. Thus the peaks do not indicate a relationship between bulk shear and the surface stress at these two frequencies.

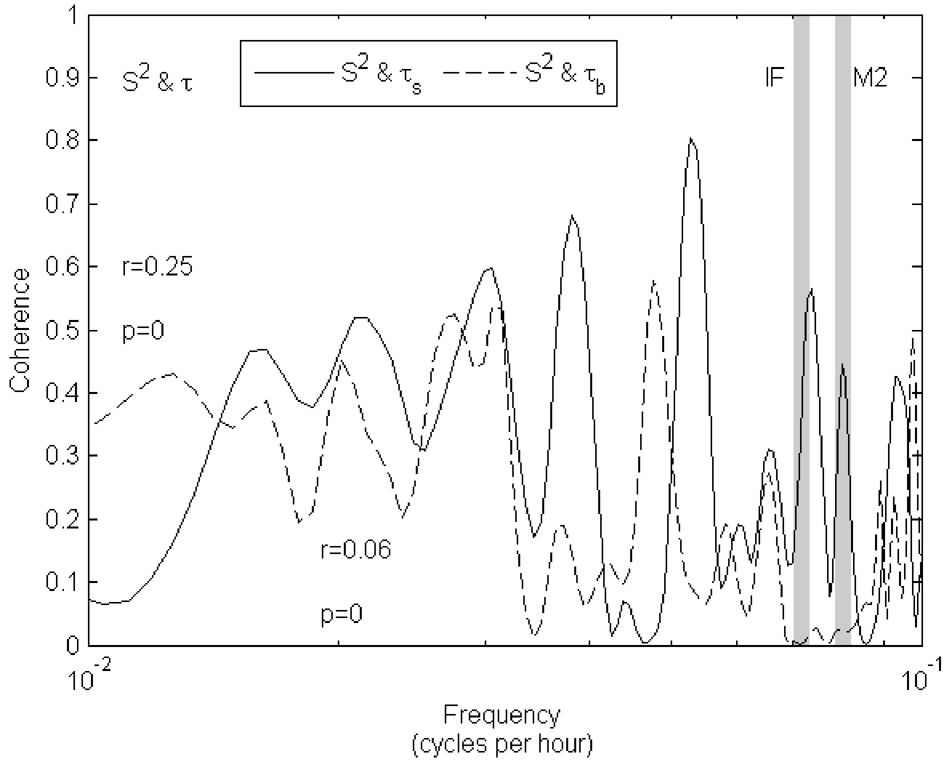

Fig 5.24 Correlation (r and p values) and coherence (dashed and solid lines) analysis of the bulk shear squared and the boundary stresses. Two boundary stresses are involved which are the surface stress and the bottom stress. The solid line is the coherence of the bulk shear squared and the wind stress, the dashed line is the coherence of the bulk shear squared and the bottom stress. The two grey bars show the positions of the local inertial frequency (IF, 0.0719 cycles per hour at NNS site) and of the M2 tidal frequency (0.0805 cycles per hour). The *r* value between the bulk shear squared and the stresses are 0.06 (with bottom stress) and 0.25 (with surface stress), both *p* values between the bulk shear squared and the stresses are less than 0.05. Due to the low *r* value between the bulk shear squared and the bed stress, the boundary stresses are hardly related to the bulk shear squared and thus the coherence between them is less important. The result of the coherence analysis between the bulk shear squared and the surface stress shows two peaks at the inertial frequency and the M2 tidal frequency respectively. However the peaks have no physical meaning since the surface stress does not naturally contain these two frequencies and thus should not have a common frequency with the bulk shear at the inertial frequency and the M2 tidal frequency.

Fig 5.26 is the coherence of shear squared production from the tide only model and the time evolution of the bulk shear squared from observation. The *r* value (*r* = -0.04) is small compare to the *r* value of other two remaining figures: *r* = 0.41 in fig 5.25, which is the correlation of the shear squared production from the model with combined wind and tidal forcing, and the time evolution of the bulk shear squared from observation. And r = 0.41 in fig 5.27, which is the correlation between the shear squared production from wind only model, and the time evolution of bulk shear squared from observation. This further supports the conclusions from section 4.3.2 that the wind is the dominant driver in the production of shear at the NNS site during the observational period (days 250 - 305). The peak at inertial frequency in figs 5.25 and 5.27 leads to a similar conclusion: That the shear square production from model with the combined forcing and the model with the wind only forcing are all related to the observed time evolution of the shear squared, especially at inertial frequency.

Comparing figs 5.25 and 5.27, the correlation coefficient r value is the same in the model with the combined forcing (fig 5.25, r = 0.41) and that with wind only forcing (fig 5.27, r = 0.41). This suggests that the contribution from the tide can be neglect and the dominant driver of the bulk shear in the observational period is the wind.

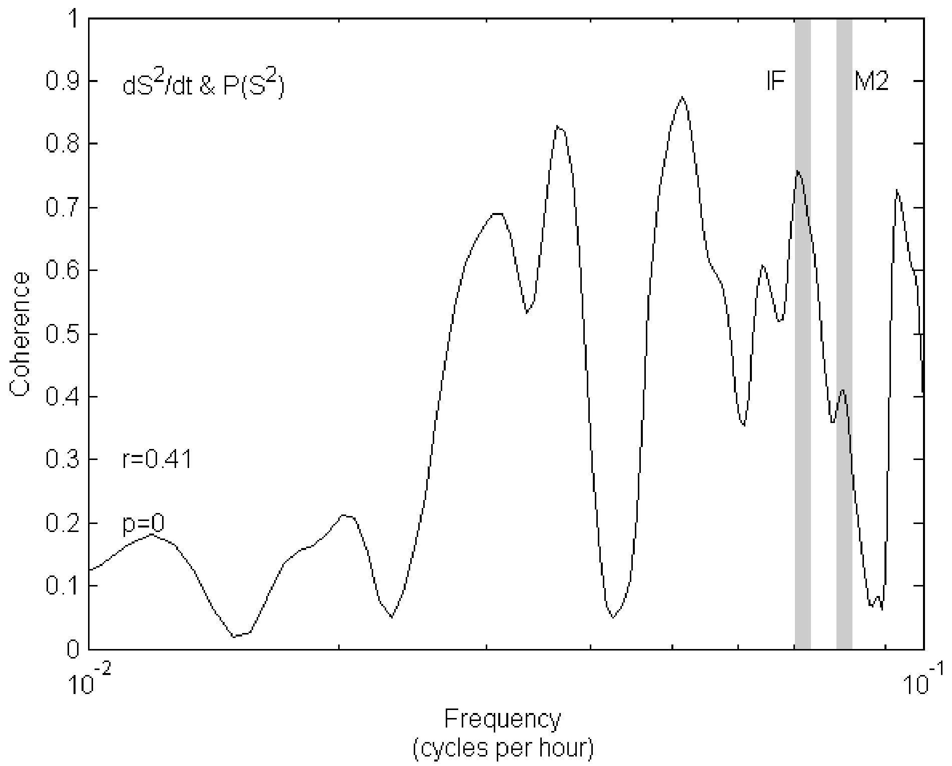

Fig 5.25 Correlation (r and p values) and coherence (solid line) analysis of the evolution of the bulk shear squared, and two-layer modelled shear squared production during the observational period. The two-layer model is driven by the combined wind and tide forcing. The r value 0.41 shows that these two factors are related, and the p value < 0.05. The frequencies concerned in the coherence analysis are the inertial frequency and the M2 tidal frequency. The peaks near inertial frequency indicates a strong similarity near inertial frequency components in the evolution of bulk shear squared and the two-layer modelled shear squared production. The

small peak near the M2 tidal frequency indicates the M2 tide contributes to the shear production but the tidal contribution is small. The greatest peak in this figure is at the frequency of 0.0514 cycles per hour, the appearance of this peak will be explained later.

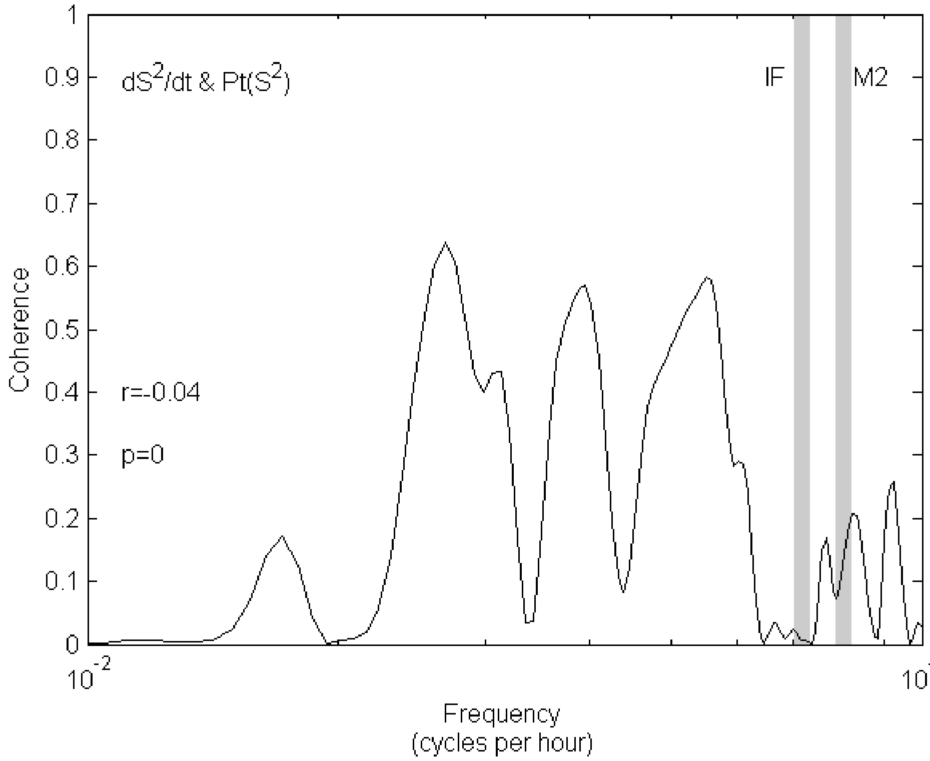

Fig 5.26 Correlation (*r* and *p* values) and coherence (solid line) analysis of the bulk shear squared evolution and of the two-layer modelled shear squared production. The two-layer model is driven by tide only forcing. The low *r* value -0.04 shows that these two factors are hardly related, and the $p < 0.05$. There are no peaks at the inertial frequency or at the M2 tidal frequency where we are concerned, and also because of the weak *r* value, the coherence is considered to be less important.

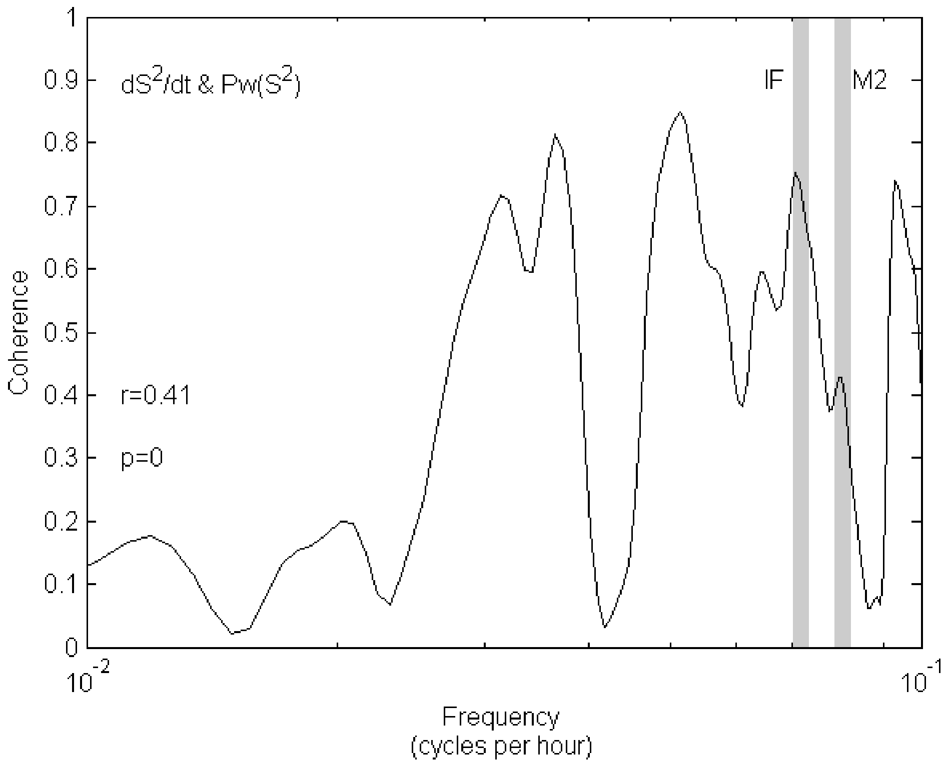

Fig 5.27 Correlation (r and p values) and coherence (solid line) analysis of the bulk shear squared evolution and two-layer modelled shear squared production. The two-layer model is driven by wind only forcing. The *r* value 0.41 shows that these two factors are related, and the *p* < 0.05. There is a peak at the near inertial frequency and a tiny peak near the M2 tidal frequency respectively, which shows that the shear squared production from the wind only driven model have a great similarity with the evolution of bulk shear squared at near inertial frequency. The greatest peak in this figure is at frequency of 0.0514 cycles per hour, the appearance of this peak will be explained later.

The largest peaks, which are found at a frequency of 0.0514 cycles per hour, in figs 5.25 and 5.27 are not expected to appear in the coherence analysis. This implies that the greatest similarity of the evolution of the bulk shear squared estimated from observation, and the shear squared production from two-layer model, is at frequency of 0.0514 cycles per hour, which has no physical meaning. The auto spectrum (take the case of fig 5.25 as example) of the evolution of the bulk shear squared estimated from observation and the auto spectrum shear squared production from the two-layer model were accomplished respectively in fig 5.28 panel a and panel b. This clearly explains the source of the unexpected greatest peak: the magnitude difference of two peaks at near inertial frequency and near the M2 frequency is larger than the magnitude difference at 0.0514 cycles per hour frequency. However, according to the rotary spectral analysis in fig 5.17, most bulk shear energy is concentrated at the inertial frequency and at the M2 frequency. For this reason, Even though the greatest peaks of coherence analysis are at 0.0514 cycles per hour (panel c), it could not be guaranteed as a frequency of the bulk shear driver since the total energy input from this frequency is smaller compare with the energy input from the inertial frequency and the M2 tidal frequency.

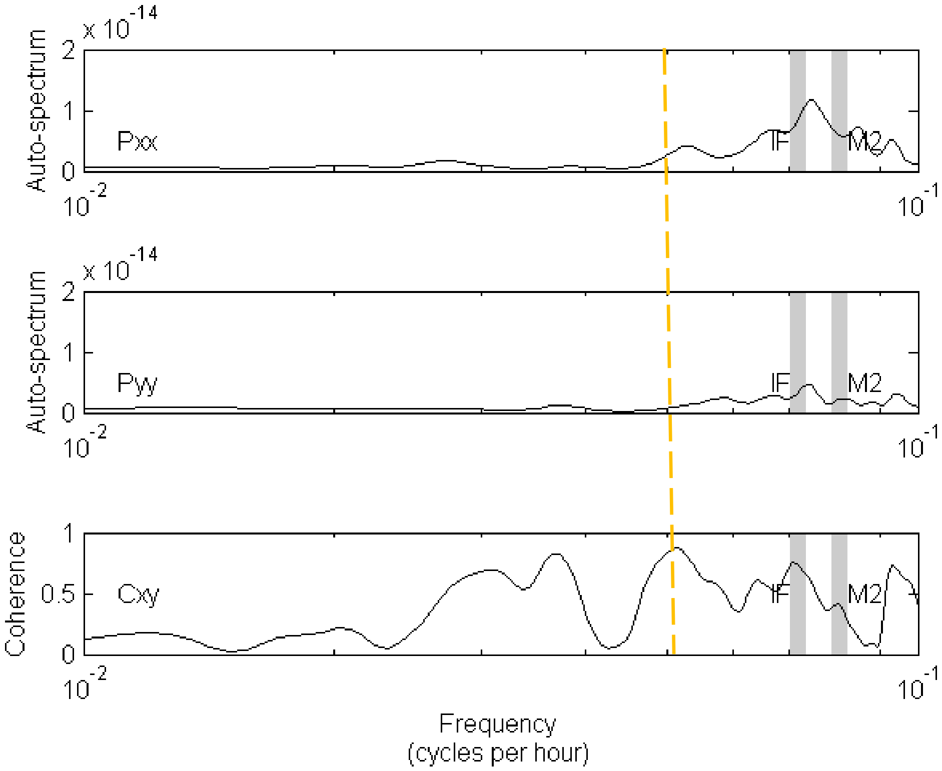

Fig 5.28 Auto spectrum of the bulk shear squared evolution (panel a), auto spectrum of the two-layer modelled shear squared production (panel b), and the coherence analysis (panel c) between the bulk shear squared evolution and the two-layer modelled shear squared production. The grey bars indicate the local inertial frequency (0.0719 cycles per hour at NNS site) and the M2 tidal frequency (0.0805 cycles per hour). The orange dashed line indicates the position of the greatest peak (0.0514 cycles per hour) in the coherence analysis. The source of the greatest peak in coherence analysis in panel c (orange line) can be tracked from the comparison of panel a and panel b, since the similarity of auto spectrum in panels a and b at 0.0514 cycles per hour frequency is bigger than the that at inertial frequency and M2 tidal frequency, thus this similarity is being reflected in panel c, where the coherence at 0.0514 cycles per hour frequency is bigger than that at the inertial frequency and M2 tidal frequency.

5.6 Summary

1. The density profile of the water column is influenced by both variations in salinity and temperature. The temperature profile is chosen to represent the structure of the water column due to the temperature data collected being a time series data, while the salinity data collected is not time series data.

2. The temperature of whole water column was slowly decreased during the observational period. However, the temperature variation of surface mixed layer (3.7℃) is much larger than that of lower mixed layer (0.3℃).

3. During the observational period, some of the enhancements of the currents are coincident with the stormy winds and neap tide, while some of the current velocity enhancements are coincident with the weak wind and spring tide. Thus there does not appear to be a simple rule to correlate the current velocity variation with the variation of wind and tide.

4. Before day 272 the barotropic current velocity is coincident with the barotropic tide, which implies the current oscillations are dominated by the barotropic tide, but after day 272 the barotropic current velocity significant divergence from the barotropic tide.

5. The increase of observed surface current velocity is mirrored by an increase in the lower mixed layer with a 180 °phase lag.

6. In the NNS site the production of shear across the thermocline is dominated by a combination of factors related to the wind and tide. Rotary spectral analysis of the bulk shear for different time period shows that before day 272 the main driver is the tide and after day 272 the dominant driver it is wind.

7. The correlation and coherence analysis between the shear production estimated from the 1D two-layer vertical dynamic numerical model and from observation shows that, both the wind and the barotropic tide contribute to the production of the bulk shear, however the wind appears to be the main driver in comparison to the tide.

Chapter 6

Sensitivity analysis of the impact of varied hydrographic scenarios to shear

The previous two chapters presented observations of the evolution of shear across the thermocline in response to the wind and barotropic tide from the western Irish Sea, during the development of seasonal stratification, and from the northern North Sea, during late summer and autumn, just ahead of the breakdown of seasonal stratification. In this chapter a 1D depth resolving numerical model is used to investigate the respective roles of the wind and barotropic tide in generating shear across the thermocline for a range of different conditions. The model is used to investigate the sensitivity of the shear generation to factors such as water column depth, thermocline depth and thermocline thickness.

The model used in this chapter is a turbulence closure model based on the MY2.0 turbulence closure scheme [Mellor and Yamada, 1974; Mellor and Yamada, 1982; Simpson et al., 1996]. The model is applied to test the effect of different hydrographic conditions on the key driver of bulk shear.

6.1 The hypothesis of shear drivers switch in WIS and NNS

In Chapters 4 and 5 it is shown that, despite similar water column depths and barotropic tidal current speeds, different mechanisms appear to be responsible for the generation of bulk shear. In the western Irish Sea, the bulk shear is dominated by the local inertial frequency and so we consider the shear to be mainly driven by the surface wind stress (Chapter 4). However, in the northern North Sea, the bulk shear exhibits by a mixture of the local inertial frequency and M2 tidal frequency (Chapter 5), which implies in this case the bulk shear is driven by both surface wind stress and bottom tidal stress. A 1D vertical dynamic Turbulence Closure model (hereafter TC model, detailed information about TC model please see Chapter 3) is used to investigate the differing physical balances responsible for the two observed scenarios.

The variability in the physical environment is the focus of the sensitivity testing. Since the study is based on the phenomenon in two different seasonally stratified shelf sea regions, four parameters will be examined with the model: the water column depth, the thermocline depth, the depth ratio (the ratio of thermocline depth to the water column depth), and the thermocline thickness. The depth ratio could potentially vary the relative importance of the wind and the tide to the bulk shear in the thermocline and eventually result in the dominant driver switch. For the purposes of this chapter it is assumed, that the thermocline separates the water column into two layers, a surface mixed layer and a lower mixed layer, and hence the thermocline depth and thickness will impact the thickness of each mixed layer.

6.2 Model sensitivity analysis to identify drivers of bulk shear

Investigation of the impact on the dominant driver of bulk shear by the four parameters accomplished using the TC model with 12 sensitivity tests and analysing the results using rotary spectral analysis. Detailed information on rotary spectral analysis and the TC model can be found in Chapter 2 and Chapter 3 respectively. The sensitivity analysis is carried out over a range of values of water column depth, thermocline thickness, thermocline depth, and the depth ratio (the ratio of the thermocline depth to the water column depth). The thermocline depth is defined as the distance from sea surface to the center of thermocline. For each 10 day model run, the same tide and wind forcing (the same forcing as in WIS) is used.

The initial parameters of the sensitivity tests are shown in tables 1 - 4. Sensitivity tests 1 - 3 (in table 1) attempt to reveal the impact of variation of water column depth on the switch of the bulk shear drives. Sensitivity tests 4 - 6 (in table 2) show the impact on the switch of the bulk shear drivers from the variation in thermocline depth. Sensitivity tests 7 - 9 (in table 3) show the impact of variations in depth ratio and the sensitivity tests 10 - 12 (in table 4) show the impact of variations in thermocline thickness. Each of the sensitivity tests 7 - 9 includes 3 subtests, identifies on tests 7.1 - 7.3, tests 8.1 - 8.3 and tests 9.1 - 9.3. Each set of three subtests has the same depth ratio, but with different water column and thermocline depths (see table 3).

The wind forcing applied in the TC model is a 10 days (days 180 - 190 in 2009) reanalysis of meteorology data from the British Meteorological office reanalysis model. In the TC model, the data was interpolated from 3 hours resolution to 10 minutes resolution. The M2 and S2 tidal forcing are from the surface slopes, which the surface ellipse, orientation and major axis amplitude are estimated by the amplitude and phase of tides.

The rotary spectral analysis of the bulk shear is used to help identify the dominant driver of bulk shear for each of the 12 sensitivity tests.

6.2.1 Water column depth

Tests 1 - 3 are the sensitivity tests using the TC model with a fixed thermocline depth of 20 m, a fixed thermocline thickness 10 m and varying water column depths: 40 m, 60 m and 100 m. These tests demonstrate the role of water column depth in determining the characteristics of the bulk shear. The value of main initial parameters in tests 1 - 3 are listed in table 1.

Table 1 the main initial parameters of water column in sensitivity tests 1 - 3

Test No.	Water column depth (m)	Thermocline depth(m)	Thermocline thickness(m)
Test 1	40	20	10
Test 2	60		
Test 3	100		

The water column structure and the rotary spectral analysis of the results for sensitivity tests 1 - 3 are shown in fig 6.1. Panel 1a, 2a and 3a show the initial water column structure conditions for sensitivity tests 1, 2 and 3. Panel 1b, 2b and 3b are the spectra of distribution of power density for bulk shear from sensitivity tests 1, 2 and 3. It is clear that the water column depth is influencing the dominant frequency of the bulk shear. The dominant frequency switches from tidal frequency (M2 tidal frequency) to near local inertial frequency (in figures in this chapter the local inertial frequency is represented as IF) as the water column depth increases.

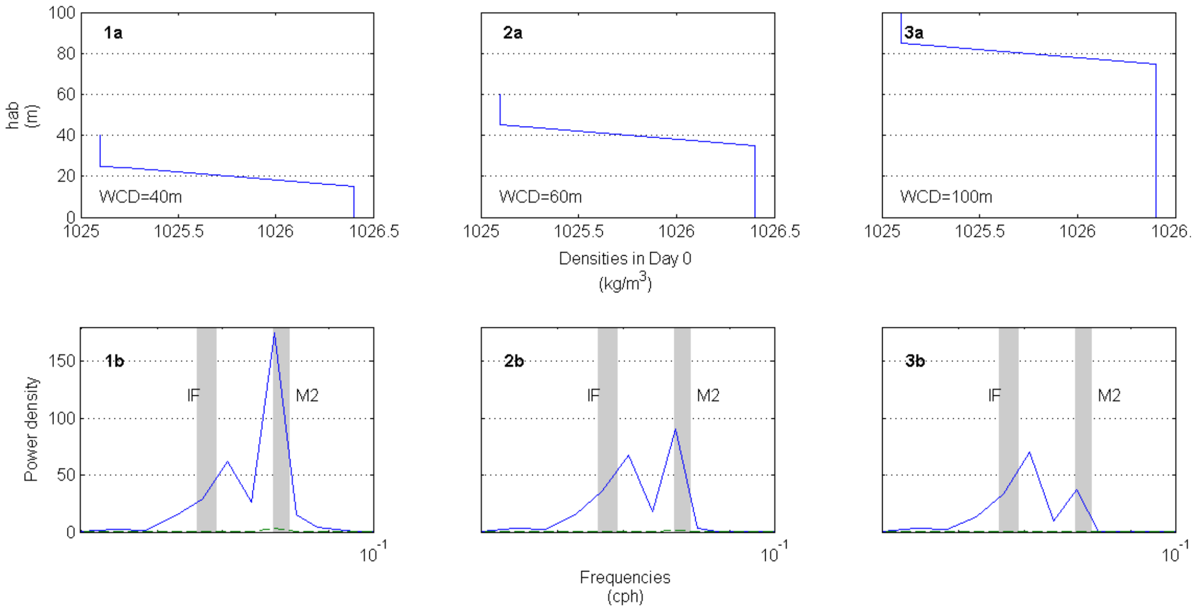

Fig 6.1 The initial water column structures (section 1a, 2a and 3a) and the rotary spectral analysis (section 1b, 2b and 3b) of the modelled bulk shears by sensitivity tests 1 - 3. The parameters of initial water column structures were listed in Table 1. Three sensitivity tests are carried out each with different water column structures. In all cases the thermocline depths (20 m from sea surface) and the thermocline thicknesses (10 m) are the same, whilst the water column depths are different (40 m in test 1, 60 m in test 2 and 100 m in test 3). The peaks of rotary spectral of bulk shears from three tests are all located at near local inertial frequency and near M2 frequencies, which suggests the modelled bulk shear is driven by a combination of the wind and the tide. However the relative impacts of the wind and the tide are different in each test. In section 1b where the initial water column depth is 40 m, near M2 tidal driver is the most important, in section 2b, the importance of M2 tidal driver decreases and the importance of near local inertial frequency increase while the M2 tidal frequency is still the dominant frequency, in section 3b, the importance of driver at near local inertial frequency is bigger than the near M2 tidal frequency.

6.2.2 Thermocline depth

Tests 4 - 6 are the sensitivity tests using the TC model with a fixed water column depth of 100 m and a fixed thermocline thickness 10 m. But with varied thermocline depths of 20 m, 40 m and 60 m respectively. These three tests are to investigate the relationship between the variation of thermocline depth and the relative role of the tide and wind in driving bulk shear in shelf seas. The main initial parameter settings are shown in table 2.

Table 2 the main initial parameters of water column in sensitivity tests 4 - 6

Test No.	Thermocline depth (m)	Water column depth (m)	Thermocline thickness(m)
Test 4	20	100	10
Test 5	40		
Test 6	60		

The water column structures and the results of the rotary spectral analysis of tests 4 - 6 are shown in fig 6.2. Panels 4a - 6a show the water column structures used as the initial conditions for the sensitivity tests 4 - 6. Panels 4b - 6b are the frequency spectra of bulk shear from the rotary spectral analysis, for sensitivity tests 4 - 6. The results show that the dominant frequency of shear variability switches from near local inertial frequency to near M2 tidal frequency as the thermocline depth increases (4a-6a).

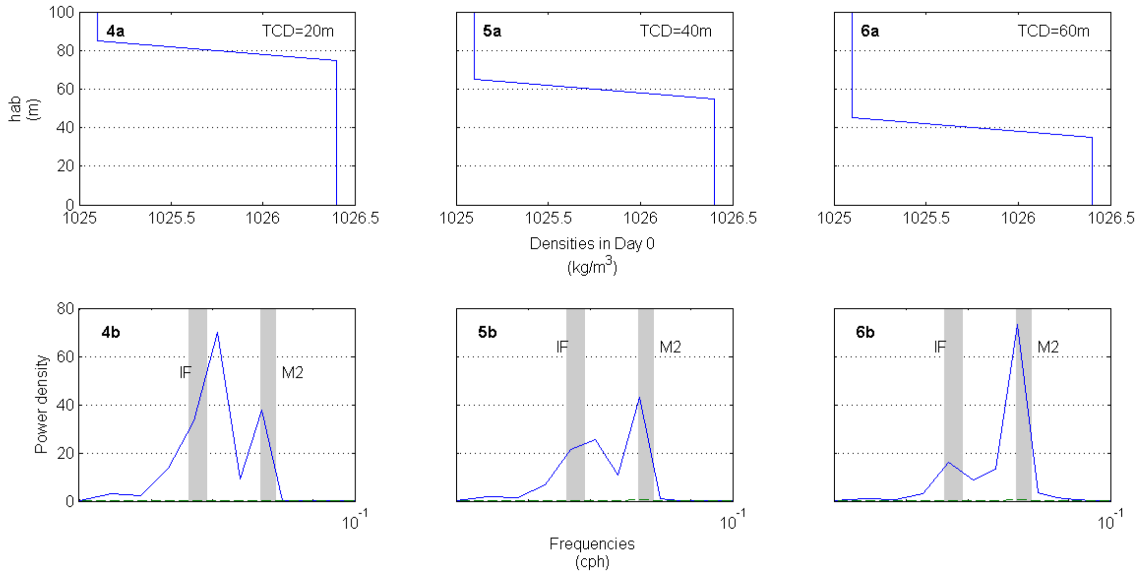

Fig 6.2 The initial water column structures (section 4a, 5a and 6a) and the spectra (section 4b, 5b and 6b) of the modelled bulk shears for sensitivity tests 4 - 6. The initial parameters are displayed in Table 2. Three sensitivity tests processed with different water column structures. In all cases the water column depths (100 m) and the thermocline thicknesses (10 m) are the same, whilst the thermocline depths are different (20 m from sea surface in test 4, 40 m from sea surface in test 5 and 60 m from sea surface in test 6). The peaks of rotary spectral of bulk shears from three tests are all located at near local inertial frequency and near M2 frequencies, which suggests the modelled bulk shear results from a combination of wind and tidally driven processes. However the relative importance of the wind and the tide varies in each test. With a shallow thermocline the shear is dominated by the near local inertial frequency but as the thermocline deepens the importance of M2 tidal driver grows.

6.2.3 Depth ratio

As shown in sections 6.2.1 and 6.2.2, the spectral characteristics of the shear are sensitive to both the depth of the water column and the depth of the thermocline. In order to determine whether the two parameters are linked, a sensitivity analysis varying was under taken with ratios of thermocline depth and water column depth (sensitivity tests 7 - 9). The depth ratio (in table 3 is DR) is defined as the thermocline depth as a fraction of the water column depth (equation 6.1), and the initial parameters are shown in table 3.

$$\text{Depth ratio} = \frac{Thermocline\ Depth}{Water\ Depth} \tag{6.1}$$

Table 3. The main initial TC model parameters of water column in sensitivity test 7 - 9. Each test has 3 subtests which have different thermocline depth and water column depth but share the same depth ratio. In test 7 the ratio is $\frac{1}{4}$, in test 8 the ratio is $\frac{1}{3}$ and in test 9 the ratio is $\frac{1}{2}$.

DR	Test No.	Thermocline depth(m)	Water column depth (m)	Thermocline thickness(m)
$\frac{1}{4}$	Test 7.1	20	80	10
	Test 7.2	30	120	
	Test 7.3	40	160	
$\frac{1}{3}$	Test 8.1	20	60	
	Test 8.2	30	90	
	Test 8.3	40	120	
$\frac{1}{2}$	Test 9.1	20	40	
	Test 9.2	30	60	
	Test 9.3	40	80	

Fig 6.3 shows the initial water column structures for each of the model runs, together with the results of the rotary spectral analysis for sensitivity tests 7.1 - 9.3. Panels 7a, 8a and 9a each shows that three different water column structures for the subtests comparisons (among sensitivity tests 7.1 - 9.3). For each main test (for example test 7) there are 3 subtests (For example tests 7.1 - 7.3) which all share the same depth ratio, but with different thermocline depths and water column depths. Full details are listed in table 3. Panels 7b, 8b and 9b show the rotary spectral analysis of bulk shear for sensitivity tests 7.1 - 9.3.

The dominant thermocline shear frequencies of the three subtests are consistent for each sensitivity test. For example in panel 7b, the relative magnitude of the peaks in the rotary analysis of bulk shear in tests 7.1, 7.2 and 7.3 are consistent. Although the estimate magnitude of the peaks changes, the dominant frequency is near the local inertial frequency for all the subtests. The dominant frequency varies with the depth ratio. For example in the rotary spectral analysis from tests 7.1 and 8.1, peaks in the rotary spectra occur at both the local inertial frequency and the M2 tidal frequency. However in test 7.1 the dominant frequency is the local inertial frequency whilst in test 8.1 the dominant frequency is that of the M2 tide. As the depth ratio grows from $\frac{1}{4}$ to $\frac{1}{2}$ (from test 7 to test 9) the dominant frequency switches from the near local inertial frequency to the M2 tidal frequency. These sensitivity tests 7.1 - 9.3 provide robust evidence that the impact of the water column depth and thermocline depth are not independent of one another and so the depth ratio is a better parameter for the study of dominant shear frequency.

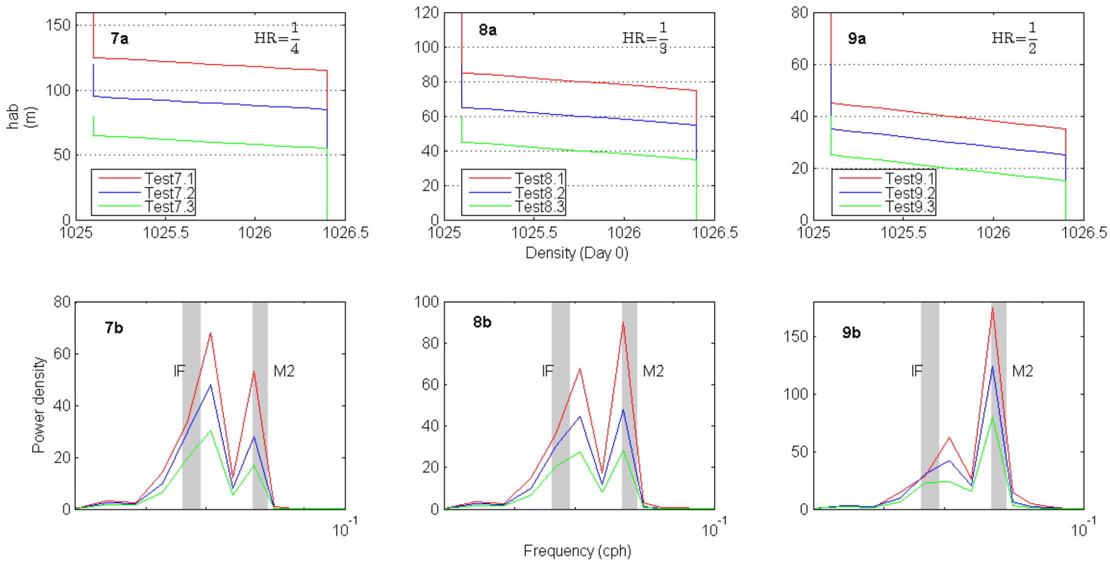

Fig 6.3 The initial water column structures (section 7a, 8a and 9a) and rotary spectral analysis (section 7b, 8b and 9b) of the modelled bulk shears by sensitivity main tests 7 - 9. The initial parameters were displayed in Table 3. Nine sensitivity subtests, which have been divided into 3 groups, processed with different water column structures. All the water column structures have the same thermocline thickness (10 m). All the water column structures under the same main tests have the same depth ratio, but with different thermocline depth and water column depth (detailed data see table 4). The peaks of rotary spectral of bulk shears from nine subtests are all located at near local inertial frequency and near M2 frequencies, which suggests the modelled bulk shear is driven by the combined influences of the wind and the tide. The importance of the wind force and the tide are similar between subtests under the same main test, however that importance varying between the main tests. For example in the main test 7, where the depth ratio is 0.25, the dominant frequency of all the subtests 7.1 - 7.3 are located at near local inertial frequency, and in the main test 8, the dominant frequency of three subtests 8.1 - 8.3 are located at near M2 tidal frequency. This proves that the key factor have impact on the switch of dominant driver is more related to the depth ratio, rather than the thermocline depth or the water column depth individually.

6.2.4 Thermocline thickness

As shown in section 6.2.3 the relative thickness of the surface mixed layer and the lower mixed layer has an impact on the relative significance of the wind and the tide in generating shear across the thermocline. Sensitivity tests 1 to 9 assumed a constant thermocline thickness, whilst sensitivity tests 10 - 12 the thermocline thickness is varied. The initial water column structure parameters were listed in table 4, with the water column depth and thermocline depth fixed (120 m and 60 m respectively) and the thermocline thickness being 10 m, 30 m and 60 m respectively in tests 10 to 12.

Table 4 the main initial parameters of water column in sensitivity tests 10 - 12

Test No.	Thermocline thickness(m)	Water column depth(m)	Thermocline depth(m)
Test 10	10		
Test 11	30	120	60
Test 12	60		

Fig 6.4 shows the results of the model runs with differing thermocline thickness (tests 10 - 12). Panels 10a - 12a show the three different water column structures which are the initial conditions for sensitivity tests 10 - 12. Panel 10b - 12b show the rotary spectral analysis of the bulk shear for sensitivity tests 10 - 12. In all three b panels, the peaks of frequencies correspond to the local inertial frequency and M2 tidal frequency. In all three tests the dominant frequency is the M2 tidal frequency. The relative importance of M2 tidal frequency and local inertial frequency does not vary across tests 10 - 12. This suggests the thermocline thickness does not appear to influence the frequency characteristics of the shear.

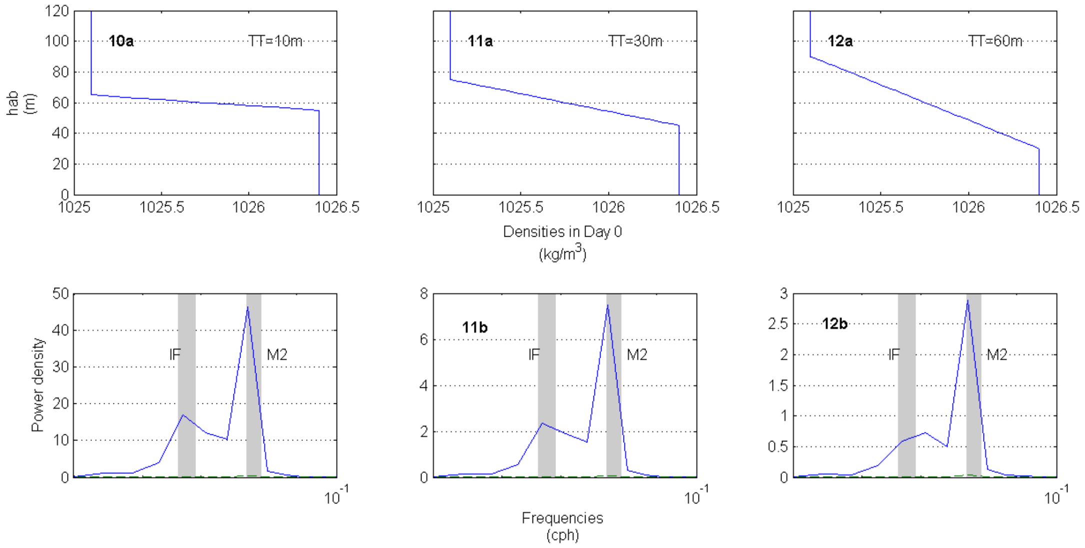

Fig 6.4 The initial water column structures (section 10a, 11a and 12a) and rotary spectral analysis (section 10b, 11b and 12b) of the modelled bulk shears by sensitivity tests 10 - 12. The initial parameters were displayed in Table 4. Three sensitivity tests processed with different water column structures, all the water column structures have the same water column depth (120 m), the same thermocline depth (60 m) and the different thermocline thickness (10 m in test 10, 30 m in test 11 and 60 m in test 12). The peaks of rotary spectral of bulk shears from three tests are all located near the local inertial frequency and the M2 tidal frequencies, which suggests the modelled bulk shear is driven by a combination of the wind and the tide. Among the three b panels, the relative importance of wind force and tide force in each panel are the same. The figure shows that the dominant frequency does not switch while the thermocline thickness significantly varies from 10 m to 60 m. This suggests that thermocline thickness does not impact on the dominant frequency of the bulk shear variability.

6.3 Summary

1. The peaks in the rotary spectral of bulk shears across the sensitivity tests are located at the near local inertial frequency and the near M2 tidal frequency, which suggests the modelled bulk shear results from a combination of wind and tidally driven processes. This is the same conclusion from the rotary spectral analysis of observations repeated in Chapter 5.

2. The dominant frequency in the bulk shear in the thermocline switches from M2 tidal frequency to near local inertial frequency as the water column depth increases.

3. The dominant frequency in the bulk shear in the thermocline switches from near local inertial frequency to M2 tidal frequency as the thermocline depth increases.

4. The dominant frequency in the bulk shear in the thermocline switches from near local inertial frequency to M2 tidal frequency as the depth ratio increases.

5. The impacts on the spectral characteristics of the shear from the water column depth and the thermocline depth are not independent. They are linked by the depth ratio. Water columns with the same depth ratio show the same pattern of spectral characteristics of the shear, even though they have different water column depth and thermocline depth. This is because the ratio of the surface mixed layer depth and the water column depth is more important than the two individual parameters. It is reasonable that when the thermocline is closer to the surface (the depth ratio is small), the shear over the thermocline is more likely to be primarily dependent on wind forcing. However when the thermocline is closer to the bottom (the depth ratio is big), it is reasonable that the thermocline shear is more sensitive to tidal forcing.

6. Varying thermocline thickness does not appear to have a significant impact on the drivers of shear in the thermocline even though it also varies the proportion of surface mixed layer and the water column depth.

Based on the conclusions 4 - 6, the model can now improve the interpretation of the key results from Chapter 4 and Chapter 5 that: the difference in the depth ratio between the western Irish Sea ($\frac{1}{3}$) and the northern North Sea ($\frac{1}{2}$) has a critical impact on the spectral characteristics of the bulk shear in thermocline, directly influencing the switch in the primary bulk shear driver.

However there are other processes responsible for the shear over the thermocline from the observation. An internal tide is one of the processes found in NNS from observation and will be discussed in the next chapter.

Chapter 7

Shear spike generation in periods of weak wind

In the previous chapter, four parameters, the water column depth, the thermocline depth, the depth ratio and the thermocline thickness, were investigated in relation to their impact on the generation of bulk shear. Whilst a two-layer model forced by the wind and the barotropic tide could explain much of the observed shear, it failed to explain the bulk shear spikes generated during the period covered by days 266.7 - 268.3 in the northern North Sea. To try to explain this result, a third process is introduced, the baroclinic tide, which has the potential for the generation of shear, and which has not so far been included in the two-layer model.

To investigate the potential impact from a baroclinic tide, the bulk shear is estimated for a baroclinic tide and is then compared to the bulk shear estimated from observed current velocity. The predicted evolution of shear including the baroclinic tidal contribution is then compared to the observations reported in Chapter 5 for the NNS site.

In particular the vector alignment for bulk shear squared from observed velocities and those from the baroclinic tide are examined to investigate the potential for the baroclinic tide to contribute to shear enhancement through the vector alignment mechanism.

7.1 Impact to the bulk shear from baroclinic tide

A model for the generation of shear has previously been introduced and the model predictions compared against the observations. However, as will be highlighted in this chapter a divergence between predicted and observed shear production is evident for a significant period of the observations. This implies another process is responsible for producing shear besides the direct impact of the wind and the barotropic tide.

Fig 7.1a (Fig 7.1 is reproduced from the data presented in fig 5.21 with a larger time scale) shows the observed evolution of bulk shear squared at the NNS site (blue dotted line), together with the bulk shear squared production (red line), estimated using the 1D two-layer vertical dynamical numerical model. The individual contributions to bulk shear production resulting from the surface wind stress (red line) and the tidal stress at the seabed (black line) are shown in fig7.1b over the study period of days 250 - 305. The two-layer model is that already used in chapters 4 and 5, and the forcing is the same as that used in Chapter 5. Whilst there is good agreement between the model predictions and the observed shear for most of the time, there is a period, days 266.7 - 268.3, (named period A in fig 7.1), when the model predicts that the combined impact of surface wind stress and the bottom tidal stress is negligible. In contrast the observations show this to be a period of significant bulk shear squared (blue dotted line in panel a) (about 0.8×10^{-9} s^{-3}). This suggests an absence of a key physical process in generating thermocline shear in the model.

For the purpose of this study, rotary spectral analysis is applied to the observed bulk shear of period A, to reveal the dominant frequency of the observed bulk shear, and provide clues as to the missing physical process.

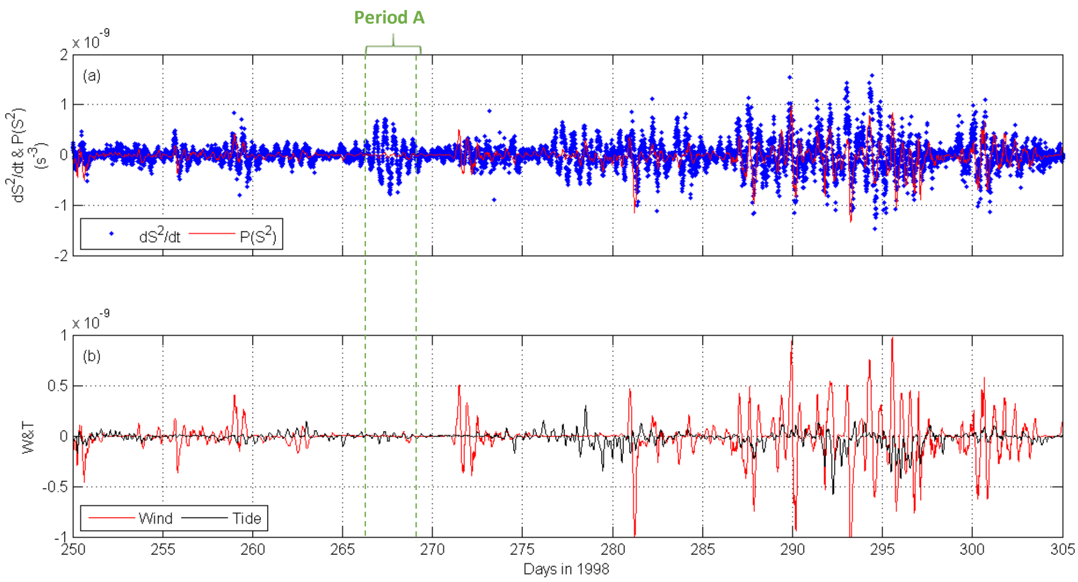

Fig 7.1 The evolution of bulk shear squared, estimated from observed current velocity at NNS site and the bulk shear squared production estimated from the 1D two-layer vertical dynamic numerical model. Detailed information of the model can be found in Chapter 3, detailed information about the model setting can be found in Chapter 5. The study period is days 250 - 305 in 1998. In panel a, the blue dotted line is the evolution of bulk shear squared, estimated from moored water current velocity time series at NNS site, the red line is the bulk shear squared production estimated from the model where the model is driven by the combined force of wind and tide. The red line coincides with the blue dotted line most of the time, the *r* value of correlation is 0.42, $p<0.05$. In panel b, both solid lines are the bulk shear squared productions estimated from the two-layer model. The production of bulk shear squared where model is driven by wind force is the red line, and the black line is the one where model is driven by tide force. The period that we are interested in was marked in the figure: the period A of days 266.7 - 268.3.

7.1.1 Rotary spectral analysis

The rotary spectral analysis is applied to the bulk shear over the period A. The results are shown in fig 7.2. The peak of rotary analysis located near the M2 tidal frequency wave band indicating that the variability in bulk shear during period A is predominately at the M2 frequency.

However, this result appears to contradict the model results (fig 7.1), which shows that there is no barotropic tidal contribution to bulk shear during period A, by revealing that the missing process in the two-layer model is linked to the tide. The apparent contradiction between the predicted shear production and the results of the rotary spectral analysis, suggest that the implied tidal contribution to the production of bulk shear over this period does not come from bottom boundary stress, which is included in the two-layer model, but from another physical mechanism associated with the tide not included in the two-layer model. One such mechanism could be the presence of a baroclinic or internal tide.

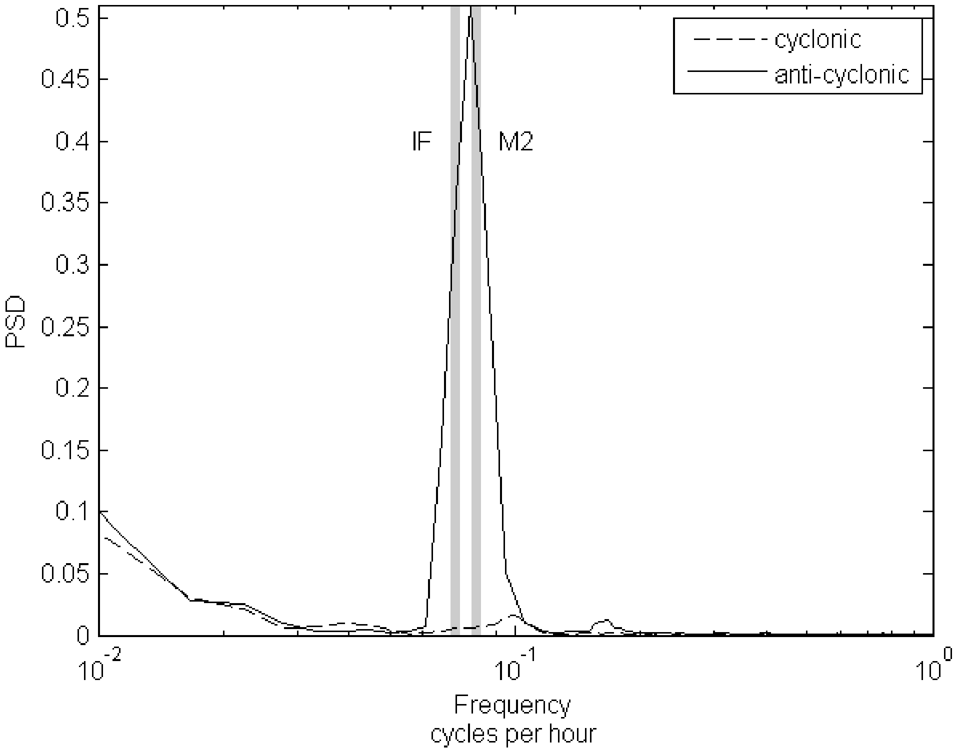

Fig 7.2 Rotary spectral analysis for bulk shear (estimated from moored current velocity in NNS) in period A. Solid line is the anti-cyclonic constituent and the dashed line is the cyclonic constituent. Grey bar indicates the position of local inertial frequency (IF, 0.0719 cycles per hour in NNS site) and M2 tidal frequency (M2, 0.0805 cycles per hour in NNS site). The anti-cyclonic rotation of bulk shear dominants compare to the cyclonic rotation, the dominant frequency of bulk shear concentrated at the M2 tidal frequency.

7.1.2 Baroclinic current and baroclinic tide

As mentioned above, besides the barotropic tide, another potential driver of bulk shear with tidal frequency is the baroclinic tide. Before estimating the baroclinic tide in period A, the contribution of the baroclinic tide to the current velocity profile, over period A is estimated. The observed current velocity profile (*U*) is reasonably considered as formed by the barotropic current (*UT*) and the baroclinic current (*UC*) which is:

$$U = UT + UC \tag{6.1}$$

The barotropic current can be assumed to be the depth averaged velocity and the baroclinic current is estimated as the difference between the depth averaged velocity and the observed current velocity profile. A least squares harmonic fit on the baroclinic current at each depth could be used to estimate the baroclinic tide at each depth. After the least squares harmonic fit, the barotropic current can be separated as a combination of a time averaged baroclinic current (*UCC*) at each depth with the baroclinic tide (*UCT*) at each depth, which is:

$$UC = UCC + UCT \tag{6.2}$$

Because the baroclinic tide is not phase locked to the barotropic tide, this approximation is only valid over a few days and so 2 - 3 days averages are chosen for this calculation.

In the real ocean, *UCT* is formed by several baroclinic tide constituents which can be separated by the least square harmonic fit analysis method. In the least squares harmonic fit the time length of data that has been fitted is limited by the Rayleigh criterion [Tierney et al, 1998; Emery and Thomson, 1998], As described in Chapter 2, when we try to separate signals of two frequencies, for example frequency f_1 and frequency f_2, the time length of the fitted data is limited by these two frequencies which is $|f_1 - f_2| > \frac{1}{T}$, where T is the time length. Thus in this chapter, the candidate tidal frequencies used for least squares harmonic fit are M2, S2 and M4 tide constituents since they are the main tides in the NNS at the mooring site. However, due to the Rayleigh criterion, the time length required to separate the M2 (0.0805 cycles per hour) and S2 (0.0833 cycles per hour) tidal signal is 357.14 hours (14.88 days), and to separate the M2 (0.0805 cycles per hour) and M4 (0.1610 cycles per hour) tidal signal, the time length required is 12.87 hours (0.54 days). Since the period A is 1.6 days, the tide constituents chosen for least squares harmonic fit is M2 and M4, which represent the semidiurnal and quarterdiurnal tidal constituents respectively.

The least square analysis is carried out using the Matlab routine t_tide.m [Pawlowicz et al., 2001]. The profiles of amplitude and phase for the baroclinic tide for period A are shown in fig 7.3.

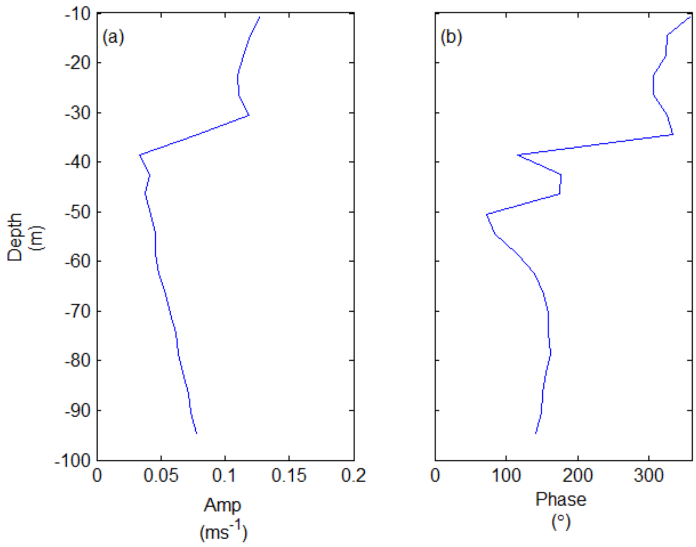

Fig 7.3 The amplitude (a) and phase (b) profiles of baroclinic tide in period A, where the baroclinic tide is estimated by the least squares harmonic fit and accomplished by using the Matlab routine t_tide.m. Y axis is water depth from sea surface. In panel a, the amplitude of baroclinic tide in the surface mixed layer is around 0.125 ms^{-1} and the amplitude in the lower mixed layer linearly increased from 0.05 ms^{-1} to 0.075 ms^{-1} along with increasing water depth. In the thermocline, the amplitude of baroclinic tide drops dramatically from 0.125 ms^{-1} to 0.05 ms^{-1} within 10 m. In panel b, an obvious phase lag can be observed between the surface mixed layer and lower mixed layer which is around 180°. The phase in the surface mixed layer is around 350° and the phase in the lower mixed layer is from 100° to 200°.

The amplitude and phase of the baroclinic tide over period A is shown in figure 7.3. Shear in the flow is evident between the surface mixed and lower mixed layer as a consequence of the flow being phase shifted by 180 ° over the thermocline. Fig 7.3a shows the strongest velocity is close to the sea surface (0.125 ms^{-1}) which decreases rapidly with depth to the thermocline (from 0.125 ms^{-1} to 0.03 ms^{-1}). The current velocity in the lower mixed layer linearly increases with depth from 0.05 ms^{-1} to 0.075 ms^{-1}. The fig 7.3b shows the vertical variation in the phase of the velocity. There is a near 180 °phase shift from surface mixed layer to lower mixed layer. The phase profile shows a clear two layer structure which is consistent with mode 1 baroclinic tide [Simpson and Sharples, 2012].

Baroclinic tide, also known as internal tide, can be displayed in different modes. The different modes represent the different vertical structures for the baroclinic waves, and a bigger mode number represents a more complex vertical structure [Bell, 1974]. The model 1 baroclinic tide have a simple two layer vertical structure, and with a 180 °phase difference between two layers (as shown in fig 7.3b).

7.1.3 Comparison of bulk shear estimate from the baroclinic tide and observed current velocity profile

The bulk shear associated with the baroclinic tide is estimated as the tidal current velocity difference over a certain vertical distance. For the purposes of this calculation the surface mixed layer is assumed to be between the depths of -34.5 m to -10.5 m, the lower mixed layer is from -94.5 m to -42.5 m and the thermocline is from -42.5 m to -34.5 m (see fig 7.3a). The E-W and N-S bulk shear constituents estimated for the baroclinic tide and observed current velocity and are shown in fig 7.4. Fig 7.4a shows the bulk shear constituents at E-W direction with the blue line the observed bulk shear constituents over period A, the red line is the bulk shear estimated for the baroclinic tidal component and the green line is the baroclinic tidal component plus an offset of 0.0015 s^{-1}. Fig 7.4b shows the bulk shear constituents at N-S direction, the blue line being the observed bulk shear and the red line the bulk shear estimated for the baroclinic tidal component.

In fig 7.4a, an offset of 0.0015 s^{-1} is added to the baroclinic tidal component (green line), so that estimated baroclinic tide bulk shear matches the observed shear (blue line) in E-W direction. Whilst the offset improves the agreement between the two profiles it does not contribute to the correlation. The E-W bulk shear from baroclinic tide is strongly correlated to the observed current profile, with an r value of 0.94 and $p < 0.05$. The offset, which assumed due to the lack of S2 tidal constituent in the harmonic fit or a residual flow component, needs a further discussion in the future work. In fig 7.4b the bulk shear estimated for the baroclinic tide (red line) is coincident with the bulk shear from observation (blue line) in N-S direction, with an r value of 0.93 and $p < 0.05$.

The strong correlation between the bulk shear predicted for the baroclinic tide with that observed implies a significant contribution to bulk shear from the baroclinic tide. This result implies that the baroclinic tide can also provide a significant source of shear, and so contribute to mixing, through interaction with the shear spike mechanism.

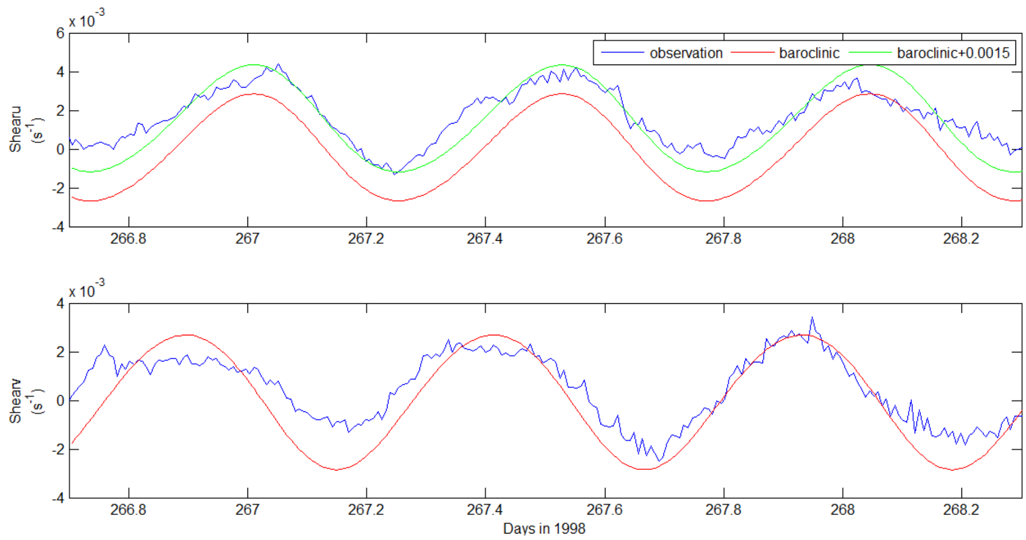

Fig 7.4 The bulk shear components of E-W (U) and N-S (V) directions estimated from observed water current velocity and baroclinic tide in period A. In both panels, the red line is the bulk shear estimated from baroclinic tide, green line is the bulk shear estimated from baroclinic tide plus an offset of 0.0015 s^{-1} and the blue line is the bulk shear from observed current velocity. (a) the bulk shear from baroclinic tide plus 0.0015 s^{-1} coincident with the bulk shear from observed water current velocity. (b) the bulk shear from baroclinic tide coincident with the bulk shear from observed water current velocity.

7.1.4 The sum of bulk shear productions from a two-layer model and the baroclinic tide

The individual contributions to shear from different processes are compared with the observations (Fig 7.5). These processes are now the shear production from two-layer model (panel b) and baroclinic tide (panel c). As shown in panels b and c, there are periods of good agreement between the estimated shear and the observations, while there are also periods where the agreement is not so good.

The periods of agreement between the red and blue lines are different (panels b and c). During the 'blue periods' the evolution of shear from baroclinic tide (red line) coincides with that from current velocity (panel c, the observation is the blue line), while the evolution of shear from two-layer model does not (panel b). This implies during the 'blue periods', the model does not contain all of the physical processes necessary to reproduce the observations.

During 'green periods', panels b and c show both the evolution of shear from baroclinic tide (red line in panel c) and shear production predicted using the two-layer model (red line in panel b) coincides observed current profile (blue lines in panels b and c).

During the rest 'no color periods', the shear production predicted using the two-layer model (red line in panel b) coincides with the observed current profile (blue line in panel b). The inclusion of the baroclinic tide at this time weakens the agreement (panel c). Thus, in the 'no color periods', the model could reproduce the observations without the need to consider the contribution of the baroclinic tide, suggesting that the baroclinic tide does not make a significant contribution to shear at these times.

In considering the different coincidences, over the different time periods, between the two-layer model (b) and the baroclinic tide (c), the fit to the observations might be improved by adding the estimated shear production in panel b and panel c together (fig 7.4a, red line). Panel a shows that during the 'blue periods' and 'green periods', the estimated shear production agree well with the observations. However for the rest of the time (the no color periods), there is a significant divergence between the predicted (red line) and the observed shear (blue line).

In comparing panels a to e, for the two 'blue periods' there is a clear coincidence between the evolution of shear in the observations and predicted for the baroclinic tide (panel c). This is a time when the wind is weak and the phase of the tide is close to a spring tide.

Comparing the panels a to e for the two 'green periods', it is clear that the best agreement between the observed shear production (blue lines in panels a, b and c), the two-layer model (red line in panel b), the baroclinic tide (red line in panel c), and the baroclinic tide combined with the two-layer model (red line in panel a) coincide with a period when the wind is strong and the tide is close to a spring tide.

For the remainder of the time series it is clear that the coincide of shear productions (observation and two-layer model) in panel b occurs when the wind is strong.

Thus, the contribution of the baroclinic tide shear takes place close to a spring tide. However the success of the model during periods of high winds suggests that at these times the wind is dominating shear production.

On the basis of these results we conclude that whilst the two-layer model works under strong wind forcing conditions, the contribution of the baroclinic tide to thermocline shear becomes important at this location during periods of weak wind forcing and during spring tides.

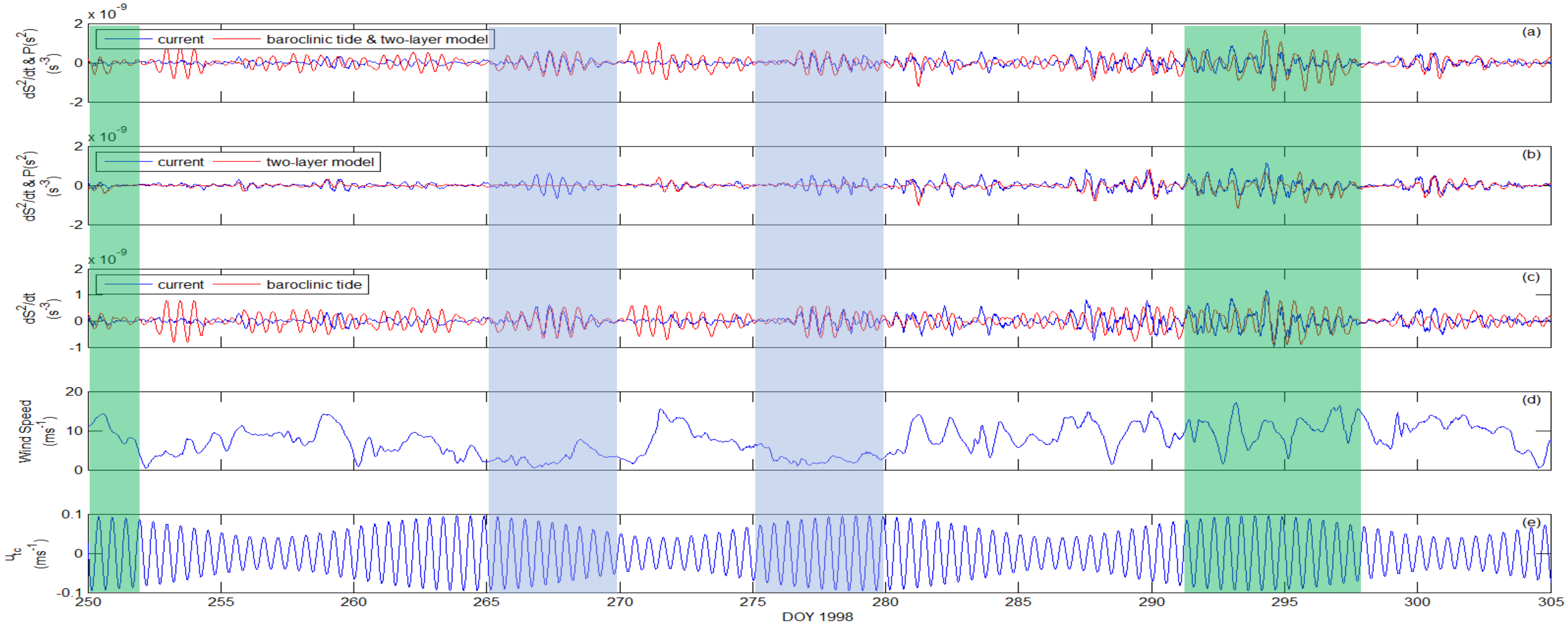

Fig 7.5 Shows the evolution of shear estimated from observed current velocity, compared with that from baroclinic tide, from two-layer model, the wind speed and barotropic tidal current during the same period. a) Evolution of shear from observed current velocity (blue line), and the evolution of shear from baroclinic tide plus the shear production from two-layer model (red line). b) Evolution of shear from observed current velocity (blue line), and the shear production from two-layer model (red line). c) Evolution of shear from observed current velocity (blue line), and the evolution of shear from baroclinic tide (red line). d) Time series of wind speed. e) Time series of barotropic tide at E-W direction.

7.1.5 The alignment of baroclinic tide and bulk shear

As described in precious chapters, the impact of wind-shear alignment on the generation of bulk shear spike can be significant. In this chapter, we have considered the alignment of the baroclinic tidal shear vector with the bulk shear as a mechanism for the generation of shear spikes. The direction of the baroclinic tide vector varies with depth. The baroclinic tide vector near the bottom of the thermocline (depth of 39 m) is selected here to show the impact of the baroclinic tide on the bulk shear. The baroclinic tide phase change is about 180 °at the bottom of thermocline relative to that at the top of the thermocline (fig 7.3).

Fig 7.6 shows the wind speed (a), baroclinic tide direction and shear direction (b), bulk shear squared (c), and the evolution of bulk shear squared and the production of shear squared (d) during period A. From this figure it is evident that when the baroclinic tide vector and the bulk shear vector are aligned (marked by orange lines), the growth rate of bulk shear squared reaches its peak (also this is where the magnitude of bulk shear starts to increase).

These results lead to a new hypothesis is that the wind shear alignment creates shear spikes across the top of the thermocline, whilst the baroclinic tide shear alignment creates bulk shear spikes across the base of the thermocline.

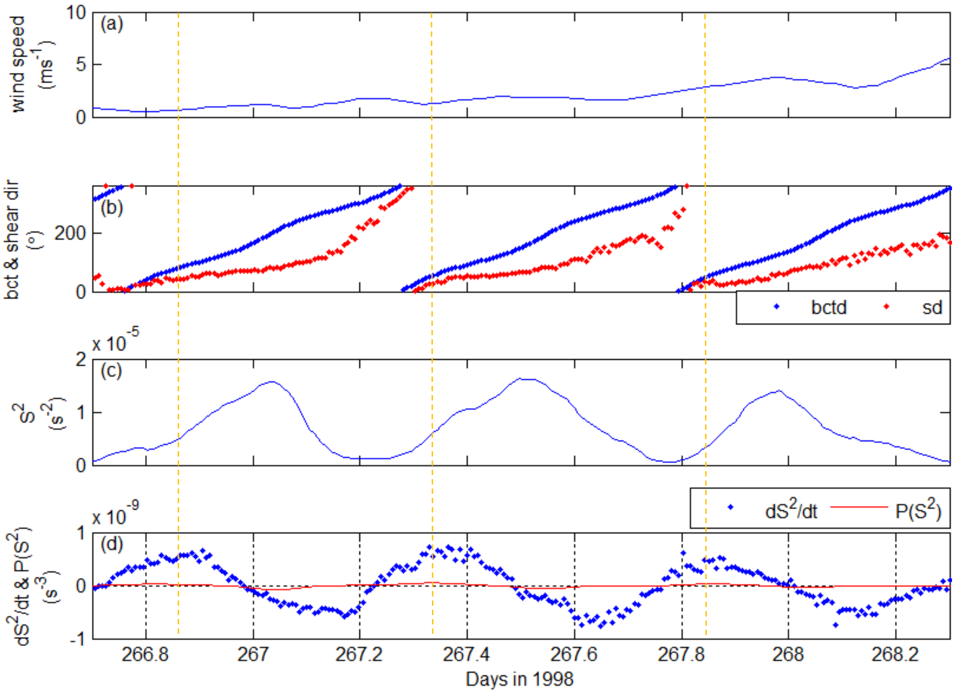

Fig 7.6 Time serials of wind speed (a), directions of baroclinic tide and bulk shear (b), bulk shear squared from observed water current velocity in NNS site (c), evolution of bulk shear squared from observed water current velocity in NNS site and the production of bulk shear squared estimated by 1D two-layer vertical dynamical numerical model with the combined initial force of wind and tide (d). The study period is the period A (days 266.7-268.3). (a) Shows the wind speed (blue line) is less than 5 ms^{-1} in period A, the time series of wind is a smooth line without significant peaks or troughs. (b) Shows the baroclinic tide (blue dotted line) and the bulk shear (red dotted line) all rotate anti-cyclonic with the same period of 0.4 day. (c) Shows the time series of bulk shear squared (blue line) in period A, the bulk shear squared has three peaks and three troughs with a period of 0.4 day. (d) Shows the comparison of evolution of bulk shear squared (blue dotted line) and the modelled bulk shear production (red line) with the initial force of wind and tide, the amplitude of evolution of bulk shear squared (8×10^{-10} s^{-3}) is significantly larger than the amplitude of the modelled production of bulk shear squared (nearly 0). The orange dashed lines indicate the moment of bulk shear from observed current velocity and baroclinic tide alignment.

7.2 Summary

1. The two-layer model which includes the impacts of the wind and the barotropic tide on thermocline shear generally reproduces observed shear. However, the model fails to reproduce the observed shear during period A (days 266.7-288.3). This result suggests that the wind and barotropic tidal forcing alone are not sufficient to explain the observed evolution of shear at that time and so implies the lack of a key mechanism, for the generation of shear across the thermocline, at this time.

2. The missing physical mechanism for period A is shown related to the dominant M2 tidal constituent using rotary spectral analysis.

3. The phase and amplitude profiles of the baroclinic tide during period A show a clear two layer structure, with a 180 °phase lag between the surface and lower layers.

4. The bulk shear estimated from the baroclinic tide is coincident with the bulk shear estimated from observed current velocity profile.

5. The evolution of the bulk shear squared coincides with the alignment of the baroclinic tidal current vector and the bulk shear vector.

Chapter 8

Summary and discussion

Shear across the thermocline was investigated because of its close link to diapycnal mixing. Diapycnal mixing affects the nutrients and carbon exchange between the surface mixed layer and the lower mixed layer in stratified shelf seas, linking it to the sink of carbon in shelf seas and the global carbon cycle [Rippeth et al., 2014].

In marginally stable stratified shelf seas, the Richardson number is close to one [Rippeth et al., 2005; Rippeth et al., 2009]. Periods of enhanced shear will lead to the reduction in Richardson number, potentially leading to shear instability and turbulence mixing across the thermocline. As such determining the dominant driver of shear is a key focus in the study.

In this thesis we examine time series data collected from two seasonally stratified shelf sea locations. Firstly, observations in the western Irish Sea are taken for the period during the early stage in the development of stratification. The second data set was collected in the northern North Sea during the autumnal breakdown of stratification. A number of spectral techniques are used to examine the contribution of the wind and tide to the evolution of shear across the thermocline. A sensitivity analysis was also undertaken using a numerical model to determine the relative contributions to the bulk shear due to forcing by the wind, and the barotropic tide. The analysis shows that the ratio of the thermocline depth to the water depth (the depth ratio) is an important parameter in determining the relative importance of wind and tide in generating shear across the thermocline.

Previous studies have shown that a key driver of shear across the thermocline in the stratified northern North Sea is the surface wind stress [Burchard and Rippeth, 2009]. The contribution to the shear from the barotropic tide (though bottom stress) can be neglected compared with the contribution from the wind (though surface stress) for the conditions presented [Burchard and Rippeth, 2009].

In the study here, the principle drivers of shear were identified using rotary spectral analysis of data from both the western Irish Sea (hereafter WIS) and the northern North Sea (hereafter NNS). This analysis shows the M2 tidal frequency could be a dominant frequency in thermocline shear production, which is in contrast with the earlier research. In the WIS, the dominant frequency is local inertial frequency, and in the NNS the dominant frequencies are local inertial frequency and M2 tidal frequency. To investigate the relative importance of wind and barotropic tides as drivers of bulk shear in the WIS (Chapter 4) and NNS (Chapter 5), a model investigation which includes a sensitivity analysis and a correlation analysis was undertaken in Chapters 6 and 7.

In Chapter 4, the observations were collected in the WIS during a period when the water column structure was developing from the onset of stratification to the point when it is well stratified in 2009. In contrast in Chapter 5, the water column structure in the NNS developed from well stratified toward the breakdown of stratification. The main driver of bulk shear during these two periods varies. In the first scenario, in Chapter 4, the bulk shear was dominated by wind driven inertial oscillations, with the alignment of the wind vector and the bulk shear vector generating shear spikes. In contrast in Chapter 5 the second scenario, the bulk shear is determined by a combination of the wind and the barotropic tide, and there is no simple relationship between the occurrence of shear spikes and the alignment of the vectors of shear, the wind and the barotropic tide.

In order to further understand the causes of shear variation in these contrasting cases, two models and several analysis methods were applied. Five parameters were investigated: the water column depth; the thermocline depth; the depth ratio; the thermocline thickness and the strength of baroclinic tide. The four parameters of the water column depth, the thermocline depth, the depth ratio and the variation of thermocline thickness were examined by sensitivity analysis in Chapter 6. The impact of the variation in the baroclinic tide was examined in Chapter 7 by the correlation analysis of shear from baroclinic tide and shear from observed current velocity.

8.1 Shear generation during development of seasonal stratification

In the study areas, stratification begins to form in May and develops through the summer with a robust two layer structure usually established by July.

The variation of density at both locations of interest (WIS and NNS) is largely determined by variations in temperature and so we have used temperature profiles to represent the water column structure.

In the WIS, over the period of the observations, the wind speed ranged from 5 ms^{-1} to 10 ms^{-1}, occasionally rising to 15 ms^{-1}. There were no significant storm events during the period (a storm is defined as wind speeds exceeding 24.5 ms^{-1}, in accordance with the Beaufort scale). The tidal current speed ranged from 0.3 ms^{-1} at neaps and 0.4 ms^{-1} at springs.

Increased current speeds in the surface mixed layer were observed to coincide with periods of high wind speed. This suggests the low frequency shear components are driven by the low frequency wind events, which are due to the occurrence of higher wind speed events. The observed increase in current velocity is limited to the surface mixed layer: the current velocity in the lower mixed layer does not correlate with the increase in wind speed. This suggests the observed lower mixed layer currents do not appear to respond directly to the wind. However closer inspection of the baroclinic current profile shows that the enhanced currents in the surface mixed layer do coincide with enhanced currents in the lower mixed layer which are 180° out of phase. This result is consistent with earlier studies [Millott and Crépon, 1981; Maas and Van Haren, 1987; Sherwin, 1987; van Haren et al., 1999; Knight et al.,2002; Rippeth et al., 2002; Shearmann, 2005; Sobarzo et al, 2007].

The strong correlation of wind and shear, especially the concurrent spikes in wind speed and shear, suggests that the wind is the dominant driver of shear spikes in this scenario. Rotary spectral analysis of the time series of bulk shear shows that the dominant frequency in the bulk shear spectrum is the local inertial frequency. This supports the suggestion that the bulk shear is dominated by the wind, and associated with the formation of inertial oscillations.

Wind-shear alignment generates shear spikes [Brannigan et al., 2013]. At the point of wind and shear alignment, the rate of growth of shear reaches its maximum. When the wind and the shear directions diverge by 90°, the shear ceases to grow, and the shear reaches its peak. It takes about 3.5 hours for the divergence of wind and shear directions to increase from 0° to 90°, which is about a quarter of the local inertial period (14.84 hours).

A two-layer numerical model [Burchard and Rippeth, 2009] is able to reproduce the observed shear generation by the surface wind stress and bottom tidal stress. Using the model the individual contributions from the surface wind stress and bottom tidal stress can then be separated.

The model is run for three different forcing conditions, tide only, wind only and a combination of both. The correlations between the three two-layer modelled shear productions with the observation were compared. In the WIS, The shear production estimated from the wind only forced model shows the greatest correlation with the observed shear production. This highlights the importance of wind forcing in the shear production. The coherence analysis between the shear production in the three modelled scenarios and the WIS observations shows that, the modelled and observed shear productions have the greatest similarity at inertial frequency. This suggests the model will perform better in estimating shear production in areas with strong wind forcing and weak tide.

8.2 Shear generation toward the breakdown of seasonal stratification

The observations from the NNS site from September to November 1998 provide an example of the water column stratification evolving from being fully developed toward the autumnal breakdown. Over the period of the observations, the water column evolved from a two layer structure in September with a surface to bottom temperature difference of 4.8℃ and a relatively thicker thermocline, to that with a thinner and deeper thermocline and a surface to bottom temperature difference of 1.4℃ at the end of the observational period in November.

In terms of the wind there are two regimes in this time series, one before and one after day 281. Before day 281 there are a series of windy periods separated by calm periods. During the windy periods, wind speeds > 10 ms^{-1} on days 251, 257 - 263 and 272. In the quiet periods, wind speeds < 10 ms^{-1} (and most of the time < 5 ms^{-1}). After day 281, the wind is stronger. Using the definition of a storm wind speeds > 24.5 ms^{-1}, there are no significant storm events during this observational period.

The characteristics of the barotropic current can be separated into two periods, before and after day 272. Before day 272, the barotropic current is coincident with the barotropic tide whilst after day 272, a divergence between the observed and tidally driven barotropic current occurs. The tidally driven barotropic current, or known as barotropic tide, is estimated from the tidal fit of barotropic current. This divergence is particularly apparent in the E-W direction: the barotropic current is 2 - 3 times bigger than the barotropic tide. Thus before day 272, the barotropic current is clearly coincide with the barotropic tide. Whilst after day 272, another driver is involved. Since the divergence in the characteristics of the currents coincides with the enhanced wind on day 272, the wind could be a strong candidate driving this divergence.

The enhanced currents observed in the surface mixed layer are not simply correlated to windy events or with the tide. Enhanced currents were observed during days with strong winds coinciding with a neaps tide, however, enhanced currents were also observed during conditions of neap tides and weak winds. The enhancement of barotropic current velocity does not therefore simply correlated to the wind or the tide.

A rotary spectral analysis of bulk shear suggests that shear is influenced by both wind and tide. Shear spikes occur under conditions of strong winds and spring tides, however they also occur at other time without strong winds and spring tides. The bulk shear-wind alignment or bulk shear-tide alignment sometimes leads to a peak in evolution of bulk shear squared however this is not always this case.

Three runs of the two-layer model were undertaken with different forcing: only surface wind stress; only bottom tidal stress; and combined surface wind and bottom tidal stress. Taking days 288 - 298 as example, the strongest agreement between the modelled shear production and the observed evolution of shear occurs using a combination of wind and tide (r = 0.39). However a similar agreement is found using only the wind forcing (r = 0.39). Weaker fits are obtained when the model is forced by tide only (r = -0.03), which suggests in the WIS the tide does not contribute to the shear production, and suggests that during the windy period, wind will be the dominant driver of bulk shear.

8.3 Sensitivity analysis of the impact of varied hydrographic scenarios to shear

A sensitivity analysis was then applied to investigate the sensitivity of the driver to the hydrographic conditions. Four parameters were considered to describe the differing hydrographic conditions. They are the thermocline depth, water depth, depth ratio and thermocline thickness.

A turbulence closure model was employed to investigate the impact of varying water column structure on bulk shear using the four parameters. Twelve sensitivity tests were carried out and the results subjected to rotary spectral analysis.

Of the four parameters, the depth ratio appeared to be the most important parameter in determining the shape of rotary spectrum. An increase in the depth ratio from $\frac{1}{4}$ to $\frac{1}{2}$ leads to a switch in the dominant frequency in the spectral analysis from the near local inertial frequency to M2 tidal frequency. The impact of depth ratio is explained by the fact that when the thermocline is closer to the surface, i.e. when the depth ratio is small, the shear over the thermocline will be more strongly influenced by the wind than the tide. In contrast, when the thermocline is deeper, i.e. the depth ratio is large, the bottom stress has a bigger impact on the thermocline shear.

The thermocline depth and water depth each have an impact on the driver of bulk shear. As the water column depth increases, the dominant frequency of the shear switches from M2 tidal frequency to near local inertial. As the thermocline depth increases, the driver switches from wind induced near local inertial frequency to tidal as evidenced by the dominance of the M2 tidal frequency in the bulk shear power spectrum. But the impacts of thermocline depth and water depth also interact with each other and cannot be individually considered as the key determinant for the switch of bulk shear driver. Varying the thermocline thickness, even though it affects the thickness of surface mixed layer and lower mixed layer, does not have impact on the driver of thermocline.

Based on the understanding that the relative significance of bulk shear drivers is determined by the depth ratio, the interpretation of the switch of bulk shear drivers between WIS and NNS is due to the different depth ratio, $\frac{1}{3}$ and $\frac{1}{2}$ respectively. As discovered in Chapter 6, the role of the barotropic tide in the production of bulk shear in the stratified shelf seas becomes more significant with the increase of the depth ratio. In an evolution of shelf sea stratification, with the same wind and tide forcing, when stratification begins to develop, the depth ratio is small and the bulk shear generation is dominated by the wind, with the barotropic tide playing a less important role. However, during the autumn break down stage of stratification, the thermocline deepens and so the depth ratio increases, the importance of the barotropic tide in generating bulk shear increases.

8.4 Shear spikes generation in a weak wind generation and weak barotropic tide generation period

The switch of bulk shear drivers is broadly explained by the variation in the depth ratio in section 8.3. However, the observations included periods when the evolution of bulk shear was not explained by the barotropic tide and the wind. From the observation in the NNS site, a divergence of shear squared production between the model and observation is evident. The model predicts that the bulk shear squared negligible at this time, however the shear squared estimated from observed current velocity is significant. This discrepancy indicates that a key physical driver of shear is not included in the model. The rotary spectral analysis was applied to investigate further the nature of this unrepresented phenomenon.

Rotary spectral analysis shows the dominant frequency of shear spike located at the M2 tidal frequency. As the two-layer model included the contribution to bulk shear from barotropic tide, the missing contribution to bulk shear with M2 tidal frequency is thought to come from the baroclinic tide.

The baroclinic tide was estimated from a tidal fitting of the baroclinic current with the M2 and M4 tidal constituents. The baroclinic current was estimated by subtracting the depth average velocity from the observed current velocity profile. Comparing the bulk shear from the baroclinic tide and the bulk shear from the observed current velocity, it is obvious that during period A (the days 266.7 - 268.3), in the E-W direction, the modelled and observed bulk shear components coincide with each other with an offset of 0.0015 s^{-1}, the r value of the two bulk shears is 0.95. In the N-S direction, the components coincide with each other with an r value of 0.93. The high correlation implies a significant contribution to bulk shear from the baroclinic tide in period A.

The observed bulk shear spikes coincided with the alignment of the bulk shear vector and the baroclinic tide vector. The peak of evolution of bulk shear coincides with the alignment of the bulk shear and the baroclinic tidal vectors.

8.5 Conclusions and questions for future research

This study has increased understanding of the relationship between bulk shear spikes at the thermocline and their forcing by the wind and the tide. A key outcome is an assessment of the relative importance of the tide and the wind varies for an evolving of water column structure as seasonal stratification develops. The dominant driver of the bulk shear switches between the tide and the wind with the variation of the water column structure. The depth ratio, which is the ratio of thermocline depth and water depth, is a useful parameter in determining which of forcing are dominant. Also, in addition to the impact from boundary stress due to shear from the wind and the barotropic tide, the baroclinic tide is identified as another driver of bulk shear at thermocline.

The study presented assumes constant forcing of wind and tide. Future studies should examine the relative importance of the forcing as water column structure and the relative strength of the forcing change, for example through the spring-neap cycle.

Three unsolved issues have been highlighted by this study. Two are related to the baroclinic tide, and the third is related to the role of thermocline structure and thickness in determining the nature of the bulk shear:

1. In the observation from the NNS site, an offset of bulk shear was observed in the E-W direction between the bulk shear estimated from observed E-W current velocity and the bulk shear estimated from the baroclinic tide. We still do not know what causes this offset, why it occurs in the E-W direction but was not the N-S direction?

2. The time series from the NNS site showed periods when the baroclinic tide was an important contributor to the generation of bulk shear. How due to the limited data it is not possible to examine further the interaction between the relative impacts of strong wind, barotropic tide and baroclinic tide on shear generation.

3. Although the impact of thermocline thickness on bulk shear is shown to be negligible, it is still potentially an interesting topic. Theoretically, the variation of the thickness of surface mixed layer and the lower mixed layer should have impact on the bulk shear, because the current velocity of each layer would change. This contradiction between the theory, which suggests the thermocline thickness should have impact on bulk shear, and

the modelled result, which shows the thermocline thickness does not affect the bulk shear, would be an interesting direction for a future study.

Bibliography

P G Baines. On internal tide generation models. *Deep Sea Research. Part A. Oceanographic Research Papers*, 29, 307, 1982. URL https://doi.org/10.1016/0198-0149(82)90098-X

J E Bauer, W J Cai, P A Raymond, T S Bianchi, C S Hopkinson, *and* P A G Regnier. The changing carbon cycle of the coastal ocean. *Nature*, 504, 61-71, 2013. URL http://www.nature.com/nature/journal/v504/n7478/full/nature12857.html?foxtrotcallback=true.

T H Bell. Effects of shear on the properties of internal gravity wave modes. *Deutsche Hydrographische Zeitschrift*, 27, 57-62, 1974. URL https://doi.org/10.1007/BF02226477

P Berrisford, P Kållberg, S Kobayashi, D Dee, S Uppala, A J Simmons, P Poli, and H Sato. Atmospheric conservation properties in FIIERA-Interim. *Quarterly Journal of the Royal Meteorological Society*, 137, 1381-1399, 2011. URL http://onlinelibrary.wiley.com/doi/10.1002/qj.864/full

L Brannigan, Y D Lenn, T P Rippeth, E McDonagh, T K Chereskin, and J Sprintall. Shear at the Base of the Oceanic Mixed Layer Generated by Wind Shear Alignment. *Journal of Physical Oceanography*, 43, 1799-1810, 2013. URL http://journals.ametsoc.org/doi/abs/10.1175/JPO-D-12-0104.1

H Burchard and T P Rippeth. Generation of Bulk Shear Spikes in Shallow Stratified Tidal Seas. *Journal of Physical Oceanography*, 39, 969-985, 2009. doi:10.1175/2008JPO4074.1. URL http://journals.ametsoc.org/doi/full/10.1175/2008JPO4074.1

C T A Chen and A V Borges. Reconciling opposing views on carbon cycling in the coastal ocean: continental shelves as sinks and near shore ecosystems as sources of atmospheric CO_2. *Deep Sea Research II*, 56, 578-590, 2009. doi:10.1016/j.dsr2.2009.01.001. URL http://www.sciencedirect.com/science/article/pii/S0967064509000162

P D Craig. A model of diurnally forced vertical current structure near 30°latitude. *Continental Shelf Research*, 9 (11), 965-980, 1989. URL http://www.sciencedirect.com/science/article/pii/0278434389900022

E D'Asaro. The energy flux from the wind to near-inertial motions in the surface mixed layer. *Journal of Physical Oceanography*, 14, 1043-1059, 1985. URL http://journals.ametsoc.org/doi/abs/10.1175/1520-0485%281985%29015%3C1043%3ATEFFTW%3E2.0.CO%3B2

E Deleersnijder. A note on the stability functions of the Mellor-Yamada level $2\frac{1}{2}$ Turbulence Closure. *Bulletin de la Société Royale des Sciences de Liège*, 61, 5, 397-404, 1992. URL http://agris.fao.org/agris-search/search.do?recordID=AV20120155240

E Deleersnijder and P Luyten. On the practical advantages of the quasi-equilibrium version of the Mellor and Yamada level 2.5 turbulence closure applied to marine modelling. *Applied Mathematical Modelling*, 18, 281-287, 1994. URL http://www.sciencedirect.com/science/article/pii/0307904X94903360

E Deleersnijder, H Burchard, and A Dijkstra. On the stability of turbulence closure schemes for stratified flows. *6th National Congress on Theoretical and Applied Mechanics*, Ghent, May 26-27, 2003. URL www.vliz.be/imisdocs/publications/114364.pdf

D P Dee, E Källén, A J Si Simmons, and L Haimberger. Comments on ‘Reanalyses suitable for characterizing long-term trends’. *Bulletin of the American Meteorological Society*, 92, 65-70, 2011. doi:10.1175/2010BAMS3070.1. URL http://journals.ametsoc.org/doi/abs/10.1175/2010BAMS3070.1

W J Emery and R E Thomson. Data Analysis Methods in Physical Oceanography. *Pergamon Press*, 1998.

M C Easton, D K Woolf, and P A Bowyer. The dynamics of an energetic tidal channel, the Pentland Firth, Scotland. *Continental Shelf Research*, 48, 50-60, 2012. doi: 10.1016/j.csr.2012.08.009. URL https://www.researchgate.net/profile/David_Woolf5/publication/257118863_The_dynamics_of_an_energetic_tidal_channel_the_Pentland_Firth_Scotland/links/56c491e608ae7fd4625a2c4e.pdf

B Galperin, L H Kantha, S Hassid, and A Rosati. A quasi-equilibrium turbulent energy model geophysical flows. *Journal of the Atmospheric Sciences*, 45, 55-62, 1988. URL http://journals.ametsoc.org/doi/abs/10.1175/1520-0469%281988%29045%3C0055%3AAQETEM%3E2.0.CO%3B2

C Garrett. Internal Tides and Ocean Mixing. *Science*, 301, 5641, 1858-1859, 2003. URL http://science.sciencemag.org/content/301/5641/1858

L Howard. Note on a paper of John W. Miles. *Journal of Fluid Mechanics*, 10, 509-512, 1961. doi:10.1017/S0022112061000317. URL https://www.cambridge.org/core/journals/journal-of-fluid-mechanics/article/note-on-a-paper-of-john-w-miles/D4BC22318F2F27EC642A65D1649F53F6

M J Howarth, J H Simpson, J Sündermann, and H van Haren. Processes of vertical exchange in shelf seas (PROVESS). *Journal of Sea Research*, 47, 199-208, 2002. doi:10.1016/S1385-1101(02)00125-9. URL http://www.sciencedirect.com/science/article/pii/S1385110102001259?via%3Dihub

H van Haren, L Maas, J T FZimmerman, H Ridderinkhof, H Malschaert. Strong inertial currents and marginal internal wave stability in the central North Sea. *Geophysical*

Research Letters, 26, 2993-2996, 1999.
URL http://onlinelibrary.wiley.com/doi/10.1029/1999GL002352/full

T Johnston and D Rudnick. Observations of the transition layer. *Journal of Physical Oceanography*, 39, 780-797, 2009.
URL http://journals.ametsoc.org/doi/abs/10.1175/2008JPO3824.1

W Krauss. Inertial waves in an infinite channel of rectangular cross section. *Deutsche Hydrografische Zeitschrift*, 32, 248-266, 1979.
URL https://link.springer.com/article/10.1007/BF02226052

P J Knight, M J Howarth, and T P Rippeth. Inertial currents in the northern North Sea. *Journal of Sea Research*, 47, 269-284, 2002.
URL http://www.sciencedirect.com/science/article/pii/S1385110102001223

Y D Lenn, T K Chereskin, J Sprintall, and J L McClean. Near-surface eddy heat and momentum fluxes in the Antarctic Circumpolar Current in Drake Passage. *Journal of Physical Oceanography*, 41, 1385-1407, 2011. doi: 10.1175/JPO-D-10-05017.1.
URL http://journals.ametsoc.org/doi/abs/10.1175/JPO-D-10-05017.1

B J Lincoln. Thermocline mixing in a seasonally stratified shelf sea. *Bangor Uniersity*, 2012.

B J Lincoln, T P Rippeth, and J H Simpson. Surface mixed layer deepening through wind shear alignment in a seasonally stratified shallow sea. *Journal of Geophysical Research: Oceans*, 121, 6021-6034, 2016. doi:10.1002/2015JC011382
URL http://onlinelibrary.wiley.com/doi/10.1002/2015JC011382/abstract

L R M *Maas* and J J M van *Haren.* Observations on the vertical structure of tidal and inertial currents in the central North Sea. *Journal of Marine Research*, 45, 293-318, *1987*.
URL http://www.ingentaconnect.com/content/jmr/jmr/1987/00000045/00000002/art00002

J MacKinnon and M C Gregg. Near-inertial waves on the New England shelf: The role of evolving stratification, turbulent dissipation, and bottom drag. *Journal of Physical Oceanography*, 35, 2408-2424, 2005.
URL http://journals.ametsoc.org/doi/abs/10.1175/JPO2822.1

Patrick McMurtry, Turbulence Mixing, 2017.
http://www.eng.utah.edu/~mcmurtry/Turbulence/turbmod.pdf

G L Mellor and T Yamada. A Hierarchy of turbulence closure models for planetary boundary layers. *Journal of the Atmospheric Sciences*, 31, 1791-1806, 1974. URL http://journals.ametsoc.org/doi/abs/10.1175/1520-0469%281974%29031%3C1791%3AAHOTCM%3E2.0.CO%3B2

G L Mellor and T Yamada. Development of a turbulence closure model for geophysical fluid problems. *Reviews of Geophysics and Space Physics*, 20, 851-875, 1982.
URL http://onlinelibrary.wiley.com/doi/10.1029/RG020i004p00851/abstract

J Miles. On the stability of heterogeneous shear flows. *Journal of Fluid Mechanics*, 10, 496-508, 1961. URL https://www.cambridge.org/core/journals/journal-of-fluid-mechanics/article/on-the-stability-of-heterogeneous-shear-flows/A9FC1F74697EB29B680F55D571E17218

C Millot and M Crépon. Inertial oscillations on the continental shelf of the Gulf of Lions-Observations and theory. *Journal of Physical Oceanography*, 11, 639-657, 1981. doi:10.1175/1520-0485(1981)011,0639:IOOTCS.2.0.CO;2. URL http://journals.ametsoc.org/doi/abs/10.1175/1520-0485%281981%29011%3C0639%3AIOOTCS%3E2.0.CO%3B2

Morgan. sw_dens0.m. 1992 . URL http://opg1.ucsd.edu/~sio221/SIO_221A_2009/SIO_221_Data/Matlab5/seawater/sw_dens0.m

Pawlowicz et al. t_tide.m. 2001. URL http://nccoos.org/projects/long-bay-wintertime-blooms/code/toolboxes/t_tide/t_tide.m/view

D Pugh. Tides, Surges and Mean Sea Level. *Wiley-Blackwell*, 1987.

T P Rippeth. The control of stratification in a fjordic system (the Clyde Sea). *Bangor University*, 1993.

T P Rippeth, J H Simpson, R J Player, and M Garcia. Current oscillations in the diurnal-inertial band on the Catalonian shelf in spring. *Continental Shelf Research*, 22, 247-265, 2002.
URL http://www.sciencedirect.com/science/article/pii/S0278434301000565

T P Rippeth. Mixing in seasonally stratified shelf seas: a shifting paradigm. *Philosophical transactions: Mathematical, physical, and engineering sciences*, 363, 2837-2854, 2005. URL http://www.jstor.org/stable/pdf/30039767.pdf?refreqid=excelsior%3A4734876ec43384d30bc7f637bde2c068

T P Rippeth, M R Palmer, J H Simpson, N R Fisher, and J Sharples. Thermocline mixing in summer stratified continental shelf seas. *Geophysical Research Letters*, 32, 10-13, 2005. URL http://onlinelibrary.wiley.com/doi/10.1029/2004GL022104/full

T P Rippeth, P Wiles, M R Palmer, J Sharples, and J Tweddle. The diapcynal nutrient flux and shear-induced diapcynal mixing in the seasonally stratified western Irish Sea. *Continental Shelf Research*, 29, 1580-1587, 2009.
URL http://www.sciencedirect.com/science/article/pii/S0278434309001605

T P Rippeth, B J Lincoln, H A Kennedy, M R Palmer, J Sharples, *and* C A J Williams. Impact of vertical mixing on sea surface $p\mathrm{CO}_2$ in temperate seasonally stratified shelf seas. *Journal of Geophysical Research: Oceans*, 119, 3868-3882, 2014. *doi:*10.1002/2014JC010089. URL http://onlinelibrary.wiley.com/doi/10.1002/2014JC010089/full

J H Simpson. Density Stratification and microstructure in the western Irish Sea. *Deep-sea research*, 18, 309-319, 1971.
URL http://www.sciencedirect.com/science/article/pii/0011747171900362

J H Simpson and J Hunter. Fronts in the Irish sea. *Nature*, 250, 404-406, 1974.
URL https://www.nature.com/nature/journal/v250/n5465/abs/250404a0.html

J H Simpson, D Bowers. The role of tidal stirring in controlling the seasonal heat cycle in shelf seas. *Annales geophysicae*, 2, 411-416, 1984. URL http://cat.inist.fr/?aModele=afficheN&cpsidt=8891016

J H Simpson and W Crawford, T P Rippeth, A R Campbell, and J V S Cheok. The vertical structure of turbulent dissipation in shelf seas. *Journal of Physical Oceanography*, 26, 1579-1590, 1996. URL http://journals.ametsoc.org/doi/abs/10.1175/1520-0485%281996%29026%3C1579%3ATVSOTD%3E2.0.CO%3B2

J H Simpson, P Hyder, T P Rippeth, and I M Lucas. Forced oscillations near the critical latitude for diurnal-inertial resonance. *Journal of Physical Oceanography*, 32, 177-187, 2002. URL http://journals.ametsoc.org/doi/abs/10.1175/1520-0485%282002%29032%3C0177%3AFONTCL%3E2.0.CO%3B2

J H Simpson and J Sharples. Introduction to the Physical and Biological Oceanography of Shelf Seas. *Cambridge University Press*, 2012.

R K Shearman. Observations of near-inertial current variability on the New England shelf. *Journal of Geophysical Research*, 110, C02012, 2005. doi:10.1029/2004JC002341.
URL http://onlinelibrary.wiley.com/doi/10.1029/2004JC002341/full

T Sherwin. Inertial oscillations in the Irish Sea. *Continental Shelf Research*, 7, 191-211, 1987. URL http://www.sciencedirect.com/science/article/pii/0278434387900793

M Sobarzo, L Bravo, D Donoso, J Garcés-Vargas, and W Schneider, Coastal upwelling and seasonal cycles that influence the water column over the continental shelf off central Chile. *Progress in Oceanography*, 75, 363-382, 2007. doi:10.1016/j.pocean.2007.08.022. URL http://www.sciencedirect.com/science/article/pii/S0079661107001577

IPCC. T F Stocker, D Qin, G K Plattner, M Tignor, S K Allen, J Boschung, A Nauels, Y Xia, V Bex and P M Midgley (eds.). Climate Change 2013: The Physical Science Basis. Contribution of Working Group I to the Fifth Assessment Report of the Intergovernmental Panel on Climate Change. *Cambridge University Press*, 2013. doi:10.1017/CBO9781107415324. URL http://www.ipcc.ch/report/ar5/wg1/

H Tennekes and J L Lumley. First Course in Turbulence. *MIT Press*, 1972.

S A Thorpe and Z Liu. Marginal instability? *Journal of Physical Oceanography*, 39, 2373-2381, 2009. URL http://journals.ametsoc.org/doi/full/10.1175/2009JPO4153.1

C C Tierney, M E Parke, *and* G H Born. An investigation of ocean tides derived from along-track altimetry, *Journal of Geophysical Research*, 103, 10273-10287, 1998. *doi:*10.1029/98JC00448.
URL http://onlinelibrary.wiley.com/doi/10.1029/98JC00448/full

K Toshinori. *Carbon Dioxide Problem*: *Integrated Energy* and Environmental Policies for the 21st Century. *CRC Press, 1998.*

L Umlauf and H Burchard. Second-order turbulence closure models for geophysical boundary layers. A review of recent work. *Continental Shelf Research*, 25, 795-827, **2005**. URL http://www.sciencedirect.com/science/article/pii/S0278434304003152

J J Walsh. Importance of continental margins in the marine biogeochemical cycling of carbon and nitrogen. *Nature*, 350, 53, 1991.
URL https://www.nature.com/nature/journal/v350/n6313/abs/350053a0.html

C Williams, J Sharples, C Mahaffey, *and* T Rippeth. Wind-driven nutrient pulses to the subsurface chlorophyll maximum in seasonally stratified shelf seas. *Geophysical Research Letters*, 40, 5467-5472, *2013. doi:*10.1002/2013GL058171.
URL http://onlinelibrary.wiley.com/doi/10.1002/2013GL058171/full

M Yelland and P K Taylor. Wind stress measurements from the open ocean. *Journal of Physical Oceanography*, 26, 541-558, 1996.
doi:10.1175/1520-0485(1996)026<0541:WSMFTO>2.0.CO;2.
URL http://journals.ametsoc.org/doi/abs/10.1175/1520-0485%281996%29026%3C0541%3AWSMFTO%3E2.0.CO%3B2